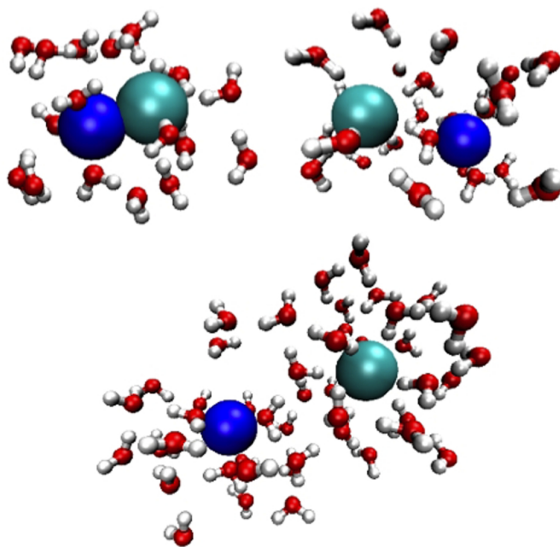Technische Universität München

Physik Department

Theoretische Physik T37
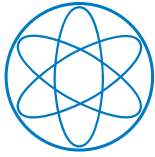
Aqueous Electrolytes:

Ion-Specific Structure and Thermodynamics

Immanuel Kalcher

Dissertation

Technische Universität München

Physik Department

Theoretische Physik T37

Aqueous Electrolytes:
Ion-Specific Structure and Thermodynamics

Dipl.-Ing.

Immanuel Kalcher

Contents

Abstract

Salt and ions are ubiquitous in every chemical and biological reaction in aqueous environment and therefore of fundamental interest. Intriguingly, different salt types affect the stability of colloidal and biological systems, as for example molecules in aqueous solution, very differently. These ion-specific effects can be attributed to salt properties in homogeneous solution (bulk) and to the interaction of ions with interfaces. In this thesis we will address both, but limit ourselves to simple model surfaces. Molecular dynamics (MD) simulations, in which water molecules and ions are simulated explicitly in atomistic detail, are used as an input to liquid state theory in order to study both bulk and interfacial properties of aqueous electrolyte solutions.

In the first part of this work we focus on bulk features and compute the ion-specific fluid structure of concentrated LiCl, NaCl, KCl, CsCl, KF, and NaI solutions. We then extrapolate short-ranged (nonelectrostatic) ion-ion potentials of mean force that enable us, on one hand, to calculate effective ion sizes and, on the other hand, to analyze structural consequences to the osmotic pressure. Since the latter is easily accessible experimentally, our presented methods permit to assess the viability of the MD setup for the ions up to high salt concentrations. In the second part we turn our attention to interfacial properties and show that structural inhomogeneities in the vicinity of a surface can be treated using classical density functional theory. Indeed, ion-specific excluded-volume correlations and electrostatic correlations can be included efficiently in a nonlocal Poisson-Boltzmann framework. The latter is simple-to-implement since the electrolyte is treated as an asymmetric nonadditive hard sphere system with previously calculated ion-specific ion sizes. In the final part we provide microscopic insights into crystallization. We focus on the NaCl salt and study fast crystallization in both bulk and confinement situations.

In summary, this thesis demonstrates how ion-specific *macroscopic* thermodynamic properties (pressure, solvation forces, etc.) can be interpreted and predicted by tracing them back to ion-specific *microscopic* structural properties. Presented methods are furthermore perfectly suited to be used in future investigations of more complicated, biologically relevant systems at high salt concentrations.

Zusammenfassung

Salz spielt eine fundamentale Rolle beim Ablauf biologischer und chemischer Reaktionen. Erstaunlicherweise beeinflussen verschiedene Salzarten die Stabilität kolloidaler und biologischer Systeme höchst unterschiedlich. Das Auftreten dieser sogenannten salzspezifischen Effekte muss Salzeigenschaften in homogener Lösung, sowie der Wechselwirkung von Ionen mit Oberflächen zugeschrieben werden. Wir behandeln in dieser Arbeit beide Fälle, wobei wir uns auf einfache Grenzflächen beschränken. Wir verwenden Ergebnisse aus Molekulardynamik (MD) Simulationen, in welchen Wasser und Ionen explizit mit atomarer Genauigkeit simuliert werden, um mit Hilfe der Flüssigkeitstheorie und statistischer Mechanik wichtige Salzeigenschaften in homogener Lösung und an Grenzflächen zu bestimmen.

Im ersten Teil dieser Arbeit konzentrieren wir uns auf Eigenschaften homogener Flüssigkeiten und berechnen die salzspezifische Struktur konzentrierter LiCl, NaCl, KCl, CsCl, KF, und NaI Lösungen. Uns gelingt es kurzreichweitige, nichtelektrostatische Ion-Ion Wechselwirkungspotentiale zu extrapolieren, aus welchen wir einerseits effektive Ionengrößen, und andererseits die Auswirkungen der Salzstruktur auf den osmotischen Druck berechnen. Da dieser eine experimentell einfach messbare Größe ist, können wir Rückschlüsse auf die Anwendbarkeit unseres MD Ansatzes zur Modellierung von Ionen bei hohen Salzkonzentrationen ziehen. Im zweiten Teil dieser Arbeit widmen wir uns Grenzflächeneigenschaften und analysieren die Salzstruktur zwischen zwei hydrophoben Platten mit Plattenabständen im Nanometerbereich. Wir zeigen, dass ionenspezifische Ion-Ion Korrelationen im Rahmen eines nichtlokalen Poisson-Boltzmann Ansatzes effektiv behandelt werden können. Wir betonen hierbei die Einfachheit dieser Methode, in welcher Ionen als asymmetrische und nichtadditive harte Kugeln betrachtet werden. Im dritten Teil dieser Arbeit gewinnen wir Einblick in die Kristallbildung auf mikroskopischen Skalen und analysieren mittels MD Simulationen die Kristallstruktur des NaCl Salzes zwischen zwei Platten und in homogener Lösung.

Zusammenfassend zeigen wir wie salzspezifische *makroskopische* thermodynamische Eigenschaften von Salzlösungen (Druck, Kräfte auf Oberflächen, etc.) auf *mikroskopische* strukturelle Eigenschaften zurückgeführt werden können. Wir betonen des Weiteren, dass unsere Methoden in zukünftige Untersuchungen komplizierter, biologisch relevanter Systeme bei hohen Salzkonzentrationen einbezogen werden sollten.

Chapter 1

Introduction

Aqueous electrolyte solutions are of fundamental importance to (physical) chemistry and biology, and form a basic matrix for technological fluids and the evolution and function of life. Especially the monovalent ions Na^+, K^+, and Cl^- are substantial ingredients in the specific or unspecific regulation of (bio)molecular processes, such as action potentials, osmotic flows, or the stabilization and function of proteins, lipids, or nucleic acids [1]. The simplest model for describing aqueous electrolytes is the so-called primitive model (PM), in which ions are modeled as charged hard spheres (HS) and water is treated as a continuum dielectric background. Even though the PM is still in use today, it is evident that such a non-specific model fails in predicting even the most basic thermodynamic properties of aqueous electrolytes. The osmotic coefficient, which is a measure for the deviation of the osmotic pressure compared to the ideal gas (non-interacting point-particles) pressure, varies widely for different monovalent salts [2] as can be seen in fig. 1.1; an observation that cannot be explained on the PM level. The specific action of individual ions (e.g., Na^+ vs. K^+) has received increased attention only recently and has triggered a revival in the investigation of ionic properties in bulk and at interfaces, as well as of ionic interactions with biomolecules and accompanying 'Hofmeister effects' [3–8]. The latter terminology, going back to Hofmeister's investigation of salt's specific action on the precipitation of egg white protein [9], is often used synonymously for salt-specific effects; typically those are found categorized in cation and anion 'Hofmeister series' but are not unique in general.

Even in homogeneous, aqueous bulk solutions, salt-specificity can occur already at an electrolyte concentration ρ larger than the Debye-Hückel limiting value of $\simeq 10$ mM [11] and affects macroscopic quantities, such as the solution activity, the electrolyte osmotic pressure Π, or the static dielectric constant $\epsilon(\rho)$. These experimentally accessible properties show a complex dependence on salt concentration and type. At a fixed ρ, for instance, the osmotic coefficient for a growing van der Waals radius of an alkali ion (e.g., $Na^+ \rightarrow K^+$) decreases in presence of the anion Cl^- but *increases* in the presence of F^- [2]
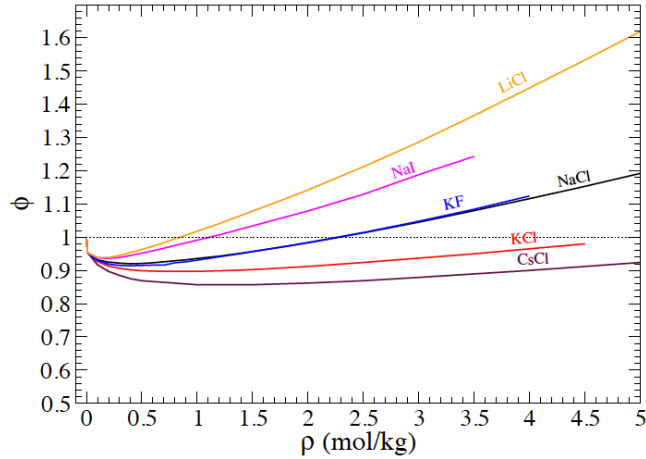
Figure 1.1.: *The experimental osmotic coefficient ϕ vs. salt concentration ρ, taken from ref. [10], for LiCl, NaCl, KCl, CsCl, NaI, and KF. The ideal gas osmotic coefficient $\phi = 1$ is depicted as the horizontal black line.*

(cf. fig. 1.1). Similarly, simple salts at a moderate concentration can considerably alter the value of the dielectric constant at infinite dilution $\epsilon(0)$ involving nontrivial trends: the relative decrease of $\epsilon(\rho)$ at a fixed ρ, for instance, increases for a growing radius of halide ions (e.g., KF $\rightarrow$ KCl) but *decreases* for a growing radius of an alkali ion (e.g., NaCl $\rightarrow$ KCl) [12].

The microscopic reason for these context-dependent trends above lies apparently in the water structure around individual or interacting ions in aqueous environment [12–15]. The highly complex hydration patterns must be traced back to the multipolar and anisotropic nature of the water molecule. In fact, it has been argued that these individual solvation properties govern the affinity of ionic groups in bulk and at (biomolecular) interfaces to associate and form direct salt pairs [16, 17]. In this view, referred to as the 'law of matching water affinities', only oppositely charged ions with matching free energies of hydration form *contact* ion pairs (sometimes called 'inner sphere' pairs, where the ions 'touch' and loose part of their first hydration shell). This proposal has been supported by recent experimental and theoretical studies on dilute systems [18–21]. Whether this view holds for concentrated solutions and how it affects macroscopic bulk or interfacial properties, is, however, not well understood.

In principle, a means to access the detailed solution structure is provided by explicit-water molecular dynamics (MD) computer simulations [22–30], in which water atoms and ions are explicitly resolved on an atomic scale by assigning (partial) Coulombic point charges q_i, excluded-volume sizes, and dispersion attractions. Typically, the non-electrostatic atom-atom interaction between two atoms at a distance r is modeled by a radially symmetric Lennard-Jones (LJ) potential that depends on the atom-atom inter-action length σ and the energy scale ϵ. The whole set $\{\sigma, \epsilon, q\}$, accompanied by adequate mixing rules, typically defines the total *force field*. It has to be emphasized that in this picture quantum effects and ion polarizabilities are not included and that therefore the

viability of the LJ approach depends on whether the latter can be neglected. Furthermore, the LJ potential is empirical and the $\{\sigma, \epsilon\}$ set is typically fitted to reproduce experimentally accessible characteristics. The empirical force fields for the ions used are typically benchmarked to single ion properties (such as the solvation free energy), and often fail to reproduce realistic electrolyte structure or thermodynamics at non-vanishing concentrations. As has been recognized early in literature, one reason is the strong sensitivity of thermodynamics to small changes in the potential of mean force (pmf) between two ions in solution [31–33]. Ion force field development thus remains an active field of research [34–36]. A link between the microscopic structure and electrolyte thermodynamic properties is given by liquid state theory [37–41]. The electrolyte thermal compressibility χ_T and the electrolyte osmotic pressure Π, for instance, can in principle be calculated exactly via a superposition of integrated ionic pair structures [39, 40]. This exact procedure, called the *compressibility route*, allows for a direct test of the empirical MD force fields and is presented in detail in this work.

A second, more popular way to obtain the electrolyte osmotic pressure is to calculate effective (solvent-averaged) ion-ion potentials as supplied by McMillan-Mayer theory [37, 38], and use them as input in implicit methods, such as Hypernetted-Chain (HNC) integral equations or Monte-Carlo (MC) simulations [24, 25, 27–32, 42–46]. Here, the electrolyte osmotic pressure Π can directly be calculated from the virial equation [39–41]. While the McMillan-Mayer theory is in principle exact, a major problem of the HNC and MC approach is that they require effective *pair* (two-body) potentials. Effective ion-ion potentials are, however, not pairwise additive due to solvent-mediated many-body contributions. This has been systematically demonstrated by Lyubartsev and Laaksonen using involved inverse MC methods [24, 25]. As a possible simplification, it has been suggested that many-body effects in electrolytes could be effectively modeled by a concentration-dependent dielectric constant $\epsilon(\rho)$ [47–49]. In fact, Hess and coworkers have recently applied this correction to MD-derived infinite-dilution pair potentials in implicit stochastic computer simulations and could accurately reproduce experimental osmotic coefficients for NaCl [27, 28]. The osmotic coefficient is a quantity highly sensitive to the particular force field or pmf [25, 27, 28, 31, 32], but good agreement could be achieved by using a NaCl force field benchmarked to solution activity derivatives [50]. This method, however, does not offer a direct way to the electrolyte osmotic pressure. We will present in this thesis an efficient way, via the so-called *virial route*, to benchmark MD force fields to this sensitive quantity of high physiological relevance [1]; a highly relevant topic of current investigations [51–53].

Considering interfacial properties of dense electrolytes, the study of ion-specific solvation forces and ionic structure between two adjacent surfaces is highly relevant for biological and colloidal systems [8, 54]. Detailed knowledge of the ion-surface interaction is therefore required [55]. The potentials describing these interactions are known to be not only ion-specific but also highly dependent on the surface chemistry [56, 57]. Indeed, force measurements show that solvation forces between mica- [54, 58] and silica- [59, 60] surfaces are non-monotonic, ion-specific, and cannot be described with the clas-

sical Derjaguin-Landau-Verwey-Overbeek (DLVO) theory (described in more detail in the next paragraph). In this realm, the ion-specific restabilization of dispersions of colloids [61, 62] and clays [63, 64] in dense electrolytes or the origin of charge reversal and attraction between like-charged surfaces [65, 66] is not entirely understood and still a matter of ongoing research [67].

The ion-specific restabilization of protein coated cationic (IgG-)latex particles at high salt concentrations shown in fig. 1.2 cannot be explained with the DLVO theory. The DLVO theory treats the colloidal system as polyions (dispersed phase), in this specific case the cationic latex particles, and microions (continuous phase). The electrolyte (microions) degrees of freedom are integrated out on a mean-field level. The resulting electrostatical part of the DLVO interaction between two polyions is strictly repulsive [40] and compensates the attractive van der Waals force. At low salt concentrations (<0.5 M) the colloidal suspension will therefore be stabilized due to the repulsive DLVO interaction. For increasing salt concentration, the surface charge of the (cationic) particles will gradually be compensated by surface-adhering (anionic) counterions and the colloidal suspension will aggregate (flocculate) due to the attractive van der Waals forces. The restabilization of the IgG-latex particles at high salt concentrations above 1 M, observed in fig. 1.2, cannot be explained within the DLVO theory, and is attributed to the so-called, non-DLVO, hydration or solvation forces [68]. The origin and the ion-specificity of the latter are not understood.

Protein-protein interactions between hydrophobic, nonpolar, groups are also highly affected by the salt type in solution [69, 70]. These findings are highly relevant at moderate to high salt concentrations for protein crystallization studies, which are of considerable interest, since they provide a link to protein structure by means of X-ray crystallography [71].

The study of ion-specific properties of electrolyte solutions in confinement situations is therefore highly relevant. The mean-field Poisson-Boltzmann (PB) theory is a useful starting point for the examination of electrolytes in confinement because of its simplicity and predictive power, particularly in systems with weak surface charges and low ion valencies [40, 72, 73]. In PB theory, ions are treated as point-charges interacting only electrostatically on a mean-field level. On such a premise, universal electrostatic ion-ion correlations that are important for systems with strong electrostatic coupling are not accounted for [74]. Methods on how to venture beyond this limitation have been discussed in literature [75–77]. For dense and very inhomogeneous electrolytes in confinement, however, one can suspect the system to be dominated by nonelectrostatic excluded-volume interactions and thus electrostatic correlations to be of minor importance.

The inclusion of those nonelectrostatic (partially solvent-mediated) ion-ion and ion-surface pair potentials is a subtle matter since PB treats the solvent as a homogeneous background continuum with a uniform dielectric constant. In order to account for these potentials we employ explicit-water molecular dynamics (MD) simulations to compute effective ion-ion and ion-wall potentials of mean force at *infinite dilution*. In this picture, the water degrees of freedom are integrated out and dispersion, hydration, and image
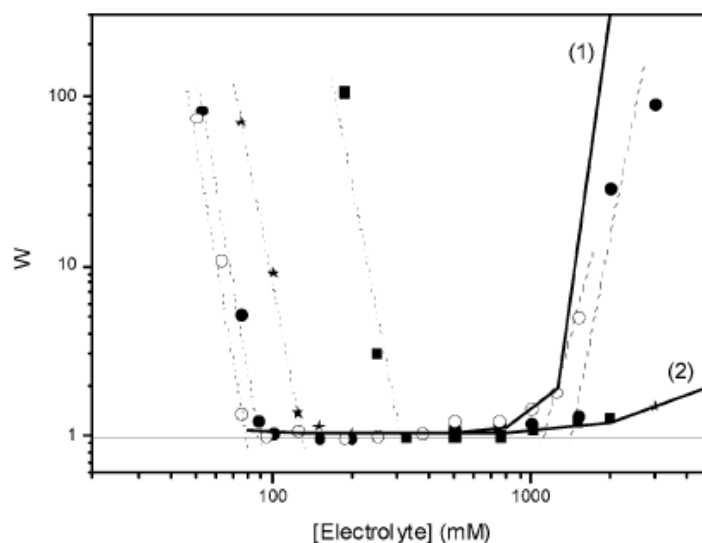
Figure 1.2.: *Stability ratio W plotted versus electrolyte concentration for protein coated IgG-latex particles at pH 4. At high salt concentrations (>1 M) the colloidal system exhibits a restabilization pattern that cannot be explained by the classical DLVO theory. The effect is shown for different electrolytes: NaSCN (⋆), NaNO$_3$ (∘), NaCl (•), and Ca(NO$_3$)$_2$ (□). Figure taken from ref. [61].*

charge effects are included on a two-body level. An ion-surface pmf can easily be included in the Boltzmann exponent as an external potential, whereas the nonelectrostatic ion-ion interactions are often treated using *local* or *nonlocal* extensions to PB theory [40]. How to design these extensions to PB efficiently in order to study for instance aforementioned solvation forces, is an integral part of this work.

For a certain threshold salt concentration, which depends on the salt type and on environmental conditions, a liquid-crystal phase change occurs in the slab-water-salt system. Indeed, crystallization of salts inside porous materials such as concrete, mortar or stone degrades buildings and our cultural heritage. Salt weathering has therefore been studied for decades experimentally and theoretically [78–81]. Nonetheless, the mechanism of crystallization pressure in confinement, that is believed to be the main reason for salt damage, is still not understood on a molecular level [82–93]. The amount of damage, for example, depends on multiple factors such as the salt type, interfacial properties or the preference of salt to crystallize inside pores (subfluorescence) or outside pores (efflorescence), the latter being far less harmful [80].

Classical MD simulations provide a direct means to investigate salt crystallization in confinement at molecular detail. However, while one-component systems under confinement conditions have been studied in detail [94–104], results remain patchy for more realistic slab-water-salt systems at saturated salt concentrations. The molecular modeling of the latter is indeed complex and poses many problems. Most notably, realistic confining surfaces have to be modeled phenomenologically and, furthermore, the time scale on which salt crystallization takes place is prohibitively long for standard MD simulation

setups. Thus, more sophisticated methods might be required [105, 106]. Nonetheless, it is in principle possible to follow a more direct and simplified approach: one can induce sufficiently large supersaturations in order to cause crystallization within a few nanoseconds, a time range accessible with MD simulations [107, 108]. In this work we suggest to study a simplified setup for a sufficiently long, but accessible time range. We use simple model surfaces and the NaCl salt as a first step, since little is known so far concerning the crystal structure and the molecular origin for crystallization stresses.

This thesis is structured as follows:

Outline

In chapter 2, we describe all computational techniques involved.

In chapter 3, we explain the theoretical methods that we use in this work. We focus on how electrolyte structure and thermodynamics are linked by liquid state theory and how density functional theory (DFT) can be used to modify the mean-field PB theory in order to account for electrostatic and excluded-volume correlations.

In chapter 4, we first calculate the electrolyte structure and effective ion-ion diameters for a range of monovalent salts by means of all-atom MD simulations in bulk. We then compute the osmotic pressure via the compressibility and the virial routes and demonstrate that they yield equivalent results up to moderate salt concentrations. Additionally, we compare the calculated osmotic coefficients to experimental values and find good agreement for most salts. The dielectric constant $\epsilon(\rho)$ is shown to decrease with increasing salt concentration ρ for all salts and good qualitative agreement with experimental data is observed.

In chapter 5, we use effective short-ranged ion-ion as well as short-ranged ion-surface potentials of mean force, both MD-derived at infinite dilution, and include them in modified PB theories. The simplest-to-implement nonlocal DFT-PB approximation (NPB-HS)—which treats the electrolyte as an asymmetric and nonadditive hard sphere (HS) system—is shown to reproduce the ionic structure in a slab geometry very well compared to results of MD and MC simulations. All local approaches fail. We then use NPB-HS in order to inspect the impact of ion-specific excluded-volume correlations on solvation forces, salt expulsion between two like-charged plates (Donnan effect), and overcharging.

In chapter 6, we single out the NaCl salt and analyze crystallization patterns in both bulk and a slab geometry. For slab geometries and surface-to-surface distances of roughly 1.5 nm, we observe a desalting effect in a pseudo grand canonical ensemble, where the salt is entirely expelled from the still hydrated slab.

In chapter 7, we present a summary and an outlook.

Chapter 2

Computational Methods

In this chapter we will describe all computational methods used in this work. First, we will provide computational details on the molecular dynamics (MD) simulation setup for simulations of bulk electrolytes. Then, configurations derived from both MD and Monte-Carlo (MC) simulations for an electrolyte in a one-dimensional nanoconfinement will be described. As to the MD simulations, setups in both the canonical and a pseudo grand canonical ensemble will be presented. We will finally sketch shortly the algorithm we use for solving modified Poisson-Boltzmann (PB) equations.

2.1. MD simulations in bulk

We simulate aqueous electrolytes by means of all-atom classical molecular dynamics (MD) simulations, a standard computational method in which Newton's equation of motion is integrated for every atom [109, 110]. We use the MD simulation package GROMACS [111, 112] and simulate at constant particle number N, pressure $P = 1$ bar, and temperature $T = 300$ K using a Berendsen barostat and thermostat [113] (NPT ensemble), respectively. The periodically repeated cubic simulation box has an edge length $L \simeq 4$ nm and includes explicit ions and SPC/E water [114] yielding a total number of $N_w \simeq 2000$ simulated water molecules. A few simulations are conducted at box lengths of 3 and 6 nm to assess finite-size effects. We use the three dimensional particle-mesh Ewald (PME) summation method for electrostatics [115]. The PME routine employs a grid-spacing in Fourier space of 0.12 nm in all three directions, an interpolation order 4, a distance cut-off of 0.9 nm for the real-space interactions, and a relative strength of the electrostatic interaction at the cutoff of 10^{-5}. Typical runs for gathering statistics are 150-200 ns in time after a $\simeq 5$ ns period of equilibration. We focus on bulk structure and thermodynamics of the six simple salts LiCl, NaCl, KCl, CsCl, NaI, and KF for a wide range of electrolyte densities from high dilution $\rho = N_s/L^3 \simeq 0.025$ M (mol/l) up to 5 M, provided by $N_s = 1$ up to ~ 200 salt pairs in solution, respectively. Note that

the total number of ions in our symmetric and monovalent system is $2N_s$ that leads to a factor of 2 in some of the thermodynamic definitions in chapters 3 and 4. The ions are modeled as charged and nonpolarizable Lennard-Jones (LJ) spheres. Two charged LJ spheres i, j, separated by a distance r, interact with the radially symmetric potential

$$V_{ij}(r) = V_{ij}^{\mathrm{LJ}}(r) + V_{ij}^c(r), \tag{2.1}$$

consisting of the LJ potential V_{ij}^{LJ} and the Coulombic potential V_{ij}^c, viz.

$$V_{ij}^{\mathrm{LJ}}(r) = 4\epsilon_{ij} \left[\left(\frac{\sigma_{ij}}{r} \right)^{12} - \left(\frac{\sigma_{ij}}{r} \right)^6 \right] \tag{2.2}$$

$$V_{ij}^c(r) = \frac{q_i q_j}{4\pi\epsilon_0 \epsilon r}, \tag{2.3}$$

where q_i is the charge of sphere i, ϵ_0 is the vacuum permittivity, and ϵ is the dielectric constant.

The LJ parameters, the energy ϵ and size σ of Li$^+$, Na$^+$, K$^+$, Cs$^+$, F$^-$, and Cl$^-$ are taken from Dang [116–119]. For KCl we investigate an additional force field from Joung and Cheatham [35] for comparison. The cross interactions are calculated by the Lorentz-Berthelot mixing rules. The resulting ion-water LJ parameters and the SPC/E parameters are summarized in tab. 2.1 on the facing page. Hydration structure and the mobility of single ions within the above MD force field have been studied in literature before [14, 120, 121]. We note that we attempted our analysis also for NaCl and KCl from the Amber force fields, which employs cations from Åqvist [122] and chloride from Dang. No reasonable analysis was possible, however, because of unphysical clustering at concentrations $\rho \gtrsim 0.2$ M as has been reported previously [28, 35, 50, 123].

2.2. MD simulations in confinement

2.2.1. Canonical ensemble

Our MD simulations in confinement situations are very similar to the simulations in bulk described previously and the same MD package is used. Nonetheless, due to the different geometry, we want to point out a few differences. We simulate at constant particle number N, constant pressure $P \simeq 1$ bar using an anisotropic Parrinello-Rahman barostat [124] in x- and y-direction—contrary to the bulk case no pressure coupling in the z-direction is used—and a temperature $T = 300$ K using a Nosé-Hoover thermostat [125]. The rectangular simulation box has periodically repeated edges of size $L_x \simeq L_y \simeq 4.15$ nm and is delimited in vertical z-direction by two walls specified in the following with a surface-to-surface distance d, which is defined as the distance on the z-axis between the centers of the respective surface C-atoms (cf. fig. 2.1(a)). We simulate a number of $N_w = 700 - 900$ SPC/E [114] water molecules and $N_i = 1 - 90$ explicit ion pairs in this one-dimensional confinement. The ions are nonpolarizable and interact with the

Table 2.1.: *Ion-water oxygen (iO) and wall-water oxygen (CO) Lennard-Jones (LJ) parameters and charges used in this work. The LJ potential is given by $V_{ij}^{LJ}(r) = 4\epsilon_{ij}\left[\left(\frac{\sigma_{ij}}{r}\right)^{12} - \left(\frac{\sigma_{ij}}{r}\right)^6\right]$. Lorentz Berthelot mixing rules are given by $\sigma_{ij} = \frac{(\sigma_{ii}+\sigma_{jj})}{2}$ and $\epsilon_{ij} = \sqrt{\epsilon_{ii}\epsilon_{jj}}$.*

Ion	σ_{iO}(nm)	ϵ_{iO}(kJ/mol)	charge q/e
Li$^+$	0.2337	0.6700	+1
Na$^+$	0.2876	0.5216	+1
K$^+$	0.3250	0.5216	+1
K$^+$(II)	0.3004	1.0816	+1
Cs$^+$	0.3526	0.5216	+1
Cl$^-$	0.3785	0.5216	-1
Cl$^-$(II)	0.4000	0.1866	-1
F$^-$	0.3143	0.6999	-1
I$^-$	0.4168	0.5216	-1
SPC/E			
O	0.3169	0.6500	-0.8476
H	–	–	+0.4238
Wall			
C	0.3537	1.2861	0

Coulomb and LJ interaction described previously. Electrostatics are treated with the two-dimensional particle-mesh Ewald (PME) summation method [115].

The surface is modeled by a solid-like assembly of atomistic LJ spheres in a close-packed, harmonically restrained, hexagonal lattice arrangement. The LJ diameter is chosen so that the atoms have the size of a methyl group $\sigma_{ii} = 0.3905$ nm [126], and the energy $\epsilon_{ii} = 1.024\ k_{\mathrm{B}}T$ is chosen in order to reproduce the contact angle of a simple, nonpolar organic material such as paraffin of $\simeq 110°$. This angle is calculated by a simple mean-field integration over the interactions between the solid and the liquid [127]. Typically $n = 480$ wall atoms are involved of which $n_s = 120$ are situated on the surface; the wall width is $l_z \simeq 1$ nm which, given L_x and L_y, corresponds to a volume number density of $\rho_{wall} \simeq 28$ nm^{-3}. The positions of the wall atoms are harmonically restrained in 3 dimensions with a force constant $k = 5000$ kJ mol^{-1} nm^{-2}, which relates the force to a one-dimensional displacement by $F_i = -k\Delta x_i$. The lattice constants are $a \simeq 0.39$ nm for the basal and $b \simeq 0.64$ nm for the height parameter. A typical simulation snapshot of the molecular slab-water-salt system is shown in fig. 2.1(a).

In order to obtain effective infinite-dilution ion-wall pmfs $V_i^{ext}(z)$ we use umbrella sampling. A cation or anion is placed in the water phase near one wall and the ion-wall pmf is obtained by the weighted histogram analysis method (WHAM) [129, 130], see fig. 2.1(c) for an illustrative MD snapshot. Runs for gathering statistics of 1.5 ns in time each after an equilibration period of 500 ps are carried out in 80 distinct windows. We use a spring constant of 500 kJ mol^{-1} nm^{-2}.

(a) Setup in the canonical ensemble.

(b) Setup in a pseudo grand canonical ensemble. Both the electrolyte inside the slab and in the reservoir are simulated explicitly.

(c) Setup for umbrella sampling. One cation is positioned in front of the surface. Views in the x-y plane (a) and slightly tilted x-z plane (b) are presented. Only water molecules in the first two hydration shells of the ion are displayed.

Figure 2.1.: *Snapshots of typical MD simulations at molar salt concentration in (a) and (b). Cations (blue spheres) and anions (yellow spheres) in a one-dimensional nanoconfinement of width d immersed in water depicted as one oxygen (red sphere) and two hydrogen (white spheres) atoms. d is the surface-to-surface distance between the centers of adjacent surface C-atoms (turquoise spheres). The pictures are made using the VMD software [128].*

2.2.2. Pseudo grand canonical ensemble

MD simulations of confined electrolytes in the grand canonical ensemble are hard to simulate due to the per definitionem infinite salt reservoir. We therefore simulate a finite, sufficiently large, electrolyte reservoir in atomistic detail that mimics a grand canonical ensemble, which is clearly a compromise between accuracy and feasibility. We simulate an in all three directions periodically repeated rectangular box of edge sizes $L_x \simeq 4$ nm, $L_y \simeq 8.5$ nm and $L_z = 3 - 5$ nm, the latter depending on the size of the confinement. The ratio of simulated water molecules in confinement to water molecules in the reservoir depends on the size of the confinement but is on the order of $1/9$. A snapshot of a typical simulation for a surface-to-surface distance of $d = 2.5$ nm is shown in fig. 2.1(b). Note that for practical reasons we use a wall that is slightly smaller in y-direction than the one described before, i.e., $l_y = 3$ nm, but otherwise similar. The number of water molecules in the reservoir is $N_w \simeq 2600$ and the number of ion-pairs is $N_i = 0 - 200$ depending on the studied salt concentration. Typical simulation times are $t = 100 - 200$ ns.

2.3. Implicit-water MC simulations

We compare our results to standard MC simulations in the canonical ensemble [110, 131]. All MC simulations were performed by Julius Schulz within the framework of his diploma thesis [132]. Ion-ion and ion-wall interactions are modeled with radially symmetric short-range ion-ion pair potentials $V_{ij}^{\mathrm{sr}}(r)$ and effective ion-surface potentials $V_i^{ext}(z)$, that depend on the lateral distance z to the wall only, respectively. Both $V_{ij}^{\mathrm{sr}}(r)$ and $V_i^{ext}(z)$ are MD-derived potentials that will be described in detail in chapter 4. The effective potentials are linearly interpolated, continued to infinity on the lower bound and set to zero on the upper bound for cut-off distances of $z = 0.95 - 1$ nm and $r = 1$ nm. Up to $N = 308$ salt pairs are simulated in charged and uncharged slabs with width $d = 2$ nm and periodic boundary conditions in lateral xy-directions with box-lengths $L_x = L_y = 4.2$ nm. A typical simulation runtime is 10^6 MC steps with 10^4 equilibration steps. To accurately account for the long-ranged electrostatics, the two-dimensional Lekner-Sperb summation is used [133, 134]. The Lekner-Sperb potential is tabulated using a grid-size of 128 in each direction, where the points are quadratically distributed and linearly interpolated. For small separations $\left(r < 1.7\ 10^{-4}\ \mathrm{nm}\right)$ the potential is calculated explicitly.

2.4. Poisson-Boltzmann solver: numerical details

The equations of our modifications to PB theory presented in chapter 3 are solved by means of a general relaxation method. The domain of interest, the z-axis in the case of a one-dimensional confinement, is approximated by a mesh of up to 2100 grid points. Each mesh point corresponds to a finite difference equation that relates two neighboring points. Starting from an initial guess, the results relax to the actual solution. The convolutions in the NPB equations are treated with standard one-dimensional Fast Fourier Transform (FFT) techniques. We use a binning of $N = 8192$ points and a Nyquist

frequency of $f_c = 1/(2\,\Delta x) = 250$ nm^{-1}. Further technical details as to the methods involved are described in great detail elsewhere [135].

Chapter 3

Liquid State Theory of Electrolytes

In this chapter we will introduce the theoretical methods used in this work. First, we will detail how the electrolyte structure in form of the radial distribution function (rdf) can be linked to bulk thermodynamic properties like the osmotic pressure. Additionally, fluctuation formulas provide insight into the dielectric constant and the shear viscosity of electrolyte solutions. Secondly, we will show how to map an electrolyte and its intricate, water-mediated interactions onto an asymmetric and nonadditive hard-sphere (HS) system. The latter can easily be incorporated into various modified Poisson-Boltzmann (PB) descriptions by density functional theory (DFT) taking into account ion-specific excluded-volume correlations. Further on, we will introduce a method that enables us to include electrostatic correlations, that are important for low salt concentrations and high ion valencies, in a similar fashion. Thirdly, and as a means to investigate the influence of excluded-volume correlations in chapter 5, we will describe among others the origin of the double-layer pressure between two plates and salt expulsion between two like-charged plates (Donnan effect). In the last part of the chapter we will analyse the so-called Grahame equation—that links the surface charge to the salt concentration in the reservoir and the electrostatic potential at the interface—by means of NPB-el, a modified PB equation that accounts for electrostatic correlations.

3.1. Electrolyte structure

3.1.1. Radial distribution functions

Let us consider, as a starting point, an isotropic system of N indistinguishable particles. The n-particle density $\rho_N^{(n)}(\vec{r}^n)$ is then defined such that $\rho_N^{(n)}(\vec{r}^n)\mathrm{d}\vec{r}^n$ represents the probability to find n particles with coordinates $\vec{r}^n$ in the volume element $\mathrm{d}\vec{r}^n$. We are particularly interested in the one- and two-particle densities $\rho_N^{(1)}$ and $\rho_N^{(2)}$, since they will prove to be easy to compute and adequate in order to calculate thermodynamic prop-
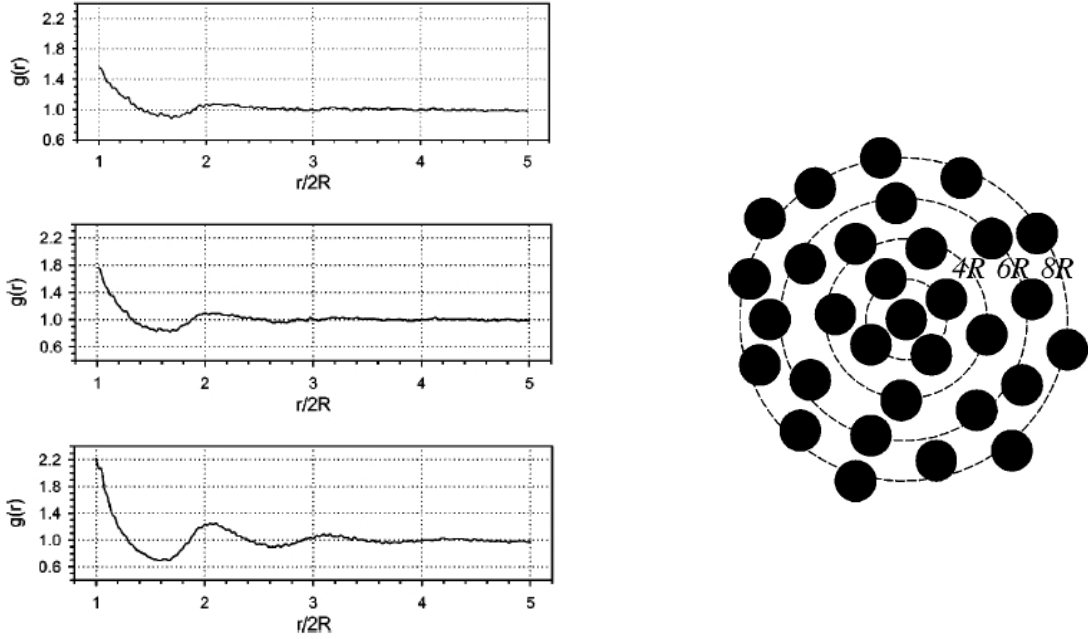
(a) Rdfs for different particle area fractions of 30%, 40% and 50% top to bottom figure, in order.

(b) Schematic picture showing the preferred positions of hard-spheres in terms of distance to one central sphere.

Figure 3.1.: *Radial distribution functions of identical small metallic spheres of diameter 2R experimentally obtained by means of video analysis. Figures taken from ref. [136].*

erties with sufficient accuracy. For the two-particle density, it is useful to introduce a two-particle distribution function $g_N^{(2)}$ that is defined as [40, 137, 138]

$$g_N^{(2)}(\vec{r}_1, \vec{r}_2) = \frac{\rho_N^{(2)}(\vec{r}_1, \vec{r}_2)}{\rho_N^{(1)}(\vec{r}_1) \times \rho_N^{(1)}(\vec{r}_2)} \tag{3.1}$$

and is a measure of the randomness in the system. In an isotropic system, $g_N^{(2)}$ depends only on the distance between the two particles $r = |\vec{r}_2 - \vec{r}_1|$ and is therefore simply written as $g(r)$. $g(r)$ is called the *radial distribution function* (rdf). $\rho g(r)$ is the average particle density at distance r from the origin, given that one particle is located at the origin in an electrolyte of average concentration ρ. Similarly, one may define the coordination number

$$n_{\text{coord}} = 4\pi\rho \int_0^{r_0} g(r)\, r^2 \mathrm{d}r, \tag{3.2}$$

that defines the number of neighboring particles closer than r_0 to the particle at the origin.

The one- and two-particle densities, and thus also $g(r)$, can conveniently be expressed by delta functions [40]:

$$\rho_N^{(1)}(\vec{r}) = \left\langle \sum_{i=1}^{N} \delta(\vec{r} - \vec{r}_i) \right\rangle \tag{3.3}$$

$$\rho_N^{(2)}(\vec{r}, \vec{r}^{\,\prime}) = \left\langle \sum_{i=1}^{N} \sum_{j=1}^{N} \delta(\vec{r} - \vec{r}_i)\delta(\vec{r}^{\,\prime} - \vec{r}_j) \right\rangle \tag{3.4}$$

$$\rho g(r) = \left\langle \frac{1}{N} \sum_{i=1}^{N} \sum_{j=1}^{N} \delta(\vec{r} - \vec{r}_j + \vec{r}_i) \right\rangle, \tag{3.5}$$

where the double sum does not include $i = j$ terms and the $< \cdots >$ are ensemble averages. In the canonical ensemble—with fixed N, V and T—the two-particle density for example reads

$$\rho_N^{(2)}(\vec{r}_1, \vec{r}_2) = \frac{N(N-1)}{Z_N} \int \exp(-\beta V_N)\mathrm{d}\vec{r}_1 \mathrm{d}\vec{r}_2, \tag{3.6}$$

where V_N is the interatomic potential energy and $Z_N = \int \exp(\beta V_N)\mathrm{d}\vec{r}^N$ is the configurational integral. Note that in (3.6) the integrals over momenta cancel. The $N(N-1)$ term in (3.6) stems from the fact that there are as much possibilities to choose two particles from a total of N particles.

Let us now consider the easy example of an ideal gas. Hence, our N particles being point particles, one- and two-particle densities as well as $g(r)$ are easy to compute and yield

$$\rho_N^{(1)} = \frac{N}{V} = \rho \tag{3.7}$$

$$\rho_N^{(2)} = \frac{N}{V} \times \frac{(N-1)}{V} = \frac{N^2}{V^2}\left(1 - \frac{1}{N}\right) = \rho^2\left(1 - \frac{1}{N}\right) \tag{3.8}$$

$$g(r) = \frac{\rho_N^{(2)}}{\rho^2} = \left(1 - \frac{1}{N}\right), \tag{3.9}$$

where V is the total volume of the system. The $\frac{1}{N}$ term on the rhs of the equations for $\rho_N^{(2)}$ and $g(r)$ is a finite size correction. In the thermodynamic limit $N \to \infty$, the two-particle density reduces to $\rho_N^{(2)} = \rho^2$ and the radial distribution function is $g(r) = 1$.

In a nonideal liquid, $g(r)$ typically deviates from 1, most notably for small separations because two particles cannot come indefinitely close due to their finite size, and converges to the ideal gas limit for $r \to \infty$. The $g(r)$ is a local measure of the deviation of the system from an uniform ideal gas like distribution and is in general accessible through radiation-scattering experiments [40, 137]. For descriptive reasons, we show rdfs of a model system of identical small metallic hard spheres in fig. 3.1.

When treating electrolytes, we will calculate rdfs $g_{ij}(r; \rho)$ between a pair of ions i and j at a salt concentration ρ, where the indices $i, j = +-$ can represent cations or anions, i.e., the particles are distinguished as cations or anions. For monovalent ions, the bulk salt concentration equals the cation and anion concentrations $\rho_+ = \rho_- = \rho$ and the rdf can be written as

$$g_{ij}(r; \rho) = \frac{\rho_{ij}^{(2)}(r)}{\rho^2}. \tag{3.10}$$

Analogously to the case of indistinguishable particles, $\rho g_{ij}(r; \rho)$ is—at a salt concentration ρ—the average density of ions of type i at a distance r from the origin, given that an ion of type j is placed at the origin. The $g_{ij}(r; \rho)$ is therefore a direct measure of the electrolyte structure.

3.1.2. Potential of mean force decomposition

In the low-density limit, the pair potential or potential of mean force (pmf) between two ions can be computed by simply Boltzmann inverting the radial distribution function [37, 38] and reads

$$\beta w_{ij}(r; \rho) = -\ln[g_{ij}(r; \rho)], \tag{3.11}$$

where $\beta^{-1} = k_\mathrm{B} T$ is the thermal energy.

It turns out to be instructive for the analysis of charged systems to decompose the pmfs (or rdfs) into short-ranged and long-ranged contributions via [29, 30, 40, 139]

$$w_{ij}(r; \rho) = w_{ij}^{\mathrm{sr}}(r; \rho) + w_{ij}^{\mathrm{lr}}(r; \rho), \tag{3.12}$$

where the short-ranged part $w_{ij}^{\mathrm{sr}}(r; \rho)$ is assumed to be salt-density independent. This should be a good approximation as long as ρ is smaller than a critical overlap density ρ^* at which the ion solvation shells around two ion pairs frequently start to interfere due to packing. As a good estimate, the typical extension of the second solvation shell is the location of the second minimum in the ion-water oxygen rdf [14], that is $r_\mathrm{sol} \simeq 0.6$ nm, so that we find roughly $\rho^* = (2r_\mathrm{sol})^{-3} \simeq 1$ M. Thus, for $\rho \lesssim 1$ M we expect the short-ranged pair potential to be quite undisturbed and nearly independent of salt concentration. A weak salt-density dependence of $w_{ij}^{\mathrm{sr}}(r; \rho)$ has been noted in literature previously [139]. With (3.11) and (3.12), we can define a short-ranged structure by

$$g_{ij}^{\mathrm{sr}}(r; \rho) = \exp[-\beta w_{ij}^{\mathrm{sr}}(r; \rho)]. \tag{3.13}$$

The long-ranged part $\beta w_{ij}^{\mathrm{lr}}(r; \rho)$ in (3.12) is typically approximated by a Debye-Hückel (DH) type of potential of the form [11, 40]

$$\beta w_{ij}^{\mathrm{DH}}(r; \rho) = z_i z_j \lambda_{ij}(\rho) \exp[-\kappa(\rho) r]/r, \tag{3.14}$$

which is strictly valid only for infinitely dilute electrolyte systems [40]. Here, z_i is the ion valency and $\lambda_{ij}(\rho)$ is an unknown parameter with unit of length. The density-dependent inverse screening or Debye length is

$$\kappa(\rho) = \sqrt{4\pi\lambda_{\mathrm{B}}(\rho)\rho \sum_{i=\pm} z_i^2} \quad . \tag{3.15}$$

The electrostatic coupling parameter called the Bjerrum length is defined as

$$\lambda_{\mathrm{B}}(\rho) = \frac{\beta e^2}{4\pi\epsilon_0\epsilon(\rho)} \tag{3.16}$$

and is ρ-dependent due to the salt-induced change of the (static) water dielectric constant $\epsilon(\rho)$ [12]. For SPC/E water the dielectric constant is $\epsilon(0) \simeq 72$ [140] and the Bjerrum length has a value of $\lambda_{\mathrm{B}}(0) = 0.78$ nm, roughly 10% larger than the one of real water.

In the low density limit of the salt ($\rho \to 0$), the pmf between two ions reduces to their mutual effective *pair potential*

$$V_{ij}^{\mathrm{eff}}(r) = \lim_{\rho\to 0} w_{ij}(r;\rho), \tag{3.17}$$

which consists of the intrinsic (vacuum) ion-ion interaction and the water mediated contribution. The pmf decomposition (3.12) is then identical to the splitting of the pair potential into a short-ranged and a pure Coulombic part as given by

$$V_{ij}^{\mathrm{eff}}(r) = V_{ij}^{\mathrm{sr}}(r) + z_i z_j \lambda_{\mathrm{B}}(0)/r. \tag{3.18}$$

Recall that for $\rho \lesssim \rho^*$, $w_{ij}^{sr}(r;\rho) \simeq V_{ij}^{sr}(r)$ should hold. We emphasize that in the case of a finite simulation box even the simulation of only a single ion pair is not close to the infinite dilution limit; one ion pair in a 4 nm quadratic box, for instance, results in a density of $\rho \simeq 0.025$ M, above the typical validity range ($\rho \lesssim 10$ mM) of Debye-Hückel (DH) limiting laws [11]. In order to obtain the pair potential (3.17) we thus extrapolate $w_{ij}(r;\rho)$ to the low-density limit as explained in the following.

The accurate calculation of ion-ion pair potentials at infinite dilution in explicit aqueous solutions is problematic as has been pointed out in literature [29, 30, 44, 141]. Typically, problems arise due to the high dilution in a finite-simulation box, yielding sampling problems and unphysical interaction truncations due to the weak electrostatic screening. A better starting point is thus a rdf $g_{ij}(r;\rho)$ at a reasonably high concentration, so that the system is electroneutral, statistics can be gathered conveniently, and the screening length is smaller than the box length, $\kappa(\rho)^{-1} \lesssim L$. On the other hand, the density should be small enough so that the short range structure of the pmf is not disturbed, i.e., $\rho \ll \rho^*$. Nevertheless, small finite size effects will still be observable for low densities (small N_s) far away from the thermodynamic limit ($N_s \to \infty, L \to \infty$), as we already observed in the case of an ideal gas in section 3.1.1. These effects are embodied mainly

in an erroneous normalization of the simulated rdfs, $g_{ij}^{\text{sim}}(r;\rho)$, as has been discussed by Lyubartsev and Marčelja [44]. A correcting factor $f(\rho)$ has to be introduced:

$$g_{ij}(r;\rho) = f(\rho)g_{ij}^{\text{sim}}(r;\rho), \tag{3.19}$$

where $f(\rho)$ should be on the order of $1 \pm 1/N_s$ (cf. section 3.1.1). In order to determine $f(\rho)$ accurately from the simulation rdfs we make use of our knowledge of the asymptotic behavior in r: multiplying the long-ranged interaction (3.14) by r and taking the logarithm of both sides (and allowing just positive arguments), we arrive at

$$\ln[|\beta w_{ij}^{\text{DH}}(r;\rho)r|] = \ln[|z_i z_j \lambda_{ij}(\rho)|] - \kappa(\rho)r, \tag{3.20}$$

where the rhs is a simple, linear function with a negative slope defined by $\kappa(\rho)$ in (3.15). The normalization correction $f(\rho)$ can thus be determined by least-square fitting the lhs of (3.20) to a linear function. The resulting axis intercept of the latter additionally yields $\lambda_{ij}(\rho)$. This procedure allows for correction of the rdfs and pmfs to yield the right asymptotic behavior for small densities $\rho < \rho^*$.

Once the parameters $f(\rho)$ and $\lambda_{ij}(\rho)$ are known, the long-ranged Debye-Hückel part of the interaction can be subtracted from $w_{ij}(r;\rho)$ to yield the short-ranged pair potential via

$$V_{ij}^{\text{sr}} \simeq w_{ij}^{\text{sr}}(r;\rho) = w_{ij}(r;\rho) - w_{ij}^{\text{DH}}(r;\rho), \tag{3.21}$$

where the lhs equality should be valid for $\rho < \rho^*$. The pair potential then follows from (3.18). Note that (3.20) and the above procedure can be equivalently performed on $g_{ij}(r;\rho) - 1$ as it obeys the same long-ranged behavior (3.14) as the pmf [40].

3.2. Dielectric constant

In a polar system, the dielectric constant is directly related to the fluctuations of the total dipole moment $\vec{M}$. The exact form of this relation depends on the geometry of the system. We consider now a *reaction field* geometry, i.e., all interactions between two particles that are farther apart then a certain cut-off radius r_c are approximated by a continuum with dielectric constant ϵ_{RF}, giving rise to the so-called correcting *reaction field* that applies to every particle. For those systems, the dielectric constant ϵ is linked to the total dipole moment $\vec{M}$ in three dimensions by the fluctuations formula [142, 143]

$$\frac{\epsilon - 1}{\epsilon + 2}\left[1 - \frac{\epsilon - 1}{\epsilon + 2}\frac{2\left(\epsilon_{\text{RF}} - 1\right)}{2\epsilon_{\text{RF}} + 1}\right]^{-1} = \frac{\left\langle \vec{M}^2 \right\rangle_t - \left\langle \vec{M} \right\rangle_t^2}{9V k_{\text{B}} T}, \tag{3.22}$$

where the $< \cdots >_t$ are time averages, V is the volume of the system, and T is the temperature. Note that eq. (3.22) does not depend on the radius of the reaction field cut-off r_c. Considering now *conducting boundary conditions*, i.e., $\epsilon_{\text{RF}} \to \infty$, the lhs of (3.22) can be simplified and yields

$$\frac{\epsilon - 1}{3} = \frac{\left\langle \vec{M}^2 \right\rangle_t - \left\langle \vec{M} \right\rangle_t^2}{9 V k_{\mathrm{B}} T}. \qquad (3.23)$$

Rearranging terms gives us

$$\epsilon = 1 + \frac{\left\langle \vec{M}^2 \right\rangle_t - \left\langle \vec{M} \right\rangle_t^2}{3 V k_{\mathrm{B}} T}, \qquad (3.24)$$

where in our MD setup $\vec{M}$ is the total dipole moment of the water molecules and V is the volume of our simulation box.

The reason why we use conducting boundary conditions is of technical nature and lies in the fact that long-range Coulomb interactions are treated in bulk MD simulations with the three-dimensional particle-mesh Ewald summation method [115], as already mentioned in chapter 2. For details, we refer to refs. [109, 115].

We are aware that in a slab geometry, introduced and used in chapter 5, conducting boundary conditions are, unlike in the bulk case, not rigorously satisfied. We will nonetheless assume that this perturbation is not critical in relation to the magnitude of the dielectric constant of bulk water. An additional hindrance of the slab geometry is that the volume accessible to the water molecules is less than the total volume inside the slab and has to be estimated since the repulsive interactions with the walls prevent the water molecules to come too close. We quantify the effective distance perpendicular to the walls accessible to the water molecules as in previous work [144]:

$$d_{wat} = d - \frac{\sigma_{CO} + \sigma_{OO}}{2} = d - 0.335 \text{ nm} \qquad (3.25)$$

with σ_{CO} and σ_{OO} being LJ parameters given in tab. 2.1. The accessible volume, that we use in the calculation of the dielectric constant, is therefore $V_{wat} = L_x \times L_y \times d_{wat}$. We emphasize once more that the calculation of the dielectric constant in our slab geometry in chapter 5 is not exact and is treated as an estimation.

3.3. Shear viscosity

In order to calculate the shear viscosity η of a liquid, we make use of two different methods. On one hand, η is given by the Green-Kubo (GK) formula [40, 145, 146]

$$\eta = \frac{V}{k_{\mathrm{B}} T} \int_0^\infty \langle P_{xz}(t_0) P_{xz}(t_0 + t) \rangle_{t_0} \, \mathrm{d}t, \qquad (3.26)$$

involving the off-diagonal components of the pressure tensor P_{xz} only. Averaged viscosities are obtained over a correlation time of 5 to 20 ps. The latter choice reflects the fact that the viscosity converges rapidly, but exhibits large statistical errors for long correlation times [147].

On the other hand, η can also be calculated by means of a non-equilibrium perturbation method, where we apply an external force [145]. Choosing the external force in a way that

only the $x-$component of the acceleration profile a_x is non-zero and depends on z only, the solution of the Navier-Stokes equation, neglecting pressure gradients in $x-$direction reads

$$\rho\frac{\partial u_x(z)}{\partial t} = \rho a_x(z) + \eta\frac{\partial^2 u_x(z)}{\partial z^2} = 0, \tag{3.27}$$

where $u_x(z)$ is the velocity profile and ρ the concentration of the liquid. An easy way to obtain smooth velocity profiles in our periodically repeated simulation box is to choose the acceleration profile as a cosine function:

$$a_x(z) = A\cos(kz), \tag{3.28}$$

with $k = \frac{2\pi}{L}$, L being the edge length of the simulation box. The amplitude A should be chosen small enough in order not to drive the system out of the linear response regime and at the same time large enough to get good statistics. For a more detailed discussion we refer to [145] and set the amplitude to $A = 0.02$ nm ps^{-2}. The resulting velocity profile then yields

$$u_x(z) = \frac{A\rho}{\eta k^2}\left(1 - e^{-\frac{t\eta k^2}{\rho}}\right)\cos\left(kz\right), \tag{3.29}$$

with the boundary condition $u_z(x) = 0$ for $t = 0$. In an MD simulation, the average velocity profile $u_x(z)$ can be calculated and permits us to evaluate the shear viscosity η [145].

3.4. Thermodynamic routes to the osmotic coefficient

The electrolyte osmotic coefficient is defined as

$$\phi(\rho) = \beta\Pi/(2\rho), \tag{3.30}$$

Π being the osmotic pressure of the electrolyte. The factor 2 in the denominator of (3.30) is due to the total number of ions $N = 2N_s$, where $N_s = N_+ = N_-$ (for a monovalent electrolyte) is defined as both the number of cations and anions in solution. Π can be derived starting from the virial equation as the so-called *virial route* to the osmotic pressure [13, 40, 41]. We will briefly sketch the derivation in the following.

The virial equation reads

$$\Pi V = Nk_{\mathrm{B}}T - \frac{1}{3}\left\langle\sum_{i=1}^{N}\vec{r}_i \cdot \vec{\nabla}V_N\left(\vec{r}^N(t)\right)\right\rangle, \tag{3.31}$$

where the $<\cdots>$ denote an ensemble average and V_N is the interatomic potential energy. With $\frac{N}{V} = 2\frac{N_s}{V} = 2\rho$, one arrives at

$$\frac{\beta\Pi}{2\rho} = 1 - \frac{\beta}{6N_s}\nu_{vir}$$

$$\nu_{vir} = \left\langle \sum_{i=1}^{N} \vec{r}_i \cdot \vec{\nabla} V_N \left(\vec{r}^N(t)\right) \right\rangle. \tag{3.32}$$

The virial contribution to the osmotic pressure ν_{vir} is hard to evaluate. However, if we consider the ions to interact through effective pairwise-additive and density independent forces $\beta F_{ij}(r) = -\frac{\mathrm{d}\beta V_{ij}^{\mathrm{eff}}(r)}{\mathrm{d}r}$ involving infinite dilution pair potentials $V_{ij}^{\mathrm{eff}}(r)$ as in (3.17), one can simplify to

$$\beta\nu_{vir} = \left\langle \sum_{i=1}^{N}\sum_{j>i}^{N} r_{ij} \cdot \frac{\mathrm{d}\beta V^{\mathrm{eff}}(r_{ij})}{\mathrm{d}r} \right\rangle, \tag{3.33}$$

where, for the moment, we ignore the distinction between cations and anions and $r_{ij} = |\vec{r}_{ij}| = |\vec{r}_j - \vec{r}_i|$ is the distance between particle 1 and particle 2. In the canonical ensemble, (3.33) reads

$$\beta\nu_{vir} = \frac{N(N-1)}{2} \iint r_{12} \frac{\mathrm{d}\beta V^{\mathrm{eff}}(r_{12})}{\mathrm{d}r} \left[\frac{1}{Z_N} \int \ldots \int \mathrm{d}\vec{r}_3 \ldots \mathrm{d}\vec{r}_N\right] \mathrm{d}\vec{r}_1 \mathrm{d}\vec{r}_2, \tag{3.34}$$

because the integrals over the double sum in (3.33) yield $N(N-1)/2$ equal terms. With (3.6) and (3.10), one can link the osmotic coefficient to the electrolyte structure:

$$\frac{\beta\Pi}{2\rho} = 1 - \frac{1}{6N_s}\frac{1}{2}\frac{N_s^2}{V^2} \iint g\left(r_{12}; \frac{N_s}{V}\right) r_{12} \frac{\mathrm{d}\beta V^{\mathrm{eff}}(r_{12})}{\mathrm{d}r} \mathrm{d}\vec{r}_1 \mathrm{d}\vec{r}_2 \tag{3.35}$$

When placing particle 1 at the origin—the integration over $\vec{r}_1$ yields V—and integrating over $\vec{r}_{12}$, one obtains

$$\frac{\beta\Pi}{2\rho} = 1 - \frac{1}{12}\frac{N_s}{V} \int g(r_{12}; \rho) r_{12} \frac{\mathrm{d}\beta V^{\mathrm{eff}}(r_{12})}{\mathrm{d}r} 4\pi r_{12}^2 \mathrm{d}r_{12}$$

$$\frac{\beta\Pi}{2\rho} = 1 - \frac{\pi}{3}\rho \int g(r; \rho) r^3 \frac{\mathrm{d}\beta V^{\mathrm{eff}}(r)}{\mathrm{d}r} \mathrm{d}r, \tag{3.36}$$

where we replaced r_{12} by r. As a last step, in order to account for the ion-specific cation-anion, cation-cation, and anion-anion potentials, we have to sum over all contributions and arrive at our final expression, viz.

$$\phi(\rho) = 1 - \frac{\pi}{3}\rho \sum_{i,j=+,-} \int g_{ij}(r; \rho) r^3 \frac{\mathrm{d}\beta V_{ij}^{\mathrm{eff}}(r)}{\mathrm{d}r} \mathrm{d}r. \tag{3.37}$$

The pair-force $\mathrm{d}\beta V_{ij}^{\mathrm{eff}}(r)/\mathrm{d}r$ is in principle density-independent, while the $g_{ij}(r; \rho)$ has to be evaluated at the considered density. The virial route is *not* exact as it employs the

infinite dilution pair potential, and many-body contributions (induced by the water) to the ion-ion interactions for higher densities are not considered. As it has been shown by Hess *et al.*, those contributions can be qualitatively corrected by taking into account the density-dependence of the water dielectric constant $\epsilon(\rho)$ [27]. Here, the long-ranged Coulomb part in the pair potential $V_{ij}^{\text{eff}}(r)$ has to be altered by using $\epsilon(\rho)$ instead of the limit $\epsilon(0)$, to obtain a corrected pair potential [27, 28]

$$\tilde{V}_{ij}^{\text{eff}}(r; \rho) = V_{ij}^{\text{eff}}(r) - \frac{z_i z_j}{r} \left[\lambda_{\text{B}}(0) - \lambda_{\text{B}}(\rho)\right], \tag{3.38}$$

which is now implicitly ρ-dependent and has to be used in (3.37) instead. The necessary input parameter $\epsilon(\rho)$ can directly be calculated from our all-atom MD simulations using eq. (3.24).

An advantage of the virial route is that it allows us to investigate and analyze short-ranged and long-ranged contributions to the virial separately by splitting the pair potential as in (3.18). We can thus write

$$\phi_v(\rho) = 1 - \frac{\pi}{3}\rho \sum_{i,j} \int_0^\infty g_{ij}(r; \rho)\frac{\mathrm{d}}{\mathrm{d}r}\left[\beta V_{ij}^{sr}(r) + \beta V_{ij}^{\text{DH}}(r)\right] r^3 \mathrm{d}r \tag{3.39}$$

$$= 1 + \Delta\phi^{sr} + \Delta\phi^{\text{DH}},$$

where $\Delta\phi^{sr} = \sum_{i,j} \Delta\phi_{ij}^{sr}$ and $\Delta\phi^{\text{DH}} = \sum_{i,j} \Delta\phi_{ij}^{\text{DH}}$ are the partial corrections to the osmotic coefficient due to the short and long-ranged virial contributions of every ion pair ij, respectively.

The second route to the osmotic coefficient makes use of the link between the compressibility χ_T and microscopic particle fluctuations in the grand canonical ensemble and is called the *compressibility route*. Here, the full electrolyte structure in terms of interionic rdfs is directly related to the electrolyte isothermal compressibility [40]

$$\chi_T = \left(\rho \frac{\partial \Pi}{\partial \rho}\right)^{-1}. \tag{3.40}$$

The link to electrolyte structure is provided by the compressibility rule (sometimes called Kirkwood-Buff formula), which can be written for a binary mixture with components $i, j = 1, 2$ as [39, 40]

$$2\rho k_B T \chi_T = \frac{1 + \rho(G_{11} + G_{22}) + \rho^2 \left(G_{11}G_{22} - G_{12}^2\right)}{1 + \rho \left(G_{11} + G_{22} - 2G_{12}\right)/2} \tag{3.41}$$

and is expressed by integrals over the structure, namely, the Kirkwood-Buff factors [39]

$$G_{ij} = 4\pi \int_0^\infty [g_{ij}(r; \rho) - 1]r^2 \mathrm{d}r. \tag{3.42}$$

A complete and detailed derivation of (3.41) can be found for example in ref. [148] and will not be repeated here. However, we want to point out that the water-water and
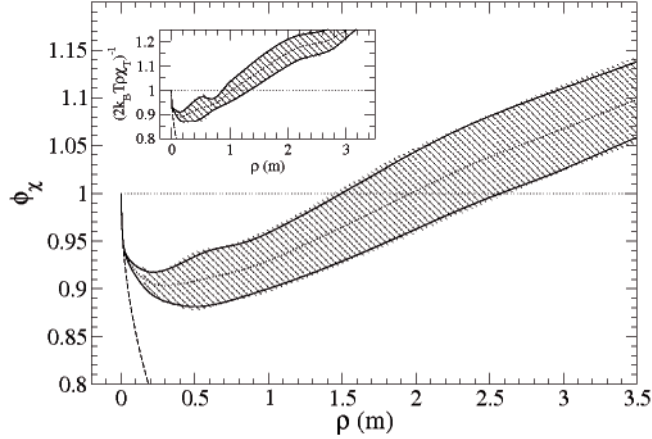
Figure 3.2.: *Illustration of the compressibility route to the osmotic pressure and its error estimate for NaCl. The inset shows the calculated inverse compressibility $(2k_BT\rho\chi_T)^{-1}$ vs. density ρ calculated from the Kirkwood-Buff formula (3.41). The curves enclosing the shaded region are upper and lower estimates obtained from the statistical errors of the rdfs (see text) and spline procedure. The central line is the average and is considered the result. Integration leads to the osmotic coefficient $\phi_\chi(\rho)$ with an error given by the shaded region. Note that DH limiting laws are employed for $\rho < 10$ mM (dashed lines).*

water-ion interactions are *not* included in the calculation of the osmotic coefficient and our binary mixture consists of cations and anions only. Eq. (3.41) can be integrated using (3.40) to obtain the osmotic coefficient from the compressibility route $\phi_\chi(\rho)$. It is in principle exact, i.e., an accurate knowledge of the structure at every density allows for the calculation of the compressibility without underlying assumptions. In practice, however, we have to evaluate the compressibility (3.41) at discrete densities and then interpolate it. As the structure at small densities is hardly accessible due to weak computational sampling, in the limit $\rho \to 0$ it is necessary for the interpolation and subsequent integration of (3.41) to include the analytic DH limiting behavior. The DH limiting law for the osmotic coefficient can be easily derived from a virial integration over DH forms starting with (3.37) and reads [11, 149]

$$\phi_{\mathrm{DH}}(\rho) = \left[1 - \frac{\kappa(\rho)^3}{48\pi\rho} \right]. \tag{3.43}$$

Relation (3.40) leads to the DH limiting law for the compressibility

$$2\rho k_{\mathrm{B}}T\chi_{\mathrm{DH}} = [1 - \kappa(\rho)\lambda_{\mathrm{B}}(0)/4]^{-1}, \tag{3.44}$$

where we neglected the density-dependence of the dielectric constant. The integrals leading to (3.43) and (3.44) are carried out in detail in appendix A. We complement thereby our MD results by data in the validity range of the DH limiting law, $\rho \leq 10$ mM. Interpolations are performed using an Akima spline [150]. For densities $\rho < \rho^*$ the integration of the compressibility equation (3.41) is performed beyond the simulation box limits by extending the rdfs and pmfs using the long-ranged form (3.14). A representative

result of the compressibility route to ϕ_χ is shown in fig. 3.2 on the previous page, where we anticipate MD results that will be presented in chapter 4. Integration of the splined compressibility data leads to a continuous plot of the osmotic coefficient $\phi_\chi(\rho)$. The error (shown as shaded area in fig. 3.2) is related on one hand to the statistical variance of the correcting factors $f(\rho)$ and $\lambda_{ij}(\rho)$ (mainly for $\rho < 1\ M$) and on the other hand to the statistical precision of each rdf. To compare those osmotic coefficients with the ones obtained from experiments or the virial route, we choose discrete points of our continuous plot and set the error bars according to the variance in the integration.

3.5. Barker-Henderson mapping onto hard spheres and nonadditivity

The ion-ion short-range pmfs $V_{ij}^{\mathrm{sr}}(r)$ exhibit oscillations on a $k_\mathrm{B}T$ energy scale due to hydration effects. As it is computationally easier and more convenient to deal with hard-spheres (HS) we intend to map the intricate ion-ion interactions onto simple HS interactions. We use therefore the Barker-Henderson (BH) scheme which relates the short-ranged pair potentials $V_{ij}^{\mathrm{sr}}(r)$ to an effective hard-core diameter via [40, 151]

$$\sigma_{ij} \;=\; - \int \mathrm{d}r\, f_{ij}(r), \tag{3.45}$$

the subscripts $i, j = +, -$ specifying cations or anions, which consists of a one-dimensional integral over the Mayer-function of the short-ranged pair potentials

$$f_{ij}(r) \;=\; \left[\exp\left(-\beta V_{ij}^{\mathrm{sr}}(r)\right) - 1\right]. \tag{3.46}$$

Our HS system can be *asymmetric*, i.e., $\sigma_{++} \neq \sigma_{--}$, and additionally *nonadditive*. We define the nonadditivity by

$$\sigma_{+-} = \frac{1}{2}\left(\sigma_{++} + \sigma_{--}\right) \times \left(1 + \Delta_{+-}\right) \tag{3.47}$$

with a nonadditivity parameter $\Delta_{ij} \neq 0$. It is well known that nonadditivity strongly influences fluid structure and phase behavior in binary hard-sphere mixtures [152, 153]. $\Delta_{ij} > 0$ results in an increasingly repulsive cross-correlation and can lead to stable fluid-fluid demixing transitions even at small positive values $\Delta_{ij} = 0.2$ [154, 155]. $\Delta_{ij} < 0$ not only entails a significantly lesser correlated system but can cause partial clustering as observed experimentally in superparamagnetic colloidal suspensions [156].

3.6. DFT approximations for electrolytes

3.6.1. Introduction

In density functional theory equilibrium one-particle densities are obtained via minimization of a grand potential functional Ω [40]. Thus, the equilibrium ion densities ρ_i

satisfy the variational principle $\frac{\delta\Omega[\rho_+,\rho_-]}{\delta\rho_i} = 0$. The grand potential functional of charged particles has the general form

$$\Omega[\rho_+,\rho_-] = F[\rho_+,\rho_-] - \sum_i \int \left[\mu_i - V_i^{ext}(\vec{r})\right]\rho_i(\vec{r})\,\mathrm{d}\vec{r}, \tag{3.48}$$

where $V_i^{ext}(\vec{r})$ is the external potential acting on ions of species $i = \pm$, μ_i is the chemical potential, and F is an intrinsic free-energy functional of the one-particle densities. F is typically split into ideal and excess parts via

$$F[\rho_+,\rho_-] = \sum_i F_i^{\mathrm{id}}[\rho_i] + F^{ex}[\rho_+,\rho_-] \tag{3.49}$$

with the ideal contribution $F^{id}[\rho_i] = k_\mathrm{B}T \int \rho_i\left(\vec{r}\right)\left(\ln\left[\Lambda^3\rho_i(\vec{r})\right] - 1\right)\mathrm{d}\vec{r}$, Λ being the de Broglie thermal wavelength, and an excess contribution F^{ex}, which we assume can be separated into a mean-field, purely Coulombic and a correlation part:

$$F^{ex}[\rho_+,\rho_-] = \frac{k_\mathrm{B}T}{2}\lambda_\mathrm{B}\iint \frac{\rho(\vec{r})\,\rho(\vec{r}')}{|\vec{r} - \vec{r}'|}\mathrm{d}\vec{r}\,\mathrm{d}\vec{r}' + F^{corr}[\rho_+,\rho_-] \tag{3.50}$$

with

$$\rho(\vec{r}) = z_+\,\rho_+(\vec{r}) + z_-\,\rho_-(\vec{r}) \tag{3.51}$$

as the charge density.

Minimizing the grand potential Ω with respect to ρ_i in a one-dimensional slab geometry leads to

$$\rho_i(z) = \xi_i \exp\left[-\beta\left(z_i\,e\,\psi(z) + V_i^{ext}(z)\right) + c_i(z)\right] \tag{3.52}$$

with the activity $\xi_i = \exp(\beta\mu_i)/\Lambda_i^3$ of species i, $\psi(z)$ being the local electrostatic potential and

$$c_i(z) = -\frac{\delta(\beta F^{corr})}{\delta\rho_i} \tag{3.53}$$

the one-particle direct correlation function [40]. For fixed $\rho_i(z)$, the electrostatic potential satisfies Poisson's equation

$$e\,\beta\,\frac{\partial^2\psi(z)}{\partial^2 z} = -4\,\pi\,\lambda_\mathrm{B}\,\rho(z). \tag{3.54}$$

The boundary conditions link the charge density σ to the first derivative of the electrostatic potential:

$$e\beta\,\frac{\partial\,\psi(z)}{\partial\,z} = -4\,\pi\,\lambda_\mathrm{B}\,\frac{\sigma}{e}. \tag{3.55}$$

3.6.2. PB in DFT

Neglecting correlations ($c_i(z) = 0$) eqs. (3.51), (3.52) and (3.54) yield the standard mean-field Poisson-Boltzmann (PB) equation. Note that in this definition, the external potential $V_i^{ext}(z)$ is still included:

$$e\beta\frac{\partial^2\psi(z)}{\partial^2 z} = -4\pi\lambda_{\mathrm{B}}\sum_{i=+,-}z_i\xi_i\exp\left[-\beta\left(z_ie\psi(z) + V_i^{ext}(z)\right)\right]. \qquad (3.56)$$

When referring to the PB solution in this work, we apply eq. (3.56).

In the *special case* of hard walls, i.e., $V_i^{ext}(z)\begin{cases}\infty & \text{for } z < 0 \\ 0 & \text{for } z > 0\end{cases}$, eq. (3.56) can be further simplified to

$$e\beta\frac{\mathrm{d}^2\psi(z)}{\mathrm{d}^2 z} = 8\pi\lambda_{\mathrm{B}}\rho_0\sinh\left(\beta e\psi(z)\right) = \kappa^2\sinh\left(\beta e\psi(z)\right), \qquad (3.57)$$

where $\kappa = \sqrt{8\pi\lambda_{\mathrm{B}}\rho_0}$ is the inverse screening lenght. For small enough surface charges the rhs of (3.57) can be linearized [149], leading to

$$e\beta\frac{\mathrm{d}^2\psi(z)}{\mathrm{d}^2 z} = \kappa^2 e\beta\psi(z). \qquad (3.58)$$

In the following, we will examine local- and nonlocal approximations for the correlation free energy $F^{corr}[\rho_+, \rho_-]$ (second term in the rhs of (3.50)) and $c_i(z)$ of (3.53). We will, in the last part of this section, also explain how electrostatic correlations can be included by modifying the Coulombic mean-field term on the rhs of (3.50).

We want to point out that in DFT one can easily switch from a canonical to a grand canonical description. In the canonical ensemble (fixed number of particles) we fix the ion area density τ. In the grand canonical ensemble (fixed chemical potential or reservoir density ρ_0) the activity is specified along with the chemical potential. In the case of PB we get $\xi_i = \rho_0$.

3.6.3. Poisson-Fermi

One way to extend PB to consider steric interactions in a local way is to derive the free energy functional from a lattice gas model [157]. For monodisperse systems each ion occupies a site using a certain excluded-volume and inhibiting other ions to occupy that site. It can easily be extended to a polydisperse system by Taylor-expanding the free space entropy [158]. Incorporating the effective ion-wall potentials finally yields for a one-dimensional confinement the so-called Poisson-Fermi (PF) distribution:

$$\beta e\frac{\partial^2\psi(z)}{\partial^2 z} = -4\pi\lambda_{\mathrm{B}}\,\bar{\rho}\,\frac{\sum_i z_i\exp\left(z_ie\beta\psi(z) - V_i^{ext}(z)\right)}{1 - \bar{\rho}\sum_i \sigma_{ii}^3\left(1 + \exp\left(z_ie\beta\psi(z)\right)\right)} \qquad (3.59)$$

with the effective density $\bar{\rho} = \frac{\tau}{d}$, where τ is the ion area density, d the plate separation and the σ_{ii} are the effective cation-cation and anion-anion BH diameters. Note that the cation-anion BH diameters do not enter in (3.59).

3.6.4. Local density approximation for nonadditive hard-spheres

In the framework of DFT local extensions to PB can be employed by using the local density approximation (LDA) [40]. In the LDA, the correlation excess free energy is given by an integral over a local excess free energy f^{corr} per volume of a homogeneous solution of density ρ:

$$F^{corr}[\rho] = \int \mathrm{d}\vec{r}\, f^{corr}(\rho). \tag{3.60}$$

As we showed before, after subtracting electrostatic interactions, ions resemble asymmetric and nonadditive HS mixtures. Thus f^{corr} should describe the free energy of a binary, asymmetric and nonadditive HS mixture for 1:1 salts. As there is no closed accurate expression available, we resort to a virial expansion of f^{corr} up to third order given by [159]:

$$\beta\, f^{corr} = \sum_{ij} \rho_i\, \rho_j\, B_2^{ij} + \frac{1}{2} \sum_{ijk} \rho_i\, \rho_j\, \rho_k\, B_3^{ijk}$$

with the virial coefficients

$$B_2^{ij} = \frac{2}{3}\,\pi\sigma_{ij}^3$$
$$B_3^{ijk} = \frac{4}{3}\left(\frac{\pi}{6}\right)^2 \left(c_{k;ij}\,\sigma_{ij}^3 + c_{j;ik}\,\sigma_{ik}^3 + c_{i;jk}\,\sigma_{jk}^3\right)$$
$$c_{k;ij} = \sigma_{k;ij}^3 + \frac{3}{2}\frac{\sigma_{k;ij}^2}{\sigma_{ij}}\,\sigma_{i;jk}\,\sigma_{j;ik}$$
$$\sigma_{k;ij} = \sigma_{ik} + \sigma_{jk} - \sigma_{ij} \tag{3.61}$$

where $\sigma_{k;ij}$ is interpreted as an effective diameter of sphere k as seen from the pair i and j. We will refer to the second order virial expansion as B2 and to the third order virial expansion as B3 in the following.

The direct correlation function now follows from the first functional derivative of the correlation term of the excess free energy:

$$\frac{\delta\left(\beta\, F^{corr}\right)}{\delta\rho_i} \;=\; -c_i(z) \;=\; 2\sum_j \rho_j\, B_2^{ij} + \frac{3}{2}\sum_{jk} \rho_j\, \rho_k\, B_3^{ijk}. \tag{3.62}$$

The correction to PB theory is local in terms of the fact that the correlation function depends on the amplitude of the *local* density only.

3.6.5. Nonlocal PB and its hard-sphere versions (NPB-HS)

As a starting point to the nonlocal treatment of the correlation term of the excess energy we will introduce a coarse-grained density $\tilde{\rho}(\vec{r})$ defined through an appropriately chosen, a priori unknown, normalized weight function $w(\vec{r})$ as $\tilde{\rho}(\vec{r}) \;=\; \int w\left(|\vec{r} - \vec{r}'|\right)\rho(\vec{r}')\,\mathrm{d}\vec{r}'$. Eq. (3.60) then reads

$$F^{corr}[\rho] \;=\; \int \phi^{ex}(\tilde{\rho})\,\rho(\vec{r})\,\mathrm{d}\vec{r} \tag{3.63}$$

where $\phi^{ex}(\tilde{\rho}) = f^{corr}(\tilde{\rho})/\tilde{\rho}$ is the excess free energy per particle of the homogeneous fluid at a density $\tilde{\rho}$ [40]. Eq. (3.63) represents a weighted-density approximation (WDA). In the low density limit, the leading term of the virial expansion yields $\phi^{ex}(\rho) = k_{\mathrm{B}}T\,\rho\,B_2$, with B_2 being the second virial coefficient [40]. As B_2 is defined by the Mayer-function shown in eq. (3.46), viz. $B_2 = -\frac{1}{2}\int f(r)\,\mathrm{d}\vec{r}$, we obtain the nonlocal expression [40]:

$$\beta F^{corr}[\rho_+,\rho_-] \;=\; -\frac{1}{2}\sum_{ij}\iint \mathrm{d}\vec{r}\,\mathrm{d}\vec{r}'\rho_i(z)\,\rho_j(z')\,f_{ij}\left(\left|\vec{r}-\vec{r}'\right|\right). \tag{3.64}$$

We emphasize that in our assumption F^{corr} approximates the excess free energy of a binary fluid interacting with the short-ranged pair potentials $V_{ij}^{sr}(r)$. Explicit Coulombic correlations, which become important at high electrostatic coupling, are therefore neglected.

The direct correlation function is now given by convolutions of the density profile over the Mayer-functions of the short-ranged potentials:

$$c_i(z) \;=\; \sum_j \int \mathrm{d}\vec{r}'\rho_j(z')f_{ij}\left(\left|\vec{r}-\vec{r}'\right|\right). \tag{3.65}$$

In the case of hard-spheres the Mayer-function degenerates into a shifted Heaviside step function $f_{ij}(r) = \Theta(\sigma_{ij}-r)-1$. Convolutions over step functions are easier and faster to compute than convolutions over the Mayer-function of the full short-ranged potential. In the following we will refer to NPB-HS when using this HS expression with the effective BH diameters of tab. 4.3 and to NPB when employing the MD derived short-range potentials V_{ij}^{sr} described in chapter 4.

When we refer to the grand canonical ensemble with a given reservoir density ρ_0 we choose the activities ξ_i of eq. (3.52) in a way that the electrolyte concentration in the middle of the slab matches ρ_0 in the limit of infinite wall-to-wall distances d. This activity depends on the direct correlation functions c_i [160].

We are aware that in the realm of DFT Rosenfeld's *fundamental-measure theory* (FMT) [161] is a more elaborate way to treat hard-sphere fluids nonlocally. The relevant generalization of FMT to nonadditive binary HS mixtures has been developed by Schmidt and applied to a broad range of nonadditivities [162, 163]. Nonetheless, as FMT involves a decomposition of the Mayer-function and requires a very sophisticated treatment [164], we content ourselves with our NPB and NPB-HS theories in the following.

3.6.6. An attempt to include electrostatic correlations: NPB-el

For low salt densities and high ion valencies electrostatic correlations dominate excluded-volume correlations [74]. In our DFT-PB picture, these correlations must be included by modifying the mean-field Coulombic term in the rhs of eq. (3.50). In principle, this can

be done exactly by means of ion-ion rdfs $g(r)$s. The Coulombic free energy term then reads:

$$F_{coul}^{ex}[\rho_+, \rho_-] = \frac{k_B T}{2} \lambda_B \iiint \frac{\rho(\vec{r})\,\rho(\vec{r'})\,g(|\vec{r}-\vec{r'}|;\alpha)}{|\vec{r}-\vec{r'}|}\, d\vec{r}\,d\vec{r'}\,d\alpha, \qquad (3.66)$$

where the integration over α "turns on" the interaction. As we already saw in section 3.1.1, the $g(r)$s are in general (for electrolytes for example) not mean-field like, i.e., constant at $g(r) = 1$ for all values of r, and feature intricate oscillations before converging to 1 for $r \to \infty$. It is therefore difficult to treat (3.66) analytically. In order to simplify, lets assume that the rdf for the interaction $z_i z_j \alpha \lambda_B / r$ is given by a simple Debye-Hückel form

$$g(r;\alpha) = \exp(-z_i z_j \alpha \frac{\lambda_B}{r} e^{-\sqrt{\alpha}\kappa r}). \qquad (3.67)$$

We can then Taylor-expand the exponential. Inserting (3.67) in (3.66), the first term in the Taylor-expansion will yield the mean-field expression of eq. (3.50). The other terms have to be integrated over α:

$$\int_0^1 d\alpha \sum_{n=1}^{\infty} a_n \alpha^n \exp(-n\sqrt{\alpha}\kappa r) = 2\sum_{n=1}^{\infty} a_n(r) C_n(r) \qquad (3.68)$$

with $a_n = \frac{1}{n!}(-z_i z_j \lambda_B / r)^n$. The $C_n(r)$ are, after carrying out simple integrations shown in more detail in appendix B, given by

$$C_n(r) = \frac{(2n+1)!}{(n\kappa r)^{2n+2}} \left(1 - e^{-n\kappa r} \sum_{m=0}^{2n+1} \frac{(n\kappa r)^m}{m!}\right). \qquad (3.69)$$

The approximation is valid for distances above $(n\kappa)^{-1}$, a value that represents the inverse screening lenght in the Taylor-expansion. Thus, the expansion must be performed up to the order $n \simeq (\kappa\sigma)^{-1}$, where σ defines the hard-core cutoff distance for the considered ions. Numerically, this approach consists in using in eq. (3.52) a convolution with the hard-core functional of eq. (3.65) for $|\vec{r}-\vec{r'}| < \sigma$, and with

$$\tilde{c}_i(z) = \sum_j \int d\vec{r'} \rho_j(z') z_i z_j \frac{2\lambda_B}{|\vec{r}-\vec{r'}|} \sum_{n=1}^{n_{max}} a_n C_n(|\vec{r}-\vec{r'}|) \qquad (3.70)$$

for $|\vec{r}-\vec{r'}| > \sigma$, where the z_i are ion valencies. We typically use an order of $n_{max} = 12$ in the Taylor-expansion. If we make use of $\tilde{c}_i(z)$ in the following, especially in section 3.9, we will refer to the NPB-el method.

3.7. Solvation forces

We place two infinitely large surfaces in an ionic reservoir of concentration ρ_0, meaning that the chemical potential μ_0 of the electrolyte inside the slab is equal to the chemical potential in the reservoir. We compute solvation (s) forces by calculating the difference

of the "internal" pressure between the surfaces and the "external" bulk pressure of the reservoir. The bulk pressure is given by the "internal" pressure in the limit of infinite surface separations $d \to \infty$ [165]. We obtain thus for the solvation pressure:

$$P_{\mathrm{s}}(d) = [P(d) - P(\infty)]. \tag{3.71}$$

To calculate the internal ionic pressure, typically a contact theorem can be derived by differentiating the free energy with respect to the surface separation [160, 166]. We use here a somewhat more general expression [167], viz.

$$\frac{\partial p(z)}{\partial z} \; + \; \sum_i z_i \rho_i(z) \frac{\partial \psi(z)}{\partial z} \; + \; \sum_i \rho_i(z) \frac{\partial V_i^{ext}(z)}{\partial z} \; = \; 0, \tag{3.72}$$

where p is the local pressure along the $z-$axis and ψ is the electrostatic potential introduced before. By replacing the density in the second term by the Poisson equation, eq. (3.54), and integrating from $z = 0$ to $z = d$ we see that, given the boundary conditions of eq. (3.55), the second expression vanishes and the total ionic pressure on one wall inside the slab simply is

$$P(d) \; = \; - \sum_i \int_0^d \mathrm{d}z \, \rho_i(z) \, \frac{\partial V_i^{ext}(z)}{\partial z}. \tag{3.73}$$

We are then enabled to investigate the impact of steric ion-ion excluded-volume correlations by comparing the results of the PB and NPB-HS methods, viz.

$$\Delta P_{\mathrm{s}}(d) = P_{\mathrm{s}}^{\mathrm{NPB-HS}}(d) - P_{\mathrm{s}}^{\mathrm{PB}}(d), \tag{3.74}$$

which is the *steric correction* to the solvation pressure. We can integrate again to obtain the steric correction to the interaction between the surfaces:

$$\Delta V_{\mathrm{s}}(d) = -A \int_d^\infty \mathrm{d}d' \, \Delta P_{\mathrm{s}}(d') \tag{3.75}$$

for a unit area of A.

3.8. Salt expulsion: Donnan effect

When two plates in contact with a (much larger) electrolyte reservoir of density ρ_0 are charged with an identical uniform charge density, counterions will be attracted to the surfaces in order to ensure electroneutrality, as has been anticipated at the end of the previous chapter. Coions on the other hand will be repelled by the latter. The salt, which has by definition the same concentration as the coions, is therefore expelled from the slab with increasing surface charge. This so-called *Donnan effect* can be treated analytically with a linearized Poisson-Boltzmann equation in the case of an ideal gas and hard walls [149]. Our coarse-grained PB and NPB-HS theories (in the grand canonical ensemble) permit us then to examine the impact of ion-ion excluded-volume correlations

and ion-surface interactions on the Donnan effect. We compare results for LiCl and NaI in the following for positive and negative surface charges and a reservoir density of $\rho_0 = 3$ M.

In the case of an ideal gas, i.e., point charge particles, and (structureless) hard walls the PB equation can be linearized for sufficiently low surface charges. Even though hardly being a new result we treat this case quickly as a starting point for clarity. Our starting point is the linearized PB equation shown in eq. (3.58). The boundary conditions are given by the surface charge density at the surface σ and by the electroneutrality condition in the middle of the slab and read

$$\frac{\mathrm{d}\psi}{\mathrm{d}z}\bigg|_{z=d/2} = 0 \qquad -\frac{\mathrm{d}\psi}{\mathrm{d}z}\bigg|_{z=0} = 4\pi\lambda_{\mathrm{B}}\frac{\sigma}{e}, \tag{3.76}$$

d being the width of the slab. The solution of eq. (3.58) satisfying the latter boundary conditions is [149]

$$\psi(z) = \frac{4\pi\,\lambda_{\mathrm{B}}\,(\sigma/e)}{\kappa\sinh(\kappa d/2)}\cosh(\kappa z), \tag{3.77}$$

$\kappa = \sqrt{8\pi\,\lambda_{\mathrm{B}}\,\rho}$ being the inverse screening length. In our simple model system, the salt concentration is given by the Boltzmann distribution $\rho_{\pm}(z) = \rho_{\pm}\exp\left(\mp\beta e\psi(z)\right)$. We can thus write

$$\bar{\rho}_s = \frac{1}{d}\int_0^d \rho_{\pm}\exp\left(\mp\beta e\psi(z)\right)\mathrm{d}z = \frac{\tau}{d}, \tag{3.78}$$

where the $\pm$ sign refers to the two distinct cases of positively or negatively charged coions. For an ideal gas and hard walls the two cases are equal. We will consider the first- and second-order terms in the Taylor-expansion of the exponential in eq. (3.78). The first order term is proportional to σ; the second order term is proportional to σ^2. The expansion up to second order in $|\sigma|$ finally yields

$$\bar{\rho}_s \simeq \rho_0\left[1 - \left(\frac{|\sigma|}{e}\right)\frac{1}{\rho_0 d} + \left(\frac{|\sigma|}{e}\right)^2\left(\frac{(4\pi\lambda_{\mathrm{B}})^2}{2d\kappa^3}\coth\left(\frac{\kappa d}{2}\right) + \frac{(4\pi\lambda_{\mathrm{B}})^2}{8\kappa^3}\frac{1}{\sinh^2\left(\frac{\kappa d}{2}\right)}\right)\right]. \tag{3.79}$$

In the inset of fig. 5.6(a) on page 61 we show, for $d = 2$ nm, how the salt concentration in the slab depends on the absolute value of the surface charge density. The sign of the latter does indeed not change the result in the case of an ideal gas. At $\sigma = 0$ the mean salt concentration equals the concentration in the reservoir ρ_0. The salt concentration decreases then with the surface charge. This decrease is linear in σ only for small surface charge densities up to $0.2\ e\ \mathrm{nm}^{-2}$. By including the second term in the Taylor-expansion we are able to reproduce the numerical result up to surface charge densities of $0.8\ e\ \mathrm{nm}^{-2}$.

3.9. Contact potential at charged interface: Grahame equation

In this section we will shortly examine the impact of electrostatic correlations on highly charged systems. Inspired by recent experimental observations that report non-DLVO behavior for the interaction of colloidal spheres in the presence of multivalent ions [168], we investigate the electrostatic potential near a highly negatively charged wall in presence of mono- and divalent counterions by means of the NPB-el method presented in section 3.6.6.

We first treat for descriptive reasons the case of an ideal monovalent gas and a hard wall because of its simplicity. The respective PB equation is shown in eq. (3.57). The hard wall is charged with a surface density of σ and is at contact with a salt reservoir of concentration ρ_0. Thus, the two boundary conditions at contact and infinitely far away from the surface are

$$\lim_{z \to \infty} \frac{\mathrm{d}\psi}{\mathrm{d}z} = 0 \qquad - \frac{\mathrm{d}\psi}{\mathrm{d}z}\bigg|_{z=0} = 4\pi\lambda_{\mathrm{B}}\frac{\sigma}{e}. \tag{3.80}$$

Integrating (3.57) using (3.80) leads to

$$e\beta\psi(z) = 4\operatorname{arctanh}\left[\tanh\left(\frac{\beta e\psi_0}{4}\exp(-\kappa z)\right)\right], \tag{3.81}$$

$\kappa = \sqrt{8\pi\lambda_{\mathrm{B}}\rho_0}$ being the inverse screening lenght and $\psi_0 = \psi(z = 0)$ being the electrostatic potential at contact with the wall. The relation between the surface charge density and the electrostatic potential at contact is now obtained via the boundary conditions and yields the Grahame equation [72, 149]:

$$\frac{\sigma}{e} = \left(\frac{2\rho_0}{\pi\lambda_{\mathrm{B}}}\right)^{\frac{1}{2}}\sinh\left(\frac{\beta e\psi_0}{2}\right). \tag{3.82}$$

This equation is exact for our model system. Rearranging terms leads to

$$e\beta\psi_0 = 2\operatorname{arcsinh}\left[\frac{\sigma}{e}\sqrt{\frac{\pi\lambda_{\mathrm{B}}}{2\rho_0}}\right]. \tag{3.83}$$

We investigate now similar systems numerically. We treat a negatively charged wall with a constant surface charge density of $\sigma/e = -1\,\mathrm{nm}^{-2}$ in contact with a salt reservoir of mono- and divalent counter- and monovalent coions—with coion concentration ρ_0—by means of PB and NPB-el. The ions are modeled in NPB-el as symmetric and additive HS spheres of diameter 0.3 nm. As a reminder, we choose in NPB-el, equivalently to NPB-HS, the activities ξ_i of eq. (3.52) in order to match the coion concentration ρ_0 far away from the wall. We probe additionally the influence of a simple attractive model box ion-wall potential.

Fig. 3.3(a) on page 34 shows results for monovalent counterions. We first observe that for all cases, the electrostatic potential at a distance $\Delta z = 0.3$ nm from the wall is shifted

and less negative than the one at contact with the wall. A similar shift is induced by the attractive ion-wall box potential. Comparing results for PB and NPB-el, we find that electrostatic correlations increase the contact potential, i.e., shifting it to less negative values. The latter increase is however small. Indeed, the contact value of the potential for $\Delta z = 0$ calculated with NPB-el is very similar to the analytic mean-field result of eq. (3.83), shown as the black full line in fig. 3.3(a).

We turn now our attention to divalent ions and focus on hard walls. In fig. 3.3(b) we recover on one hand the shift in contact potential to higher values for $\Delta z = 0.3$ nm compared to $\Delta z = 0$. On the other hand, we notice that the results for NPB-el differ strongly from PB. In the former case, ψ_0 exhibits a steep increase for concentrations $\rho_0 < 0.05$ nm^{-3} and converges then rapidly to an equilibrium value. For PB, ψ_0 shows the same slow increase as observed for monovalent counterions.

We conclude that electrostatic correlations have a minor impact for monovalent counterions. For divalent counterions, however, we observe that the electrostatic contact potential of a highly negatively charged wall increases rapidly with salt concentration already at concentrations in the millimolar range. The latter points to strong charge compensation due to electrostatic correlations for multivalent counterions.
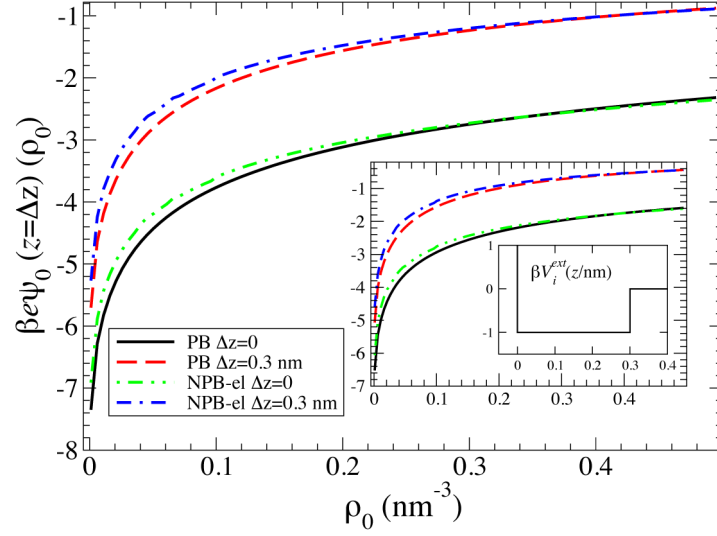
(a) Monovalent counterions. Eq. (3.83) is drawn as black continuous line (PB $\Delta z = 0$ in the legend). Inset: Results with depicted attractive model box ion-wall potential for both co- and counterions.
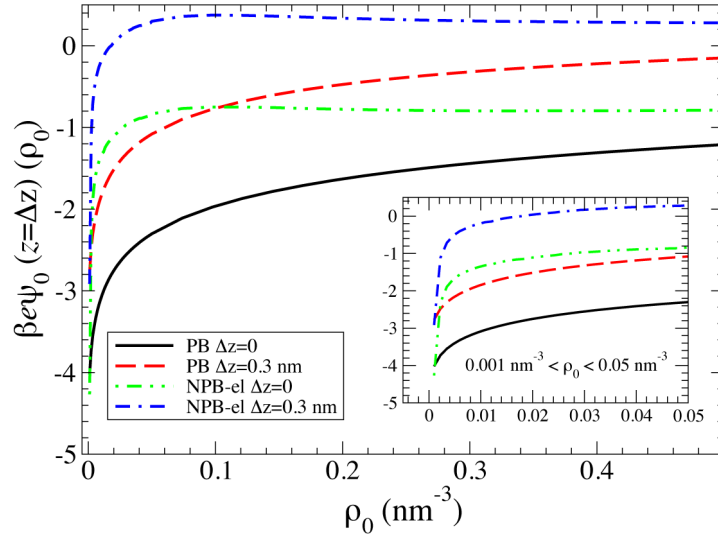
(b) Divalent counterions. Inset: Zoom on low reservoir densities.

Figure 3.3.: *Electrostatic potential next to a highly charged hard wall plotted with respect to the salt reservoir concentration. The contact potential is defined as either at direct contact with the wall or at a distance $\Delta z = 0.3$ nm, corresponding to the size of the counterions. The surface charge is $\frac{\sigma}{e} = -1 \, nm^{-2}$.*

Chapter 4

Structure-Thermodynamics Relation of Electrolyte Solutions

This chapter addresses ion-specific thermodynamic properties of bulk aqueous electrolytes. For this, we will first compute ion-specific radial distribution functions out of explicit-water MD simulations of bulk electrolytes. We will then calculate effective short-range ion-ion potentials of mean force (pmfs) and deduce Barker-Henderson diameters for every ion-ion combination. We furthermore compute osmotic coefficients for the studied electrolytes by the compressibility and the virial route up to high salt concentrations of $\simeq 6$ M. In the latter route we will employ a correction via a concentration dependent dielectric constant, that we additionally extract from our simulations and compare to experiments. The virial route permits us to inspect short-ranged cation-anion, anion-anion and cation-cation, as well as long-ranged Debye-Hückel contributions to the osmotic coefficient separately. Finally, we will calculate bulk shear viscosities by means of fluctuation formulas at salt concentrations of $\simeq 3.5$ M.

4.1. Ion-specific electrolyte structure

4.1.1. Ion-specific rdfs

In our bulk MD simulations, the ion-ion radial distribution functions $g_{ij}(r; \rho)$ of eq. (3.10) are evaluated by standard probability histograms. Examples of $g_{ij}(r; \rho)$s for concentrations up to $\rho = 4$ M including the low-density limit $\rho \to 0$ are presented in fig. 4.1 on page 38 for LiCl, NaCl, NaI, KF, KCl and CsCl. For $\rho \to 0$, all salts show the expected, long-ranged $\propto \exp(\pm \lambda_\mathrm{B}(0)/r)$ decay for Coulomb interactions. Already at $\rho = 0.3$ M the curves exhibit a strong electrostatic screening and the rdfs reach the asymptotic value of 1 below $r \simeq 2$ nm, consistent with the small decay length of $\kappa^{-1} \simeq 0.5$ nm. The short-ranged oscillations hardly change qualitatively with density, i.e., the peak positions and

overall wavelength seem not to be affected by a large density.

The rdfs show very distinct structural signatures and can significantly differ between the various salts. Let us focus in the following on the cation-anion rdf as it turns out later that they dominate the specific trends in the osmotic pressure behavior. The Li-Cl and Na-I rdfs, for instance, feature a quite small contact peak (contact values of 3 to 6) while the second peak is larger or of comparable height. This is in stark contrast to the structural behavior of KCl and CsCl, where the first peak is significantly larger and the second peak is relatively small. A similar but weaker trend is observed for NaCl and KF. For a comparison, the height of the contact peak of the cation-anion rdfs vs. salt concentration is plotted in fig. 4.2 for all salts. Apart from LiCl and NaI, a strong concentration dependence for $\rho < 0.5$ M is observable due to electrostatic screening. An inversion in the order of peak heights for KCl and CsCl can be observed at around 0.3 M. At a moderate density of $\rho \simeq 1$ M the order of decreasing peak height is KCl>CsCl>NaCl>KF>LiCl>NaI. Furthermore, the results for K(II)Cl and K(II)Cl(II) force field parameters (also shown in fig. 4.2 for $\rho = 0$, 0.3, and 2 M) can significantly differ from the Dang KCl results featuring much smaller contact peaks. Note that the force field parameters for K and K(II) have different σ and ϵ values but are balanced such that the effective size of the ion is similar. The same effective size, however, does obviously not lead to the same electrolyte structure. Interestingly, although $K^+(II)$ features a larger dispersion attraction than K^+, contact ion pair formation is suppressed which is probably due to a stronger binding of the first hydration shell.

The above observations are interesting in the view of Collins' law of matching water affinities and the salt's respective probability to form direct or indirect ion pairs [16, 17]. The Li^+-Cl^- and Na^+-I^- pairs are relatively asymmetric in their size and water affinity behavior [12]. Indeed, we observe that they prefer not to form contact pairs, visible from the small first and large second peak in the rdf. The opposite behavior is observed for the more symmetric salts KCl and CsCl. To quantify this, we estimate the ratio between the mean counterion densities in the second (one-solvent-molecule separated) and first solvation shell, that is

$$x(\rho) = \frac{(r_1^3 - r_0^3) \int_{r_1}^{r_2} g_{ij}(r;\rho) r^2 \, \mathrm{d}r}{(r_2^3 - r_1^3) \int_{r_0}^{r_1} g_{ij}(r;\rho) r^2 \, \mathrm{d}r}. \tag{4.1}$$

The integration boundaries r_k, with $k = 1, 2$, are the location of the first two minima in the cation-anion rdf, respectively, and r_0 is the distance at which the rdf vanishes to zero. Note that for uncorrelated systems, or if the mean number densities of particles in the first and second solvation shells are the same, the definition above leads to $x = 1$. The values of the distances r_k and results for $x(\rho)$ are summarized in tab. 4.1 on page 39 for two different concentrations, $\rho = 0$ and 1 M. The 1st and 2nd solvation shell widths lie between $r_1 - r_0 \simeq 0.09$ nm (KF) and $\simeq 0.15$ nm (CsCl), and $r_2 - r_1 \simeq 0.23$ nm (LiCl) and $\simeq 0.25$ nm (KF), respectively. The calculated values of $x(\rho)$ clearly distinguish between contact and solvent-separated ion pairs: for NaI and LiCl the counterion density in the second solvation shell can be 2 to 5 times higher than in the first solvation shell, respectively. In contrast, for KCl and CsCl the average counterion density in the first
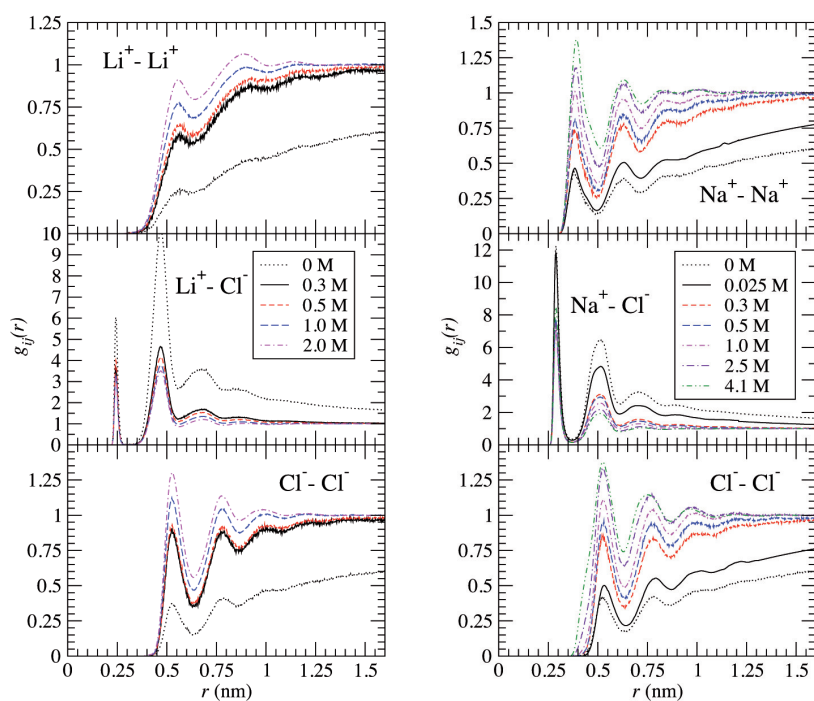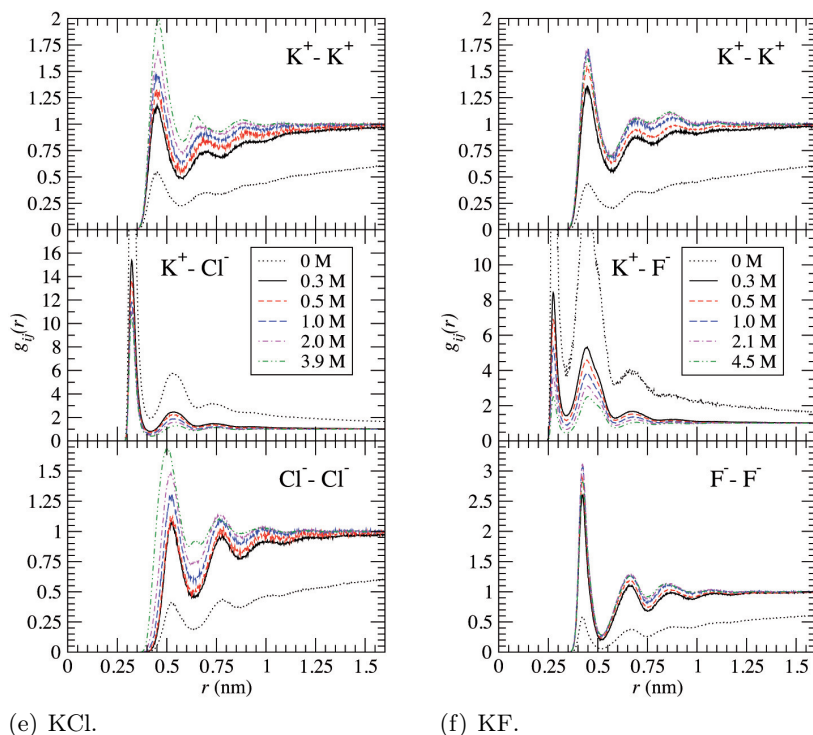
(a) LiCl.

(b) NaCl.
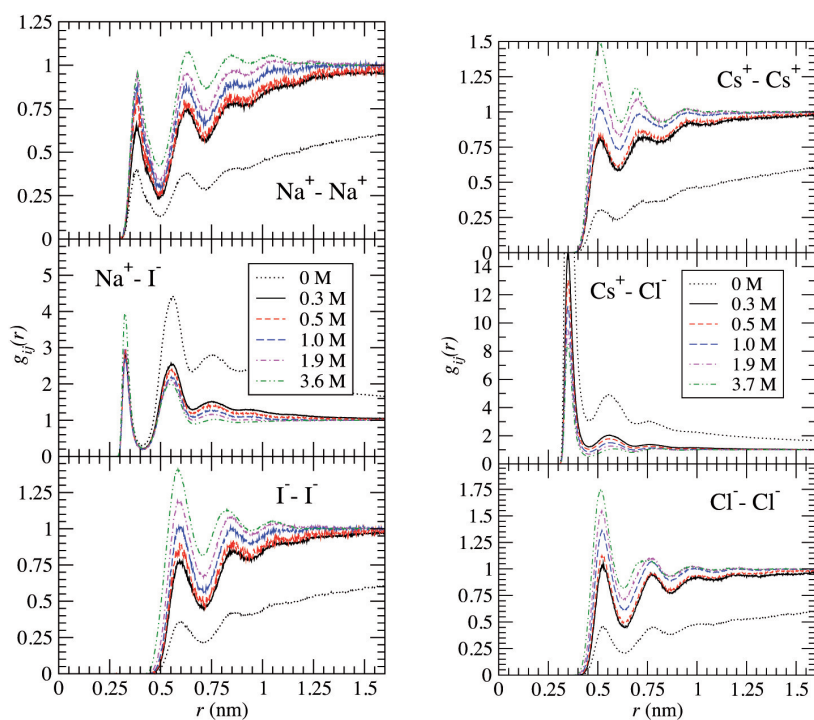
(c) NaI.

(d) CsCl.

Figure 4.1.: *Continued on next page.*

(e) KCl.   (f) KF.

Figure 4.1.: *MD results for the radial distribution functions for different monovalent electrolytes at different salt concentrations. Note that also the zero-density limit ($\rho \to 0$) is shown. Concentration values are rounded to the first digit after the comma.*

solvation shell almost doubles the one in the second solvation shell. For NaCl and KF, x is closer to unity. That is unexpected for KF because it is a rather asymmetric salt [16, 17]. The value for K(II)Cl and K(II)Cl(II) can qualitatively deviate from KCl, demonstrating a strong sensitivity of contact ion formation to the particular force field, a fact noticed previously in literature on ion-ion pmf modeling [116]. We conclude that Collin's law of matching water affinities is partly supported by our simple structural analysis, while the contact probability shows a strong force field sensitivity. Thus, a likely reason for the unexpected 'symmetric' behavior of KF may just be a bad choice of LJ parameters.

4.1.2. Ion-specific short-ranged pmfs

The intricate structural behavior of electrolytes is solvent-induced and stems from different hydration properties of the individual ions. As we have demonstrated in the previous chapter, by subtracting the Debye-Hückel interaction we can obtain an unobstructed view on the short-ranged pair potential $V_{ij}^{sr}(r)$ or structure.

An illustrating and representative example of the procedure is shown in fig. 4.3 on page 41 where we plot $\ln[w_{ij}(r)r]$ of eq. (3.20) for Na$^+$ and Cl$^-$ at salt densities $\rho = 0.025$, 0.2, 0.3, 0.5 M. As anticipated, we observe that for $r \gtrsim 2r_{sol} = 1.2$ nm the short-
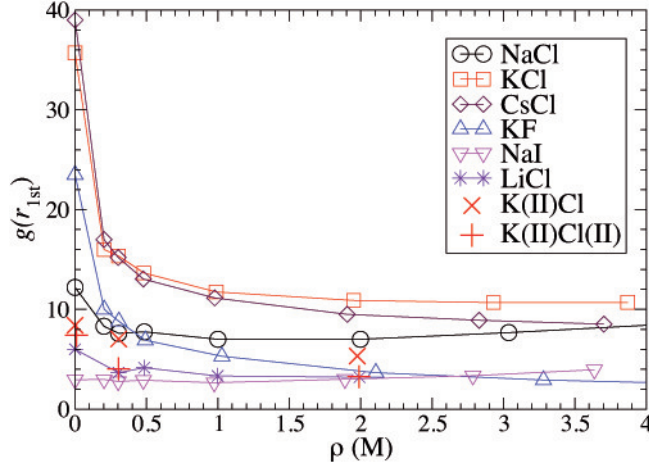
Figure 4.2.: *Height of the first peak (located at $r = r_{1st}$) of the cation-anion $g_{ij}(r)$ for the considered salts vs. concentration ρ.*

Table 4.1.: *The ratio $x(\rho)$ between the mean counterion densities in the second (one-solvent-molecule separated) and first solvation shells of the coion for $\rho = 0$ and 1 M. The mean densities are obtained by integration over the cation-anion rdfs defined in (4.1) using the integration boundaries r_k, $k = 0, 1, 2$.*

Ion pair	r_0/nm	r_1/nm	r_2/nm	$x(\rho = 0\ \text{M})$	$x(\rho = 1\ \text{M})$
LiCl	0.22	0.33	0.56	5.11	3.50
NaCl	0.26	0.37	0.61	1.36	1.03
KCl	0.29	0.42	0.66	0.63	0.63
CsCl	0.31	0.46	0.69	0.62	0.66
KF	0.25	0.34	0.59	0.95	1.13
NaI	0.29	0.41	0.66	2.15	1.68
K(II)Cl	0.29	0.40	0.64	1.32	0.94
K(II)Cl(II)	0.28	0.39	0.63	1.55	1.33

ranged structure has indeed decayed and the functional behavior is purely linear due to the screened Coulomb interactions. The inverse screening length from eq. (3.15) is $\kappa(\rho) = 0.54, 1.59, 1.98$ and 2.54 nm^{-1} for the above densities, and we find $\lambda_{ij}(\rho) = 0.96, 1.11, 1.17$ and 1.46 nm, respectively, with an $\lesssim 15\%$ error of the latter stemming from the standard deviation in the statistical fluctuations of $w_{ij}^{\text{DH}}(r)$. The normalization correction for the rdfs is $f(\rho) = 1.080, 1.056$ and 1.029 for the densities $\rho = 0.2, 0.3$, and 0.5 M. The potential for $\rho = 0.025$ M results from the free energy perturbation (FEP) calculation, described in the following, which comes with an arbitrary energy shift. The determination of $f(\rho)$ turns out to be quite accurate as the long-ranged linear decay in eq. (3.20) is very sensitive to its value. The resulting short-ranged parts of the pair potential $V_{ij}^{\text{sr}}(r)$ are plotted in the inset of fig. 4.3. The low density results agree with each other within a couple of percent. We have also attempted to evaluate $V_{ij}^{sr}(r)$ for densities 0.75 and 1 M but we could not reproduce the linear behavior for any value of

$f(\rho)$; we suspect that, due to the very small screening length ($\simeq 0.26$ nm for 1 M), the statistical sampling becomes too weak for a reasonable evaluation. The conformity of the derived short-ranged potentials demonstrates that a), the above procedure works fine for the calculation of accurate pair potentials, and b), that the short-ranged structure remains indeed quite undisturbed and density independent for $\rho \lesssim 0.5$ M.

For the smallest ion concentration possible $\rho = 0.025$ M, namely, a single pair of ions in the simulation box, we employ a simple thermodynamic integration (TI), also called FEP, procedure: a distance constraint is added between the two ions making use of the Lincs alorithm [169]. We set the highest order in the expansion of the constraint matrix to 4 and the number of correction iterations in the final step to 1. Two different distances $r_1 = 0.25$ nm and $r_2 = 2$ nm between the constrained ions are interpolated linearly making use of a coupling parameter $0 \leq \lambda \leq 1$. For each λ, a simulation of 500 ps up to distances $r_2 = 1.0$ nm and of 2 ns for distances $r > 1$ nm has been performed in order to obtain good statistical precision. Further on, the λ-spacing was set to 0.002 nm for short distances up to 0.4 nm, to 0.005 nm for intermediate distances (0.4-1.0 nm), and to 0.01 nm for distances greater than 1 nm. The total force on the two ions (the derivative of the total Hamiltonian with respect to λ) is ensemble-averaged for each value of λ. The integrated mean force, i.e., the pmf, obtained with this procedure has to be corrected for the entropic contribution, stemming from distance-constraining the ions [28, 141] according to $w_{ij}(r; \rho) = w_{ij}^{\mathrm{TI}}(r; \rho) - (D - 1)k_{\mathrm{B}}T \ln(r)$, where $D = 3$ is the dimension of the constraint. We carefully checked for selected salts at $\rho \simeq 0.3$ and 0.5 M that TI and the standard $g_{ij}(r; \rho)$ calculations yield the same result.

The $V_{ij}^{\mathrm{sr}}(r)$ for all ion combinations are shown in fig. 4.4(a) on page 42 revealing a couple of interesting features: first, comparing all cation-cation potentials, the Na$^+$ pair shows the strongest oscillations. We explain this by sodium's high water binding affinity and tightly bound hydration shells which give rise to energetic barriers whenever two Na$^+$ approach each other closely by a rare fluctuation. The Cs$^+$ pair in contrast hardly shows barriers due to weakly bound water, and the interaction is smooth and soft-sphere like. For Li$^+$ water binding is stronger than for Na$^+$ as can be observed by a higher LiO rdf contact peak (not shown), but the potential looks smooth and similar to the Cs$^+$ case. The reason is that the strong water binding of Li$^+$ leads to a huge energy barrier for close distances, so that the Li$^+$-Li$^+$ contact is never sampled. Turning to the anion-anion potentials, this strong hydration does not happen for the small fluoride pairs where contact configurations are possible and the structure is highly oscillatory. The latter smoothens for Cl$^-$. The large I$^-$ exhibits a rather structureless, soft-sphere like potential.

Let us now turn to the cation-anion pairs. In line with the rdf interpretation above that KCl and CsCl preferably form contact ion pairs, we observe that the first (contact) minimum in the potential is the global minimum of $V_{ij}^{\mathrm{sr}}(r)$. Adding the attractive Coulomb potential thus clearly drives the ions into a contact configuration. For the other salts, the *second* minimum at the solvent-separated configuration is the global minimum. Especially the asymmetric salts LiCl and NaI feature a $1 - 2$ k$_{\mathrm{B}}T$ deeper second minimum compared to the contact minimum. This big difference cannot be balanced by
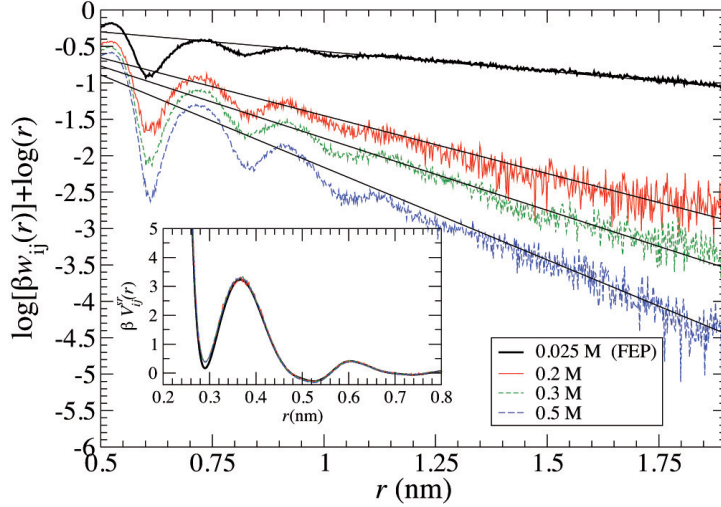
Figure 4.3.: *The effective potential $w_{ij}(r)$ between Na^+ and Cl^- plotted according to eq. (3.20) for different salt concentrations (see legend). From fitting a linear function to it with a slope given by the inverse decay length $\kappa(\rho)$ (solid lines), the prefactor in the DH expression (3.14) can be obtained. Subtracting the DH expression from $\beta w_{ij}(r)$ yields the short-ranged pair potential βV_{ij}^{sr} (inset) which appears to be independent of density within the considered density range.*

the electrostatic attraction as we deduct from the inversion of the infinite dilution rdf (not shown) and thus promotes solvent-separated configurations. A rather odd case is displayed by KF: although water binding is strong for F^-, the short-ranged potential exhibits only weak oscillations and a quite broad second minimum pointing to an unusual water configuration around a KF pair at a solvent-separated configuration.

A comparison between the $V_{ij}^{sr}(r)$ for the different KCl force fields is plotted in fig. 4.4(b) on the following page. Although the position of the first minimum is very similar for all combinations (within 3%), pointing to the same effective size, the depth of the potential minimum can vary significantly between 1 and 3 k_BT. This obviously tunes the height of the contact peak, which is shown for 0.3 M in the inset to fig. 4.4(b). The contact peak height of K(II)Cl is smaller than that of KCl, probably due to a tighter bound first hydration shell. The latter leads to a larger desolvation energy barrier at $r \simeq 0.4$ nm in $V_{ij}^{sr}(r)$ in fig. 4.4(b). We support earlier notes [116] that by changing the individual ion parameters slightly, the solvent-induced pair structure can be considerably affected.

Another instructive way of characterizing a pair potential in a more comprehensive way is to calculate its second virial coefficient by integrating over the Mayer function [40], viz.

$$B_2^{sr} = -2\pi \int_0^\infty \left(\exp[-\beta V^{sr}(r)] - 1\right) r^2 \mathrm{d}r. \qquad (4.2)$$

Note that $B_2^{sr} > 0$ for an overall repulsive interaction (yielding a positive contribution to the osmotic pressure), and $B_2^{sr} < 0$ for an overall attractive interaction (yielding a negative contribution to the osmotic pressure). The values for the individual $V_{ij}^{sr}(r)$ are
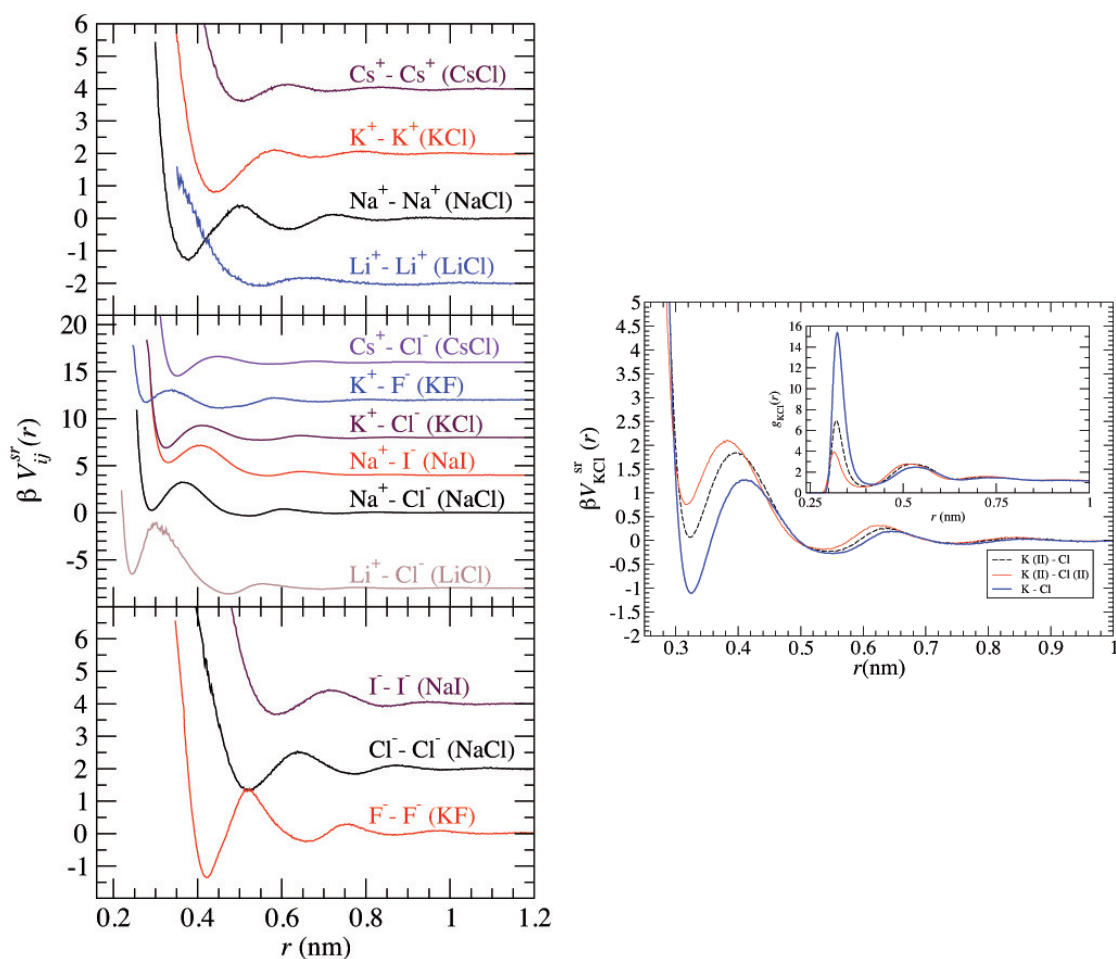
(a) Potentials for all studied ions. The curves are shifted by a constant energy for better comparison.

(b) K-Cl potentials and rdf at $\rho = 0.3$ M (inset) for KCl, K(II)Cl, and K(II)Cl(II).

Figure 4.4.: *Short-ranged pair potential $V_{ij}^{sr}(r;\rho)$ for the simulated ion pairs vs. radial ion-ion distance r.*

Table 4.2.: *Second virial coefficient B_2^{sr} for cation-cation $(++)$, cation-anion $(+-)$, and anion-anion $(--)$ pairs defined by eq. (4.2) using their short-ranged pair potential only. The unit is nm^3. The $\sum_{i,j}$-column is the sum of all contributions with $i, j = +, -$ (counting the cation-anion contribution twice).*

Ion pair	$B_2^{sr}(++)$	$B_2^{sr}(+-)$	$B_2^{sr}(--)$	$\sum_{i,j}$
LiCl	0.18	0.14	0.19	0.64
NaCl	-0.13	0.21	0.19	0.48
KCl	-0.14	0.06	0.19	0.17
CsCl	0.11	0.01	0.19	0.28
KF	-0.14	-0.08	-0.05	-0.33
NaI	-0.13	0.25	0.36	0.73
K(II)Cl	-0.16	0.29	0.19	0.61
K(II)Cl(II)	-0.16	0.14	0.23	0.35

summarized in tab. 4.2.

The cation-cation pairs of Na^+ and K^+ are overall attractive in this short-ranged picture, probably due to their smaller size and stronger oscillations with pronounced minima when compared to Cs^+ and Li^+ pairs which exhibit a repulsive short-ranged potential. Li^+ shows the strongest repulsion as its effective size is large due to its tight, covering hydration shell. Cs^+ features a comparable size but a deeper first minimum, so that the B_2^{sr} of the Cs^+-Cs^+ potential is somewhat lower. A monotonic trend can be observed for the investigated anion-anion pairs where the large I^- pair has a more repulsive potential than that of Cl^- or F^-. In contrast to lithium, the small fluoride pair shows the weakest repulsion from the anion pairs, a fact that has been controversially discussed in literature before [32, 170–172]. The cation-anion $V_{ij}^{sr}(r)$ are repulsive for the NaI, NaCl, and LiCl pairs, weaker repulsive for the KCl pair, and neutral for CsCl. Surprisingly, the KF pair features an attractive short-ranged pair potential, probably due to the unusually broad, second minimum in $V_{ij}^{sr}(r)$ [amplified by the r^2-term in (4.2)]. We will see later that the B_2^{sr}, especially the one of the cation-anion pairs, will be strongly related to the low-density osmotic pressure behavior of the salts.

4.1.3. BH diameters

Our short-ranged ion-ion pmfs can be integrated and mapped onto a HS system along the lines of section 3.5. Fig. 4.5 shows both $f_{ij}(r)$ and σ_{ij} for all ion-ion combinations of the NaCl salt. The σ_{ij} are not to be confused with the LJ parameters of tab. 2.1. The Mayer-functions exhibit oscillations and can become positive due to attractive regions in the ion-ion short-range pmfs. This attraction can lead to much smaller than expected effective diameters. A typical example is Na^+-Na^+, which has a BH diameter of $\sigma_{++} = 0.22$ nm even though the ion-ion short-range potential $V_{++}^{sr}(r)$ already diverges to infinity at a distance $r \simeq 0.3$ nm.

The BH diameters σ_{ij} for all studied salts are summarized in tab. 4.3 on the following page. As ionic interactions and pairing affinities are governed by hydration effects we
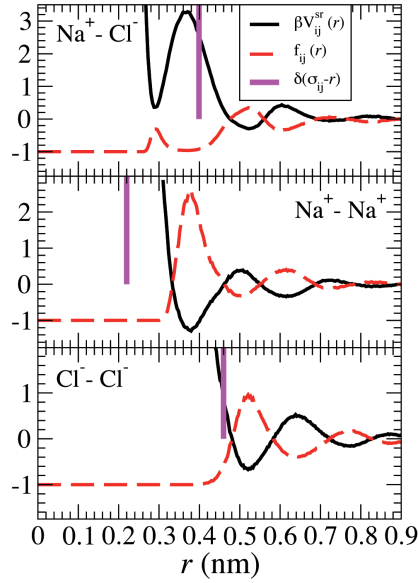
Figure 4.5.: *Mapping of ion-ion short-range pair potentials onto hard-sphere interactions in the case of sodium chloride (NaCl). Shown is the short-range pair potential V_{ij}^{sr} (black full), its Mayer-function $f_{ij}(r) = \left[\exp\left(-\beta V_{ij}^{\mathrm{sr}}(r)\right) - 1\right]$ (red dashed) and the effective BH hard-sphere diameter σ_{ij} in the form of a delta function (magenta).*

Table 4.3.: *Barker-Henderson diameters σ_{ij} and nonadditivity Δ_{+-} defined by $\sigma_{+-} = \frac{1}{2}\left(\sigma_{++} + \sigma_{--}\right) \times (1 + \Delta_{+-})$ for all salts studied.*

Salt	σ_{++} (nm)	σ_{+-} (nm)	σ_{--} (nm)	Δ_{+-}
LiCl	0.45	0.38	0.46	-0.16
NaCl	0.22	0.40	0.46	0.18
KCl	0.19	0.30	0.46	-0.08
CsCl	0.41	0.22	0.46	-0.49
NaI	0.22	0.47	0.47	0.36

ascertain that it is not possible to determine the effective diameters σ_{ij} by looking at vacuum van der Waals radii only. Another striking example is the Li$^+$-Li$^+$ pair, which has the smallest van der Waals radius but exhibits the largest effective BH diameter of all cations studied. A more detailed inspection of the values σ_{ij} in tab. 4.3 shows that electrolytes resemble size-asymmetric and nonadditive hard-sphere mixtures, viz.

The CsCl salt, for instance, has a large negative nonadditivity $\Delta_{+-} = -0.49$. CsCl will therefore show a tendency for mixing. In strong contrast, we expect NaI, having a large positive nonadditivity of $\Delta_{+-} = 0.36$, to be strongly influenced by excluded-volume correlations and inclined to phase-separate. Indeed, at high concentrations, we will see that the NaI salt in confinement will lead to a highly asymmetric system and strong layering. A positive nonadditivity in general competes with electrostatics, which always favors mixing of cations and anions.

4.2. Dielectric constant

We measure $\epsilon(\rho)$ in our bulk MD simulations by calculating the dipole fluctuations of the water molecules using eq. (3.24). In the salt-free case we calculate a dielectric constant of $\epsilon(0) = 72 \pm 1$ for SPC/E water, consistent with the literature value [140], and smaller than $\epsilon(0) = 78.4$ for real water at $T = 298$ K. The MD results for the water dielectric constant $\epsilon(\rho)$ in dependence of salt type and concentration are presented in fig. 4.6 on the next page. All investigated salts decrease the dielectric screening of water, while in particular for larger salt concentrations $\rho \gtrsim 0.5$ M, the decrease quantitatively depends on salt type. Our results agree with other MD studies of NaCl and KCl using the same force field [173], or NaCl using the KBFF ion parameters [27, 28]. We find that for densities $\rho \lesssim 2$ M the functional form of $\epsilon(\rho)$ can be fitted reasonably well with the expression $\epsilon(\rho) = \epsilon(0)/[1 + A(\rho/M)]$, with $A = 0.31$, 0.27, 0.24, and 0.23, for the chloride salts LiCl, NaCl, KCl, and CsCl, respectively, and $A = 0.34$ and 0.31 for NaI and KF.

The results for the relative decrease of $\epsilon(\rho)$ with salt type and concentration are in very good agreement with experimental measurements [174–180] for concentrations up to $\rho \simeq 1$ M. The experimental results are plotted in the bottom part of fig. 4.6 for a direct comparison. For larger concentrations the situation worsens and the simulation overestimates the relative decrease of $\epsilon(\rho)$ by up to 15%. The trends with changing ion size, however, are reproduced for all salts by the MD results within the statistical error: the larger the cation ($Li^+ < Na^+ < K^+ < Cs^+$), the smaller the decrease of $\epsilon(\rho)$. Interestingly, for anions the trend is reversed, i.e., by going from NaCl to NaI, or from KF to KCl the relative decrease of $\epsilon(\rho)$ enhances. Apparently, although water is more tightly bound for both, smaller anions and cations, dipolar fluctuations change in a qualitatively different way: they seem not necessarily be related to ionic solvation free energies (or contact peak heights in the ion-water rdf), which monotonically follow changes in ionic size [14].

4.3. Osmotic pressure

We compute the osmotic coefficient with the procedure shown before in fig. 3.2 on page 23. In fig. 4.7 on page 48 we plot the comparison between the osmotic coefficients from the compressibility route $\phi_\chi(\rho)$ and experimental results (at $T = 298$ K) for all considered salts and densities $\rho < 5$ m. Note that we use the unit molality (m=mol/kg) instead of molarity (M=mol/l) for the comparison. The chloride salts LiCl, NaCl, CsCl with the exception of KCl match the experimental values within the theoretical error bar for densities $\rho \lesssim 2$ m, indicating that the Dang-SPC/E force field combination performs well for these salts. The osmotic coefficient for KCl deviates for $\rho \gtrsim 1$ m not only quantitatively but exhibits a qualitative difference to the experimentally measured $Li^+ > Na^+ > K^+ > Cs^+$ order in the decrease of ϕ, as its $\phi_\chi(\rho)$ becomes smaller than the one of CsCl. This is somewhat surprising, as the experimentally measured order is also obeyed by their (van der Waals) size distribution, in reality *and* in the employed MD force field. The largest deviations are observed for the NaI and KF salts. For NaI, the MD simulation
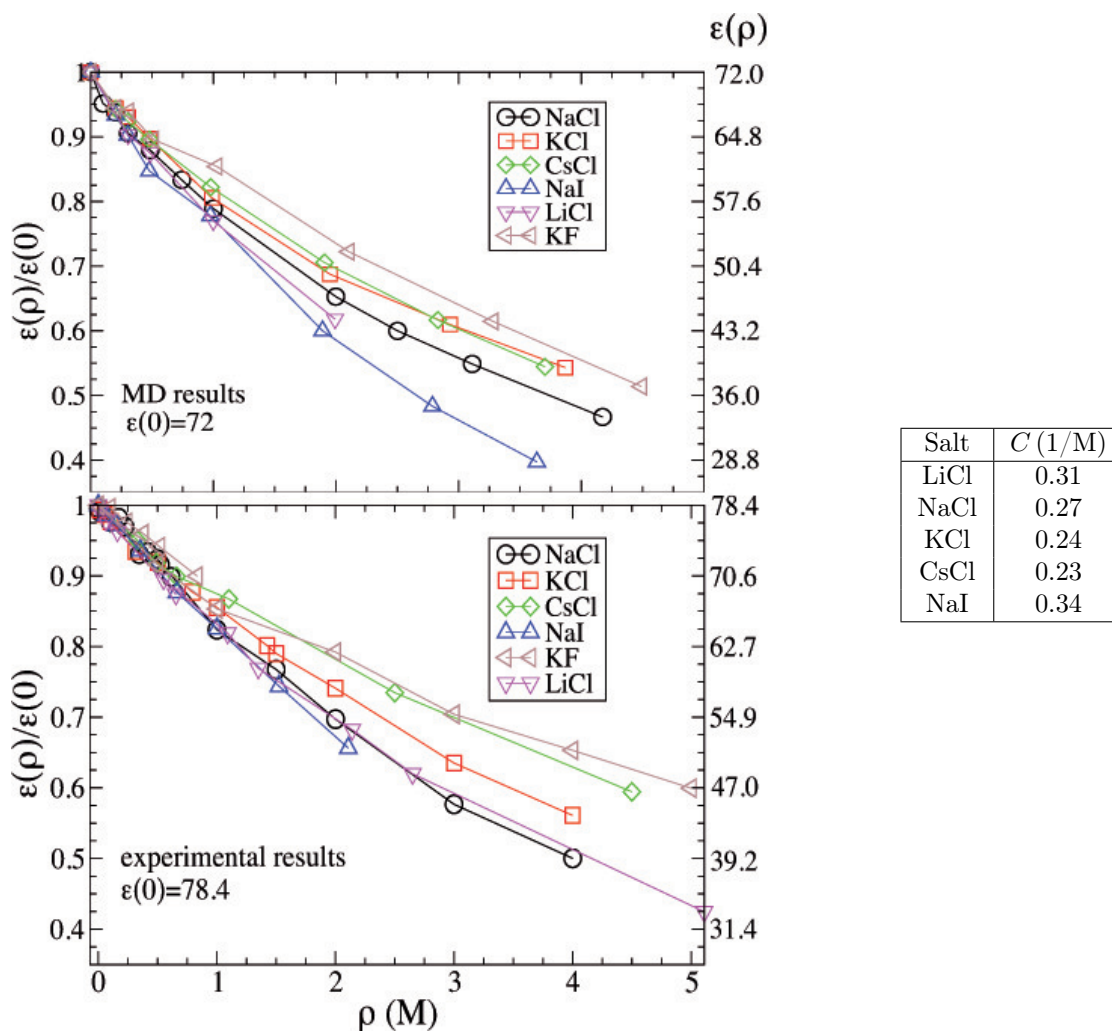
Figure 4.6.: *Water dielectric constant $\epsilon(\rho)$ vs. salt concentration ρ from MD simulations (top figure) and experiments [174–180] (bottom figure). Data points are depicted by symbols while lines are guides to the eye. The magnitude of the statistical error is smaller than the symbol size. The labels at the right vertical axes show the absolute $\epsilon(\rho)$ values. The salt-specific dielectric constant of the MD simulations can be calculated with $\epsilon(\rho) = \frac{\epsilon(0)}{[1+(C\times\rho)]}$ with $\epsilon(0)$ being the dielectric constant at infinite dilution and ρ being the concentration in mol/l (M). The ion-specific constants C are displayed in the table on the right.*

shows a strongly increasing osmotic coefficient larger than $\phi = 1$ for $\rho \gtrsim 1$ m in line with the experiments but overestimates the deviation from $\phi = 1$ by more than a factor of two. The osmotic coefficient of KF from MD is entirely wrong and is $\phi_\chi < 1$ for all densities while the experiments show a change of sign at $\rho \simeq 2.3$ m.

A comparison between the osmotic coefficients from the compressibility route and the virial route, ϕ_χ vs. ϕ_v, is presented in fig. 4.8 on page 49 for all six salts. Without the many-body correction by $\epsilon(\rho)$, the virial route prediction deviates considerably from the compressibility route starting from densities $\rho \simeq 0.5$ m, as exemplified for NaCl in fig. 4.8. This finding is in accord with the study of Hess *et al.* [27] who used the same correction in implicit water computer simulations. We observe the same qualitative behavior for the other salts, too (not shown). With the correction included, a reasonable agreement of the virial route with the compressibility route can be achieved for concentrations $\rho \lesssim 2$ m for all chloride salts within the statistical error. Deviations are found already for smaller densities ($\rho \simeq 1$ m) for KF. However, we hereby corroborate and generalize the validity of the $\epsilon(\rho)$ correction found by Hess *et al.* for NaCl to other salts in the molar concentration range.

In fig. 4.8(a), we also plot selected results for the K(II)Cl and K(II)Cl(II) force fields. For $\rho = 0.3$ m, K(II)Cl(II) agrees well with experiments (cf. fig. 4.7) while K(II)Cl overestimates the osmotic coefficient. Both parameter sets predict a significantly too high ϕ at a density of $\rho = 2.1$ m with $\phi = 1.05$ and 1.4 (not on scale) for K(II)Cl(II) and K(II)Cl, respectively, and out of the experimental Li$^+$ > Na$^+$ > K$^+$ > Cs$^+$ order. From our analysis so far, it emerges that the osmotic coefficient (and structure) of electrolyte solutions in MD simulations is very sensitive to slight changes in the force field as observed before in HNC and MC calculations [28, 31, 32]. Note that none of the tested combinations for KCl can describe the experimental osmotic pressure at $\rho \simeq 2$ M within our error bars.

Results for the partial corrections to the osmotic coefficient $\Delta\phi^{sr} = \sum_{i,j} \Delta\phi_{ij}^{sr}$ and $\Delta\phi^{DH} = \sum_{i,j} \Delta\phi_{ij}^{DH}$, are shown in fig. 4.9 on page 51. For all salts we observe that the sum of long-ranged (electrostatic) contributions $\Delta\phi^{DH}$ is strongly negative, i.e., reducing the total osmotic coefficient as could have been expected from DH theory only, and hardly depends on salt type. The DH limiting law (3.43) nevertheless overestimates this contribution by almost a factor of two because it does not consider the finite size of the ions. Indeed, one can find easily that an analogous virial integration over DH forms [149] with a lower distance cut-off a leads to the expression $\phi_{DH} = 1 - \kappa^3/[48\pi\rho(1+\kappa a)]$. Using $a \simeq 0.3$ nm, we find that this size-corrected DH limiting law describes the long-ranged electrostatic data within the statistical error. Further inspection of fig. 4.9 shows that the specificity is provided by the short-ranged contributions $\Delta\phi^{sr}$ and is dominated by the cation-anion part $\Delta\phi_{+-}^{sr}$ for densities $\rho \lesssim 0.5$ M, for NaCl and KCl up to 1 M. In this range, the anion-anion and cation-cation contributions are small and/or cancel each other while the DH contribution is counterbalanced by the cation-anion short-ranged contribution only.

An eye-catching behavior is displayed by KF: from fig. 4.9(b) on page 51 we observe that it is the only salt whose cation-anion short-ranged contribution acts not repulsive
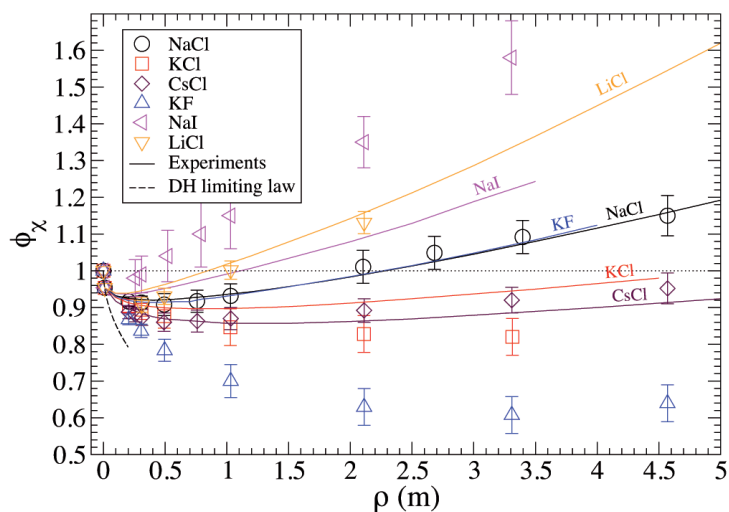
Figure 4.7.: *The osmotic coefficient ϕ_χ vs. salt concentration ρ from the compressibility route [eqs. (3.40) and (3.41)] compared to experimental values. The DH limiting law (3.43) is also shown (black dashed line).*

to the osmotic pressure so that the resulting $\Delta\phi$ is dominated by the DH part only. By comparing this behavior to the second virial coefficient B_2^{sr} of the short-ranged potentials (cf. tab. 4.2 on page 43), we rationalize an intimate connection as only $B_2^{sr} < 0$ for the K^+-F^- pair. Further inspection reveals that a general trend can be observed for all investigated salts. At moderate densities $\rho \gtrsim 1$ m, the magnitude of ϕ decreases in the order NaI > LiCl > NaCl > CsCl > KCl > KF: the same order is found in the sum of the second virial coefficients of the short-ranged pair potentials, see the last column in tab. 4.2. Thus, the strong osmotic repulsion for LiCl and NaI can be traced back to the large Li^+ (dressed by a water shell) and I^--ions yielding large positive virial coefficients. For small densities $\rho = 0.5$ m, we find that the order in decreasing osmotic pressure is different and is NaI > NaCl > LiCl > KCl > CsCl > KF. As observed before, the low density behavior is dominated by the cation-anion short-ranged potential; again, the just mentioned series of salts agrees with the $B_2^{sr}(+-)$ of the cation-anion short-ranged pair potential only, see the second column of tab. 4.2. As an important conclusion, we emphasize that for $\rho \lesssim 0.5$, the *specific* behavior of ϕ is determined by the cation-anion $V_{ij}^{sr}(r)$ only and is strongly related to B_2 of the latter.

4.4. Shear viscosity

In order to get a more complete picture of the solvent properties we calculate bulk shear viscosities for NaCl, KCl, and NaI at moderate concentrations around $\simeq 3.5$ M. We use SPC/E water, but present also results for the rigid TIP3P water model. For the Green-Kubo method, we use MD simulations of a bulk electrolyte, where, after NPT-equilibration we proceed with an NVT-production run of 50 ns. In the case of the non-equilibrium method, the external acceleration profile of eq. (3.28) is applied to every

(a) NaCl, KCl, and CsCl   (b) KF, NaI, and LiCl
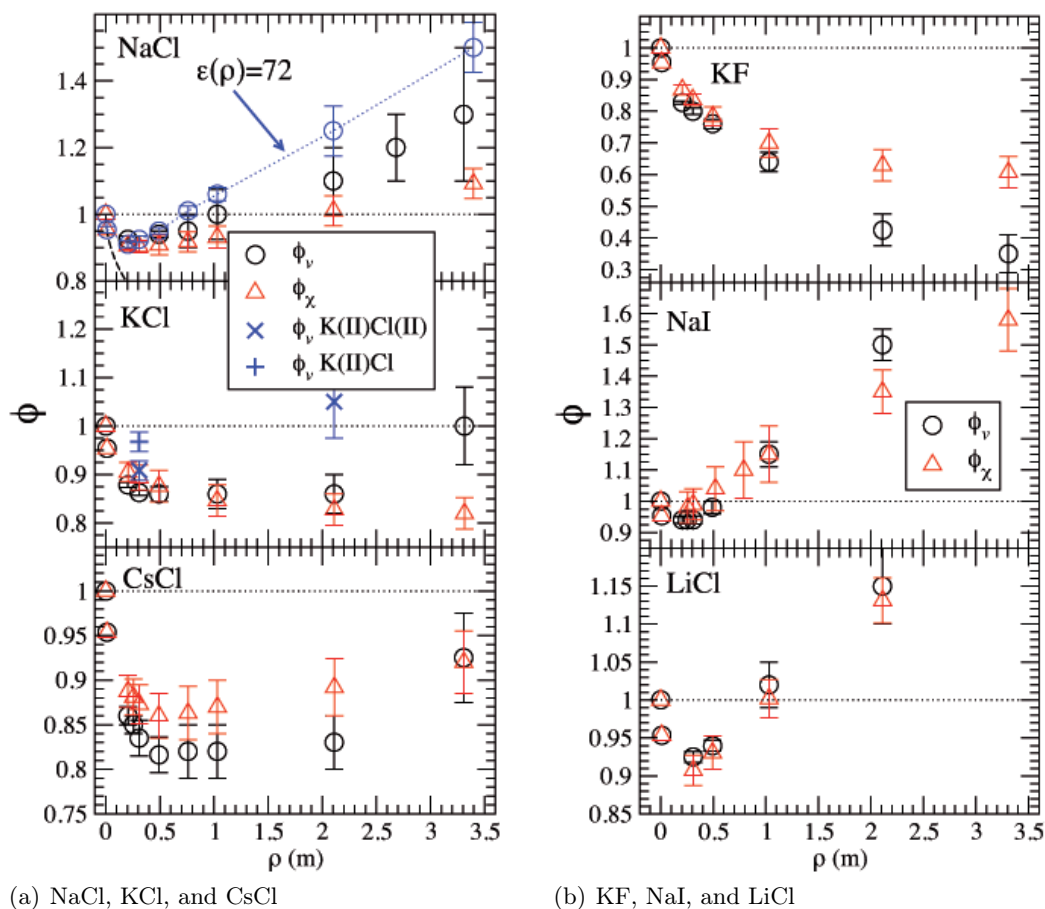
Figure 4.8.: *The osmotic coefficients ϕ_χ and ϕ_v from the compressibility and virial routes, respectively. The DH limiting law (3.43) is also shown in the NaCl plot (black dashed line).*

water molecule and salt ion in a bulk NVT-simulation.

With the GK formula we find values of $\eta_0 = 0.31 \pm 0.01 \; 10^{-3}$ kg/(m·s) for pure TIP3P water, corroborating with a previous study [181], and $\eta = 0.58$, 0.74, and 0.6 ± 0.01 10^{-3} kg/(m·s) for the KCl, NaCl, and NaI solutions at a concentration of 3.6 mol/l, respectively. For SPC/E water we find $\eta_0 = 0.68 \pm 0.01 \; 10^{-3}$ kg/(m·s) for pure water, again similar to earlier work [181], and $\eta = 1.34$, 1.41, and $1.37 \pm 0.01 \; 10^{-3}$ kg/(m·s) for the KCl, NaCl, and NaI solutions at a concentration of 3.6 mol/l, respectively. The non-equilibrium method yields the same results within a 5% error range. Compared to experimental values [2] the MD simulation considerably overemphasizes the increase of the viscosity at this elevated salt concentration for both water models; indeed, the viscosity was experimentally found to increase by only roughly 5% for KCl and 30-40 % for NaCl and NaI compared to pure water. This failure in describing the correct bulk viscosities of the electrolyte solutions must be attributed to inaccuracies in the force field.

4.5. Short summary

In this chapter we calculated as a first step the fluid structure of homogeneous aqueous electrolyte solutions for LiCl, NaCl, KCl, CsCl, KF, and NaI by using all-atom molecular dynamics (MD) simulations of the frequently employed Dang force field for ions [116–119] and SPC/E water [114]. We found that the short-ranged, water-mediated ion-ion structure remains ρ-independent for $\rho \lesssim 0.5$ M, which can be rationalized by the small packing fraction and overlap probabilities of the ion pairs in this density range. We utilized this fact to efficiently derive accurate ion potentials of mean force (pmfs) from non-vanishing densities ($\rho \simeq 0.3$ M) by subtracting the long-ranged, screened Coulomb part. Further on, simple integrals over the latter short-ranged pmfs yielded *effective* ion-ion Barker Henderson (BH) diameters. The osmotic coefficient ϕ_χ calculated from the exact *compressibility route* for the employed cation-Cl$^-$ force fields from Dang match experiments well for $\rho \lesssim 2$ M, whereas for NaI—while reproducing the 'hofmeister order'—the agreement is not quantitative. KF parameters failed. Comparison of ϕ_χ to ϕ_v from the *virial route*, which relies on the pair potential approximation, showed us that many-body effects become important for all salts above $\rho \simeq 0.5$ M but can be corrected using a ρ-dependent dielectric constant $\epsilon(\rho)$. The latter finding corroborates and generalizes previous studies on NaCl only [27, 28]. Additionally, the salt-type dependent $\epsilon(\rho)/\epsilon(0)$ data from our MD simulation agreed well with experiments. By analyzing the short- and long-ranged pair potential contributions to the virial, we found that for $\rho \lesssim 0.5$ M, the specific osmotic properties are determined by the short-ranged cation-anion pair potential only and are strongly related to the second virial coefficient of the latter. Simple structural properties such as contact pairing probabilities, however, have only weak relation to osmotic trends.

(a) NaCl, KCl, and CsCl.

(b) LiCl, KF, and NaI.
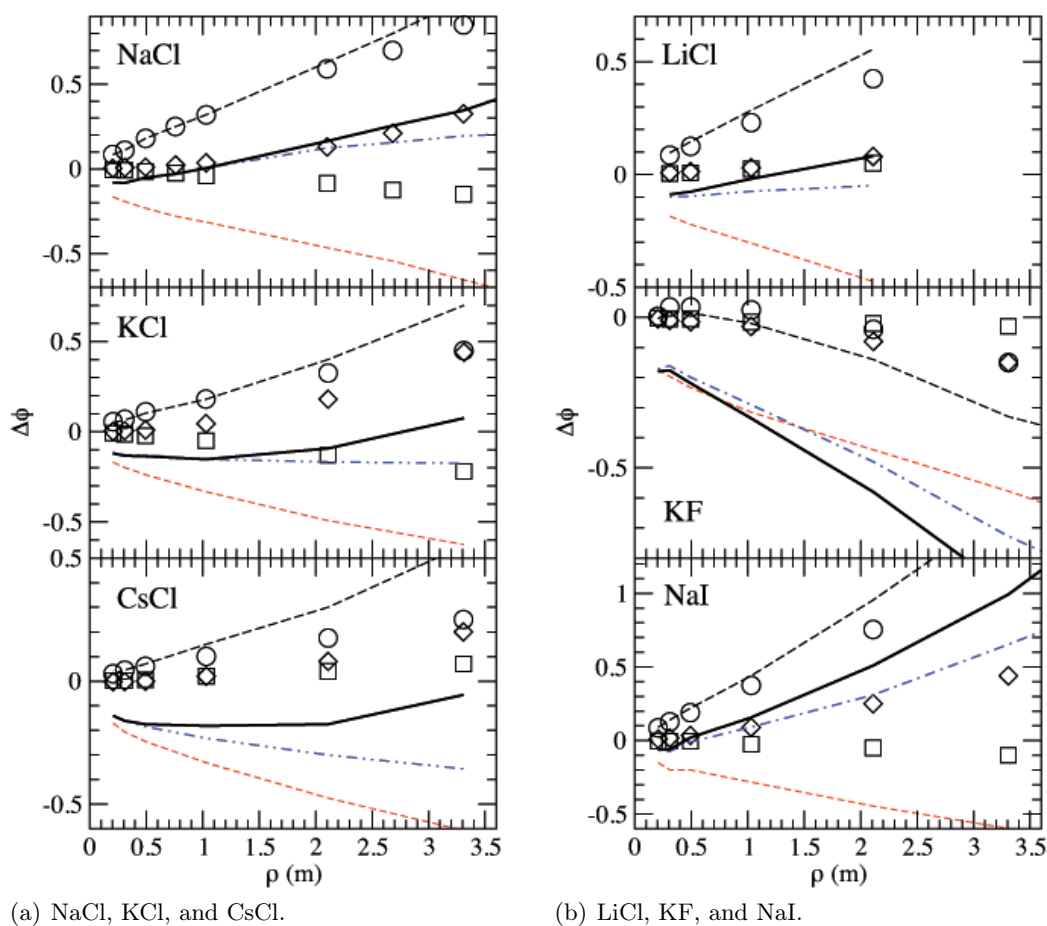
Figure 4.9.: *Individual contributions to the change $\Delta\phi$ in the osmotic coefficient $\phi = 1 + \Delta\phi$. The symbols are the contributions due to the short-ranged part of the pair potential from cation-anion (circles), cation-cation (squares), and anion-anion (diamond) pairs. The black long-dashed line corresponds to their sum, i.e., the total short ranged part, while the red, short-dashed line is the total contribution from the long-ranged part of the pair potential. The dot-dashed line is the sum of the total long-ranged part and the cation-anion short-ranged part only. The thick solid line is the total change $\Delta\phi$.*

Chapter 5

Ion-Specific Structure and Correlations in a Nanoconfinement

This chapter addresses the ion-specific structure of confined dense electrolytes. For this, we first compare the ionic structure of our DFT-PB approaches to MD and MC simulation results for all salts in a one-dimensional nanoconfinement. The latter consists of both charged and uncharged model hydrophobic surfaces with surface-to-surface distances on the order of $d \simeq 2$ nm. Effective salt concentrations are in the molar range. We then proceed by investigating excluded-volume correlations in case of the Donnan effect for NaI and LiCl. We then compute solvation forces for all salts for like-charged plates and compare them to the uncharged case. Finally, we inspect the charge distribution in the vicinity of a charged surface and will analyze whether ion-surface interactions or ion-ion excluded-volume correlations drive overcharging.

5.1. Structure at infinite dilution

In order to effectively coarse-grain our slab-water-salt system we extract two main terms from all-atom MD simulations at infinite dilution: ion-ion short range pmfs $V_{ij}^{\text{sr}}(r)$ or effective ion-ion BH diameters, and the (also short-ranged) ion-surface pmf $V_i^{\text{ext}}(r)$. The $V_{ij}^{\text{sr}}(r)$ have already been computed in the previous chapter and the relevant cation-anion pmfs are summarized in fig. 5.1 on the following page. We calculate the $V_i^{\text{ext}}(r)$ by umbrella sampling (methodological details are given in chapter 2). The resulting ion-wall pmfs are shown in fig. 5.1. We observe partial attraction for the large I^- and Cs^+ ions, while Na^+ and Cl^- are repelled from the surface, corroborating with earlier studies [57, 182]. A more astonishing feature is that the Li^+ cation, even though having a very small van der Waals radius (cf. tab. 2.1 on page 9), is attracted to the hydrophobic wall instead of favoring hydration in bulk water. This could be attributed to a force field problem but is presumably due to the tightly bound first solvation shell that is
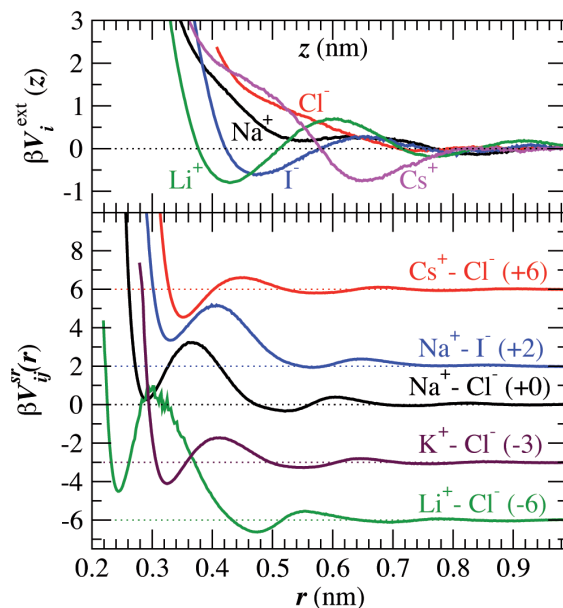
Figure 5.1.: *Effective ion-surface potentials $V_i^{ext}(z)$ (top) and the short-ranged part of the cation-anion pair potentials $V_{ij}^{sr}(r)$ (bottom). The latter curves are shifted vertically for a better view where the shifted x-axes are depicted as dotted lines. The potentials are obtained from explicit-water MD simulations described in chapter 4.*

not clearly distorted at the location of the minimum in the ion-wall pmf at a distance $z = 0.43$ nm from the surface. Similar trends have already been seen at the air-water [56] and a hydrophobic interface [183].

5.2. Electrolyte structure

5.2.1. MD and MC

Fig. 5.2 on page 56 displays a comparisons of MD- and MC-derived density profiles for LiCl, NaCl, CsCl and NaI for two different ion area densities. The MC profiles are shown using on one hand realistic, MD-derived dielectric constants, given in the caption of fig. 5.2, and on the other hand one corresponding to experimental pure bulk water. We observe in general good agreement between the results for MD and MC for an area density of $\tau \simeq 3$ nm^{-2}, even though the MC simulations with the realistic dielectric constant perform better. This trend substantiates even more for higher concentrations, i.e., larger dielectric deviation from bulk water. The special case of the NaCl salt at the higher effective concentration is due to fast crystallization and will be treated later in chapter 6. The MC simulations with MD-derived dielectric constants reproduce particularly well the ionic concentration at the walls and in the middle of the slab in the MD simulation. However, we note that the agreement of MC in comparison with MD is ion-specific. For LiCl, for example, MC is able to predict the MD profiles almost perfectly, whereas for

NaCl the cation density profile exhibits differences already at the lower concentration. This is due to multi-body and explicit-water effects that seem to play a more important role for Na^+, the effectively smallest cation in our study, than for Li^+, the effectively biggest. Nonetheless, we highlight that MC simulations with correctly chosen ion-ion and ion-wall interactions and a reasonable dielectric constant are able to reproduce the *electrolyte structure* in an explicit-water system in a slab-confinement fairly well. The importance of a properly chosen dielectric constant has been pointed out in literature so far only for bulk thermodynamic properties as the osmotic pressure [27, 28].

5.2.2. MC and DFT-PB

Fig. 5.3 on page 57 show a comparison of ion density profiles for MC, PB, PF and hard-sphere LDA approaches for two different area densities. We observe that PF and all local corrections to PB tend to level off regions of high and low ionic concentration within the slab. While in the case of NaCl the B3 and B2 LDA methods can describe well the ion-ion correlations seen in MC, they fail to reproduce the ion density profiles of a lower correlated system as CsCl ($\Delta_{ij} = -0.49 < 0$). Local theories in general perform badly for electrolytes with ions attracted to the interface as the lithium cation or the iodide anion (not shown). This is due to the indiscriminative energy penalty imposed on high salt concentrations. There are no systematic trends to validate any of the discussed local theories, on the contrary, in most cases the "unimproved" Poisson-Boltzmann theory seems to be better or equally well-suited for a wide range of concentrations and salts as CsCl or LiCl. For a further analysis we compute the pressure on one wall, defined as in eq. (3.73), for MC and the B3 LDA for all salts at the higher ion area density. In tab. 5.1 we see that the B3 method, even though performing better than PB, overestimates the pressure of MC always by 20 to 30 %, independently of the salt studied. Furthermore, none of the tested LDAs are able to compute stable ion density profiles for NaI. It was noted in literature before that local density approximations for hard-sphere ions lead to instabilities beyond certain ion sizes [184]. As a conclusion, we state that LDAs are neither able to predict electrolyte structure nor the correct pressure for inhomogeneous electrolytes in confinement.

In fig. 5.4(a) we show a comparison of the same MC ion density profiles with both the NPB-HS and NPB theories. We observe on one hand that NPB-HS and NPB perform quasi-identically; on the other hand, we observe that the nonlocal theories, even though neglecting electrostatic correlations, are able to reproduce the electrolyte structure of the MC simulations even at regimes of low dielectric constants fairly well with the exception of NaI. In addition, we compare in fig. 5.4(b) results for NPB-HS on an additive, i.e., $\Delta_{ij} = 0$ and therefore $\sigma_{+-} = \frac{1}{2}(\sigma_{++} + \sigma_{--})$, and nonadditive level, assessing the impact of Δ_{ij}. We see only a minor difference for the NaCl and LiCl salts, whereas for CsCl and NaI a difference and better performance of the nonadditive model is discernible. We quantify the latter by analyzing the relative error in pressure compared to MC in tab. 5.1 on page 59. LiCl and NaCl perform equally well on the additive and the nonadditive level. This is not surprising given their small nonadditivity, see tab. 4.3 on page 44. For CsCl and NaI, on the contrary, the nonadditive theory is evidently superior. For CsCl for
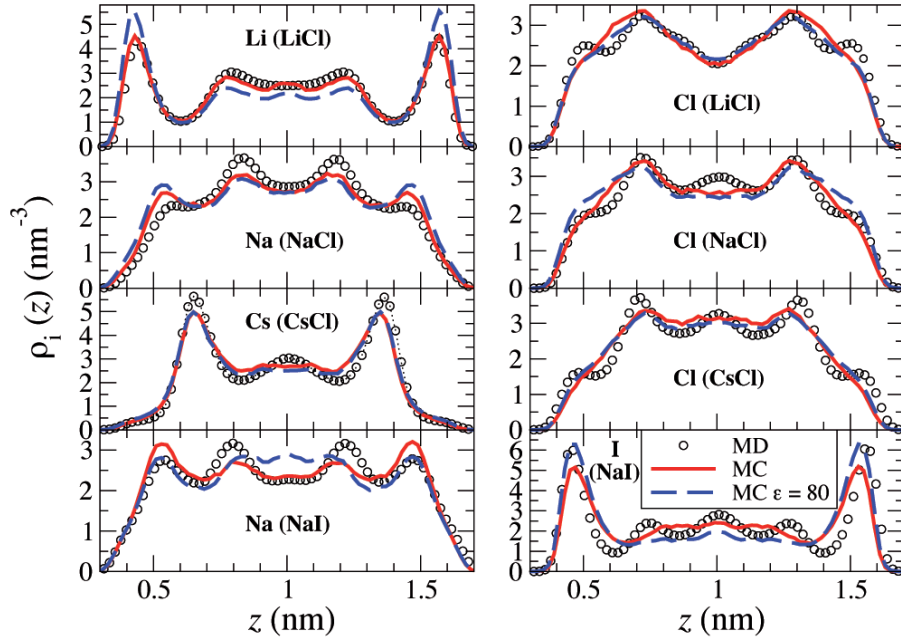
(a) Ion area density of $\tau \simeq 3$ nm^{-2}, effective ion concentration of $\bar{\rho} \simeq 2.5$ M and dielectric constants of $\epsilon = 33, 38, 47, 36$ for LiCl, NaCl, CsCl and NaI respectively.
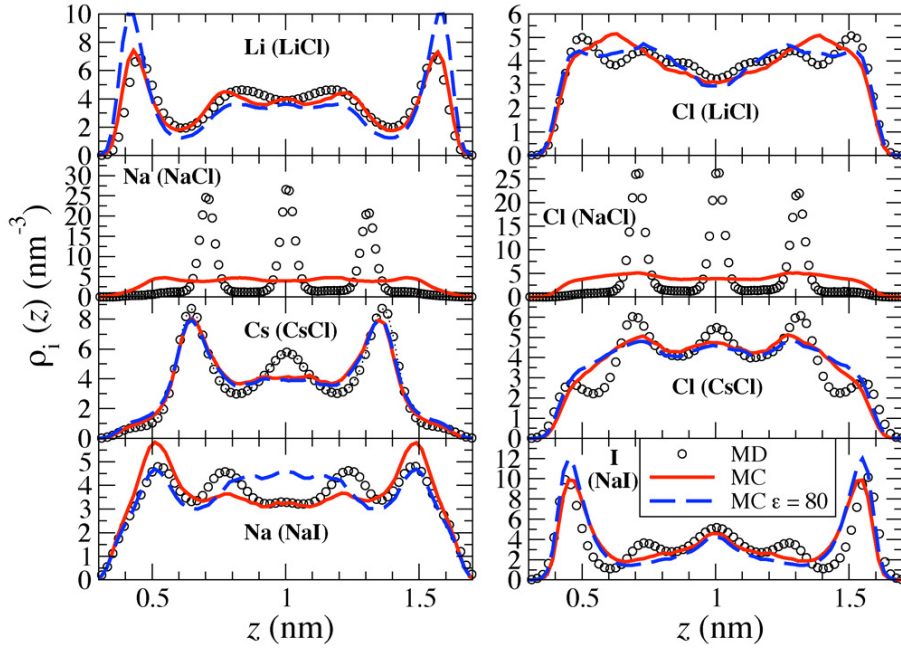
(b) Ion area density of $\tau \simeq 5$ nm^{-2} and $\epsilon = 21, 26, 41, 36$ for LiCl, NaCl, CsCl and NaI respectively

Figure 5.2.: *MD (circles) and MC derived ion density profiles in a $d = 2$ nm slab-confinement. Results for MC are shown for both realistic (MD derived) dielectric constants (red continuous line), and the dielectric constant of experimental pure bulk water $\epsilon = 80$ (blue dashed line).*
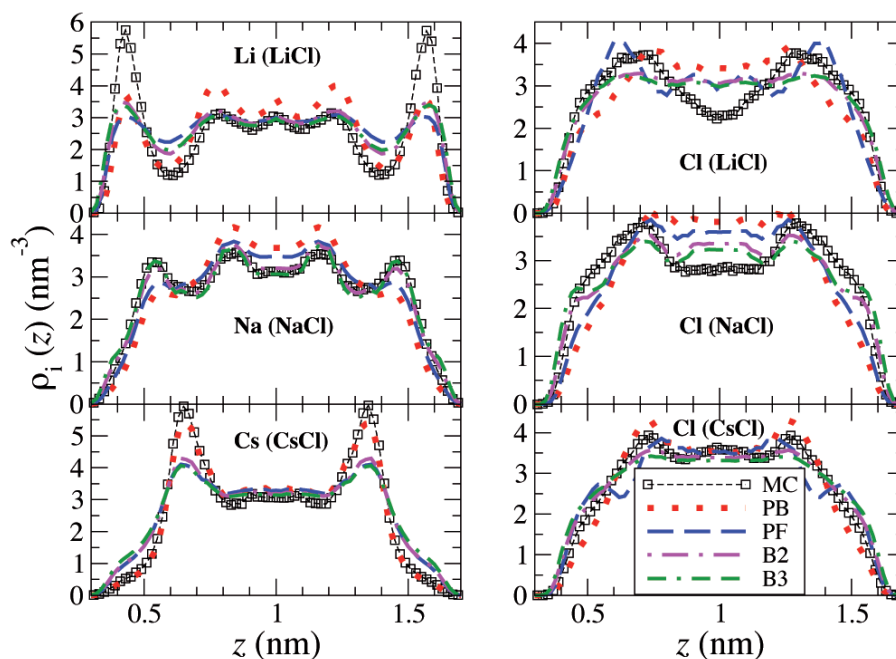
(a) Effective concentration of $\bar{\rho} \simeq 3$ M and ion area density of $\tau \simeq 3.6$ nm^{-2}
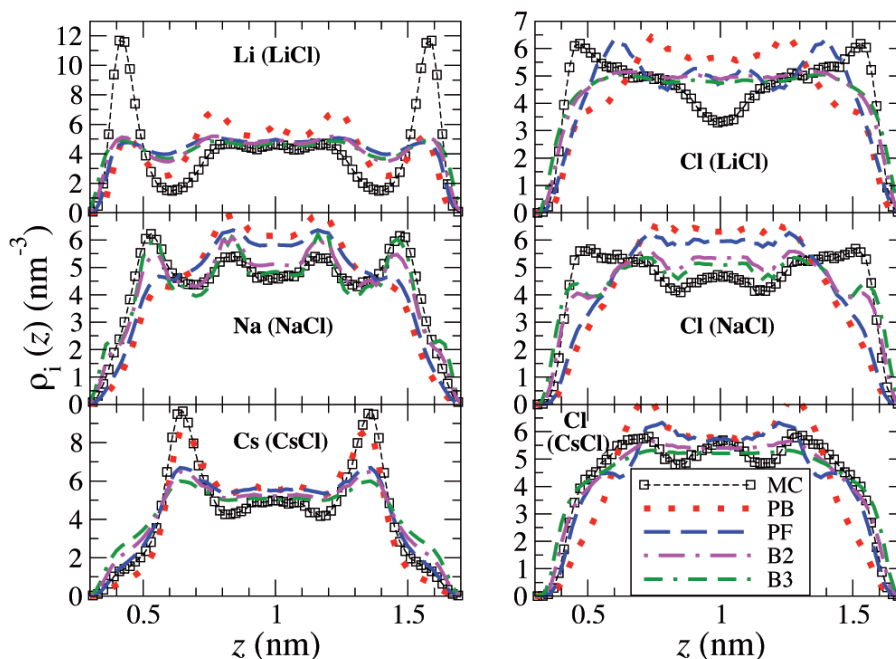
(b) $\bar{\rho} \simeq 5$ M and $\tau \simeq 6$ nm^{-2}

Figure 5.3.: *MC derived ion density profiles compared to Poisson-Boltzmann (PB), Poisson-Fermi (PF) and second (B2) and third order (B3) hard-sphere LDA expansions. LiCl, NaCl and CsCl are shown for $d = 2$ nm. The dielectric constant is chosen according to the formula $\epsilon(\bar{\rho}) = \frac{80}{[1+C \times (\bar{\rho}/M)]}$ in all cases with a salt specific constant C given in fig. 4.6 on page 46.*

(a) $\tau \simeq 3.6$ nm^{-2}

(b) $\tau \simeq 6$ nm^{-2}
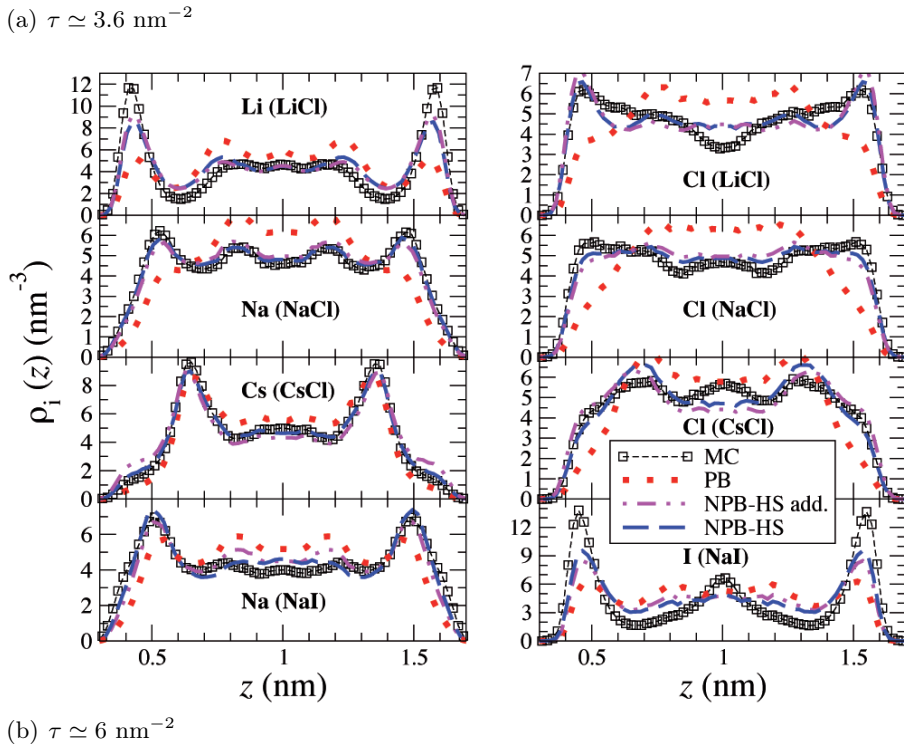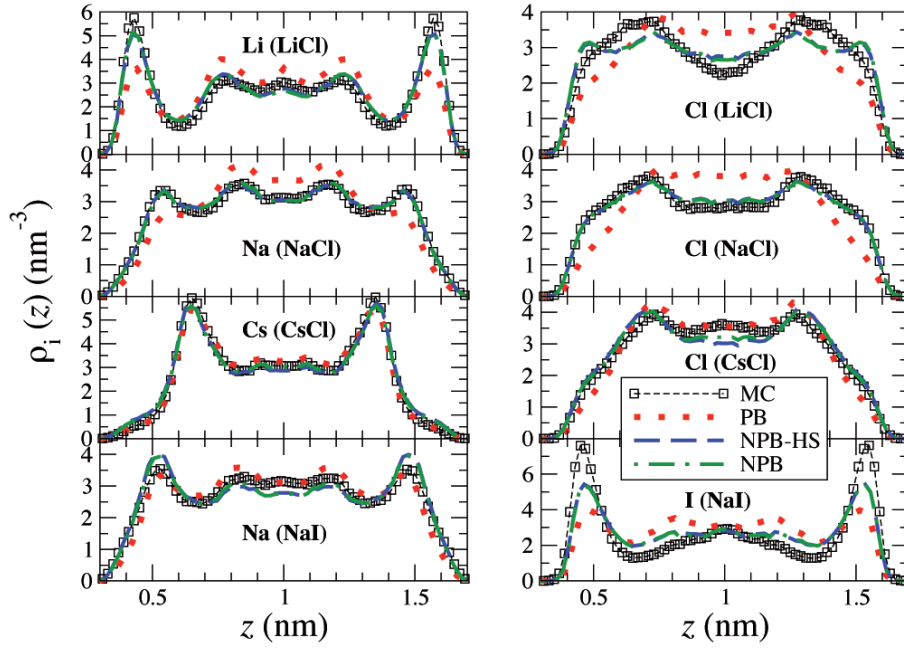
Figure 5.4.: *MC and PB derived ion density profiles for LiCl, NaCl, CsCl and NaI compared to nonlocal theories NPB-HS and NPB. Same distance d = 2 nm, ion area densities and dielectric constants as in fig. 5.3.*

Table 5.1.: *Total pressure exerted by the ions on one wall for LiCl, NaCl, CsCl and NaI. The system is the same as shown in figs. 5.3(b) and 5.4(b). The pressure for PB, LDA B3, additive (NPB-HS add.) and nonadditive NPB-HS is shown in terms of the relative error to MC pressure in percent. For NaI the B3 method failed to yield a stable result.*

Salt	P_{MC} (bar)	Relative error $= \frac{(P_{\text{MC}} - P_X)}{P_X}$ (%)			
		$X = \text{PB}$	$X = \text{B3}$	$X = \text{NPB-HS add.}$	$X = \text{NPB-HS}$
LiCl	1089	114	-22	-6	3
NaCl	993	90	-23	4	-5
CsCl	775	62	-29	-34	-16
NaI	1355	202	n/a	83	53

example the additive NPB-HS performs equally bad as the B3 method in terms of pressure while the nonadditive theory is better by a factor of 2. For NaI, which exhibits the largest positive nonadditivity ($\Delta_{+-} = 0.36 > 0$) of all salts studied, even the nonadditive NPB-HS underestimates the MC-derived pressure by roughly 50 %. We argue therefore that systems with large ions in terms of effective size and a high positive nonadditivity are dominated by excluded-volume interactions and need a more sophisticated treatment, as for example a nonadditive FMT approach [162].

Finally, in fig. 5.5 on the following page we show ion density profiles for LiCl and NaI for both negatively and positively like-charged surfaces. Since the system has to be electroneutral we observe an asymmetry in the cation and anion area densities in the form of $\sigma/e = \frac{\tau_- - \tau_+}{2}$, where σ is the surface charge density of one wall. This asymmetry leads to a very different ion structure depending on the nature of the counterions. NaI is an interesting example since Na^+ is the effectively smallest and I^- the largest ion in our study. For this reason, negatively charged walls lead to a relatively unstructured system, whereas positively charged walls lead to accumulation of counterions and depletion of coions at the surface. In the latter case there are roughly 4 times as many counterions than coions near the positively charged surface at $z \simeq 0.5$ nm. For negatively charged walls, on the contrary, there are roughly as many counter- than coions for distances $z \leq 0.6$ nm from the wall.

5.3. Donnan effect

In fig. 5.6 we show the dependence of the effective mean coion concentration $\bar{\rho}_s = \tau/d$ on the surface charge density in the case of positive and negative surface charges for LiCl and NaI. As the ion-wall interaction is repulsive close to the surface, the ions can not come indefinitely close. Hence, we do not recover the reservoir density ρ_0 for $\sigma = 0$. We will generally underestimate the effective mean coion concentration in terms of the (restricted) volume accessible to the ions. We are not bothered since we are interested in the *relative* decrease in salt concentration with the surface charge density. Indeed, the effective concentrations for neutral walls will also be different for PB and NPB-HS, given that in the grand canonical ensemble the particle number may vary for the same reservoir density $\rho_0 = 3$ M.
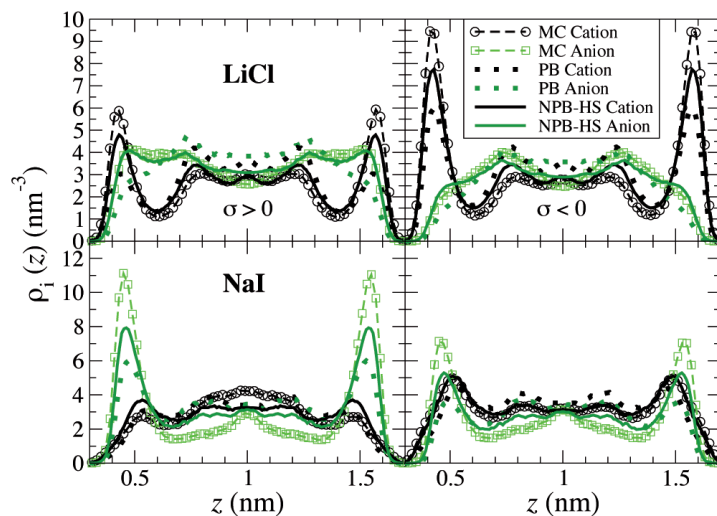
Figure 5.5.: *MC, NPB-HS and PB derived ion density profiles for LiCl (upper panels) and NaI (lower panels) for both positively (left) and negatively (right) like-charged surfaces in a $d = 2$ nm slab-confinement with surface charge densities $|\sigma| = 0.4\ e\ nm^{-2}$. The coion area density is $\tau \simeq 3.6\ nm^{-2}$ and the dielectric constant is set to 80.*

In fig. 5.6(a) we assess the effect of ion-ion correlations and ion-wall interactions on the Donnan effect in the case of negatively charged walls (sodium being the counterion) and positively charged walls (iodide being the counterion). We first turn our attention towards the results of PB and therewith "switch on" the ion-wall interactions only. We observe a more pronounced decrease in salt concentration in the case of negatively charged walls indicating that sodium depletes the coion concentration more than iodide does. We make the following assertion. The attractive part of the ion-wall pmf for iodide drives the counterions to the wall and therefore leading to a lower *effective* surface charge density than in the case of sodium being the counterion. We expect excluded-volume effects to depend particularly on the effective ion sizes of the counterions σ_{ij} and on the nonadditivity parameter Δ_{ij}. As stated in tab. 4.3 on page 44, NaI is a highly asymmetric and nonadditive salt. We anticipate that iodide as a counterion with an effective diameter of $\sigma_{--} = 0.47$ nm will squeeze out more salt than sodium that is less than half as big ($\sigma_{++} = 0.22$ nm). As we can see, this is what happens. The excluded-volume impact overcompensates the effect of the pmf so that the Donnan effect is overall greater for positive surface charges.

In order to validate our assessments we repeat in fig. 5.6(b) the same procedure for LiCl. The latter is a more symmetric and less nonadditive salt than NaI with an attractive part in the cation-wall pmf and a purely repulsive anion-wall interaction (see fig. 5.1 on page 54). Examining the results for the PB method, we recover the same trend as for NaI. The bigger the attraction/repulsion discrepancy between cation- and anion-pmfs the wider the gap in salt expulsion will be when changing the sign of the surface charge density. As to the excluded-volume correlations, the small relative change of salt expulsion between the PB and NPB-HS methods corroborates with the fact that LiCl
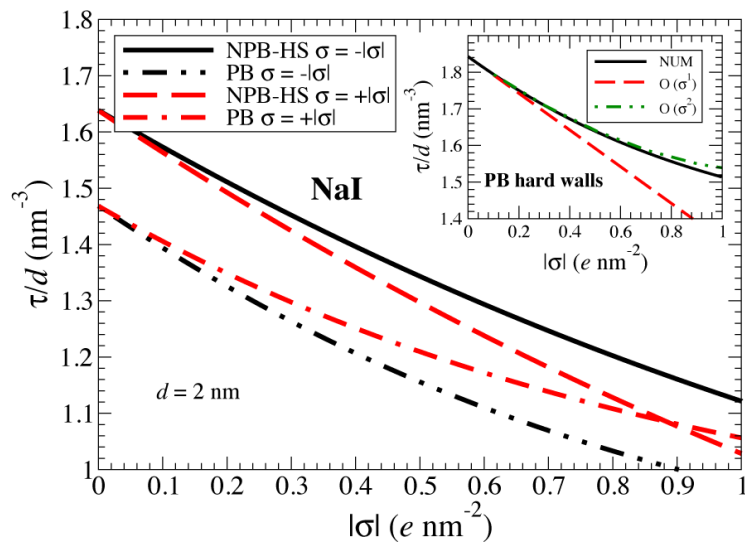
(a) NaI. Inset: numerical solution of the mean-field Poisson-Boltzmann theory
for an ideal gas between two hard walls compared to the analytical second
order expansion (3.79).
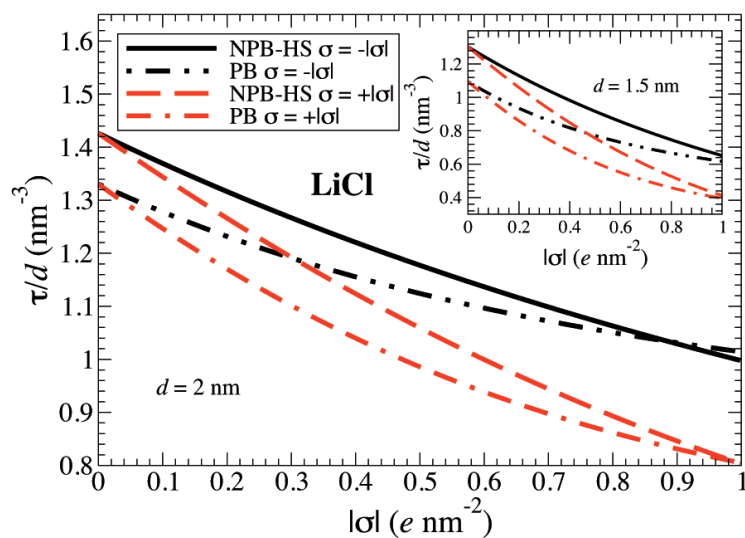
(b) LiCl. Inset: same effect for a smaller confinement of $d = 1.5$ nm

Figure 5.6.: *NPB-HS and PB derived Donnan effect in a $d = 2$ nm slab-confinement in the case of positively and negatively like-charging the walls. The reservoir density is $\rho_0 = 3$ M. The difference in effective concentrations $\bar{\rho} = \tau/d$ of the two methods for neutral walls ($\sigma = 0$) is due to different (reservoir) fugacities.*

is the most symmetric salt we study and does not display a big difference in the impact of ion-ion excluded-volume correlations switching cations for anions. In the inset of fig. 5.6(b) we show the same analysis with a smaller wall-to-wall distance $d = 1.5$ nm. We recover the same trends implying that our analysis is valid also for smaller confinements as long as the ion-wall PMFs of the two walls do not overlap.

5.4. Solvation forces

In fig. 5.7 we compare the solvation pressure $P_s(d)$ of LiCl for three different reservoir densities $\rho_0 = 1$, 3 and 5 M in an uncharged slab-confinement. As we increase the density, the pressure variations get more pronounced, in particular for NPB-HS. The loci of the maxima and minima stay untouched, a behavior that is expected since the ion-wall interactions are unaffected by the increase in concentration. The steric correction in turn is always repulsive and increases with ρ_0. We observe a change of one order of magnitude in the repulsive barrier going from $\rho_0 = 1$ M to $\rho_0 = 3$ M and of roughly a factor of two increasing the reservoir concentration from $\rho_0 = 3$ M to $\rho_0 = 5$ M. The repulsive barrier for $\rho_0 = 1$ M and $\rho_0 = 5$ M is $\simeq 0.4\ k_B T$ and $\simeq 55\ k_B T$, respectively, for two close colloidal surfaces with an area $A = 10$ nm^{-2}. This corresponds to a difference of two orders of magnitude.

In fig. 5.8 we choose a reservoir density of $\rho_0 = 3$ M and show the solvation pressure $P_s(d)$ obtained for charged and uncharged walls with PB and NPB-HS for LiCl, NaCl, CsCl and NaI. A common feature of all salts studied is the strong dependence of P_s on the shape of the ion-wall potentials V_i^{ext}. A nice example is LiCl with the cation partially attracted and the anion repelled from the surface. While a positive surface charge leads to a high solvation pressure mainly due to chloride counterions, P_s features regions of strong attraction for negative surface charges that are related to the loci and magnitudes of attraction in the ion-wall short-range potentials of the lithium counterions. We observe the same effect for NaI. The anion and cation V_i^{ext} of NaCl being similar translates into like shapes of P_s for positively and negatively charged walls in.

Turning our attention now to the steric correction we note another trait common to all salts. The mainly repulsive barrier induced by ion-ion correlations for uncharged surfaces decreases with increasing surface charges, independently of the sign of the latter. We explain this behavior with the following argument. For small confinements and high surface charges the pressure inside the slab is dominated by the force exerted by the counterions on the surfaces. We observe that for $d < 1.2$ nm the two pressures calculated with PB and NPB-HS start to converge. This is expected since nonlocality plays a less important role in confinements of dimensions as small as an effective ion diameter. Note that in general the ions do not come closer than ~ 0.38 nm to the walls (cf. fig. 5.1 on page 54). Since the term $P(\infty)$ of eq. (3.71) is always smaller for PB than for NPB-HS due to excluded-volume effects on a primitive model level, we obtain a mainly negative contribution to eq. (3.74) for small confinements and high surface charge densities. Indeed, fig. 5.8 shows that for $\sigma = \pm\ 0.4\ e$ nm^{-2} the solvation pressure for PB is always larger than for NPB-HS for wall-to-wall separations of $d < 1.1$ nm.
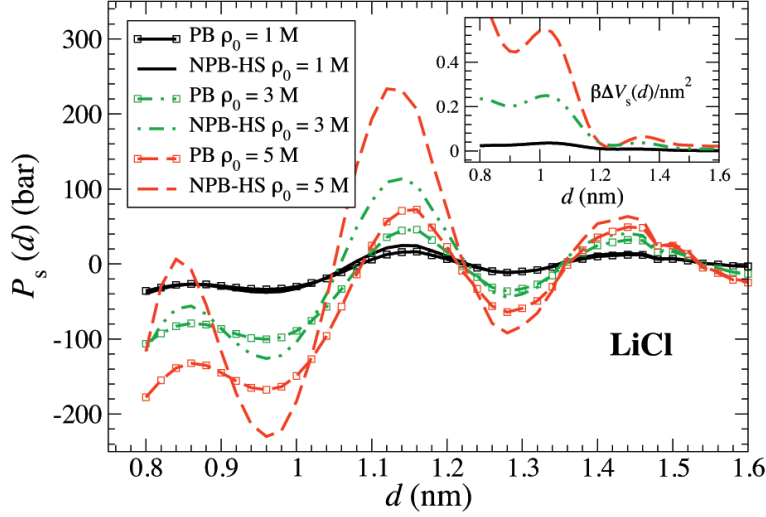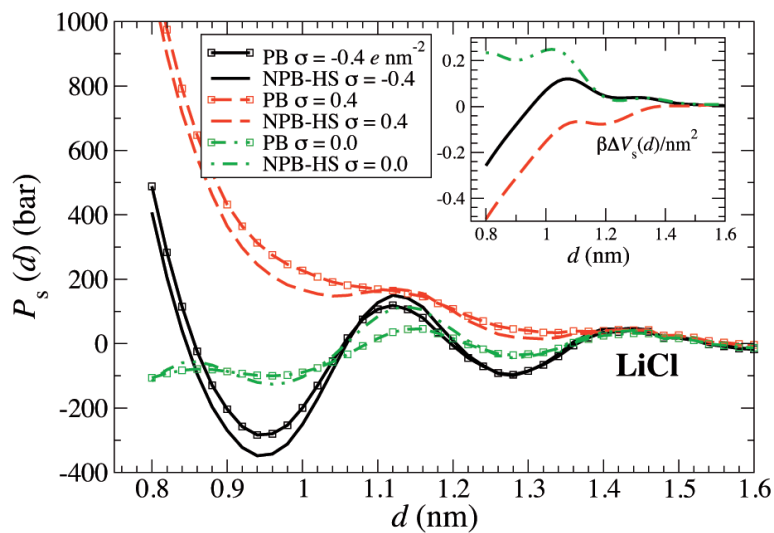
Figure 5.7.: *Distance resolved solvation pressure $P_s(d)$ for LiCl in the case of neutral walls. Results for three different reservoir densities $\rho_0 = 1,\ 3,\ 5$ M are shown. Inset: corresponding steric corrections for a unit area $A = 1$ nm^2.*

For LiCl only a very small repulsive barrier is still discernible for a negative surface charge density $\sigma = -0.4$ e nm^{-2} whereas for positive surface charges the steric correction becomes purely attractive. For NaCl, CsCl and NaI the steric barrier disappears independently of the sign of the surface charge and gives way to a purely attractive correction.

We corroborate at this point with the aforementioned study [160] that the steric correction due to ion-ion correlations is mainly attractive for highly charged surfaces, even though we operate on a primitive model where excluded-volume interactions are purely repulsive, whereas Burak and Andelman used an *attractive* correction. We also note that the form of the solvation interaction is strongly coupled to the ion-surface interaction and a *net* attraction can not be predicted without knowledge of the latter.

5.5. Overcharging

Overcharging is in essence known as the phenomenon where an electric double-layer appears to attract more charges from counterions than is needed to compensate for the surface charge. This effect is very important to evaluate long-range interactions between two charged surfaces in an electrolyte solution. Our aim in this paper is not to provide a detailed study of the phenomenon because we use only a simple hydrophobic surface and limit ourselves to monovalent ions. Indeed, detailed reviews as to the "physical" and "chemical" nature of overcharging can be found in literature [67, 185]. Our coarse-grained
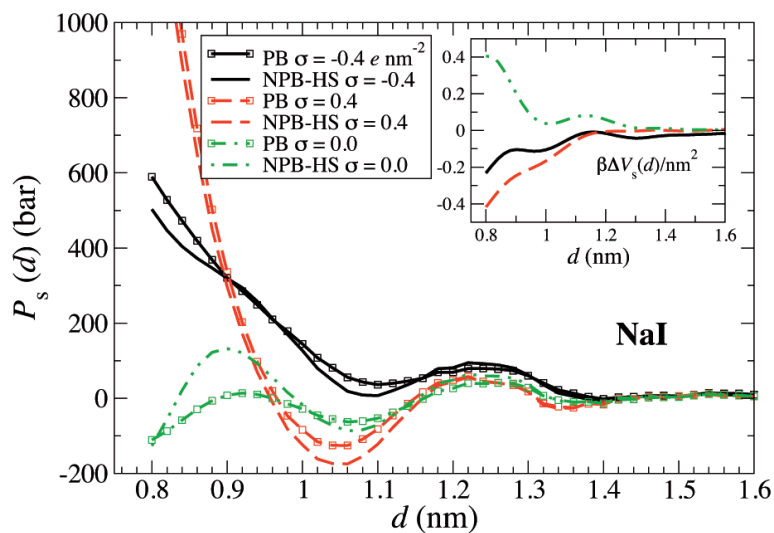
(a) LiCl.
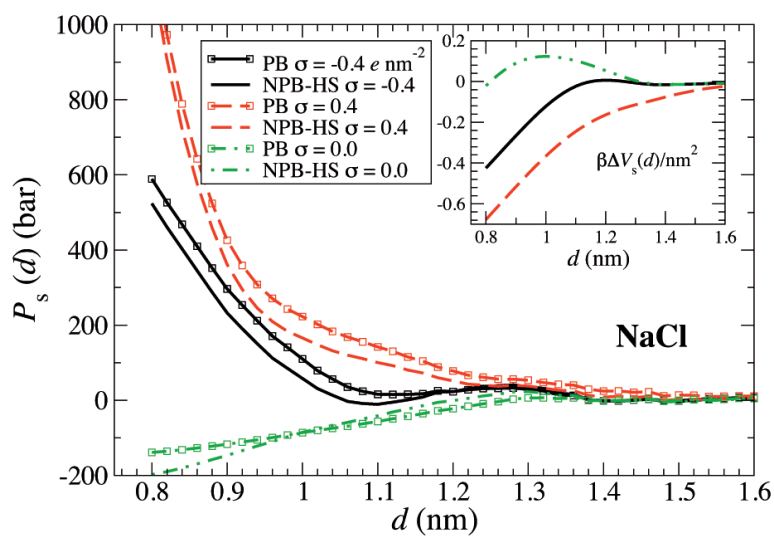
(b) NaCl.

Figure 5.8.: *Continued on the next page.*
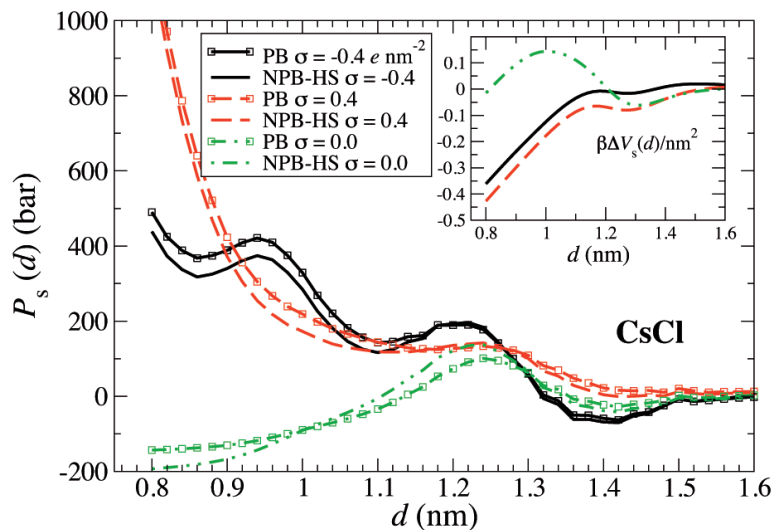
(c) CsCl.

(d) NaI.

Figure 5.8.: *Distance resolved solvation pressure $P_s(d)$ in the case of neutral and charged walls with a reservoir density of $\rho_0 = 3$ M. Results for surface charge densities of $\sigma = \pm 0.4$ e nm^{-2} are shown. Inset: corresponding steric corrections for a unit area $A = 1$ nm^2.*

methods PB and NPB-HS do, however, allow us to compare the effect of ion-specific ion-surface interactions and excluded-volume correlations on overcharging. In this simplified picture the nonelectrostatic ion-wall interactions mirror the role of "chemical" adsorption whereas ion-ion correlations mimic the "physical" component. More explicitly, we want to inspect the crucial role assigned to excluded-volume by the authors of a previous study [186].

We place one infinitely large surface in an ionic reservoir of concentration ρ_0. The system is equivalent to that of section 3.7 except for the fact that we examine only a single surface, meaning that we set the inter-surface distance d to infinity. To study overcharging we calculate the *net* charge area density in the system. This charge density is given by the surface charge density at the wall and decreases to zero for large distances to maintain electroneutrality. We obtain the net charge area density simply by integrating over the charge density of eq. (3.51) :

$$\sigma_{tot}(z)/e \ = \ \sigma/e \ + \ \int_0^z \rho(z')dz'. \tag{5.1}$$

We proceed with a similar analysis as in section 5.3. We first discuss results for the PB method and inspect the role of ion-surface interactions. We then compare them to results from NPB-HS where we "switch on" ion-ion excluded-volume correlations. In fig. 5.9(a) on the facing page we show the distance resolved net charge area density of a plate immersed in a LiCl electrolyte scaled by the surface charge density. We use surface charge densities of $\sigma = \pm 0.4 \ e \ \mathrm{nm}^{-2}$ and a reservoir density of $\rho_0 = 3$ M. The PB results show a distinct difference for negative (Li^+ being the counterion) and positive (Cl^- being the counterion) surface charges. If Li^+ is the counterion, the surface charge is compensated already at a small distance $z \simeq 0.5$ nm from the plate. The net charge area density is then shown oscillating around zero. In sharp contrast to the latter, in the case of a positive surface charge the net charge area density becomes even slightly more positive up to distances of $z \simeq 0.6$ nm and only then decays slowly to zero. These considerably different effects are obviously related to the ion-surface interaction that is attractive for Li^+ and repulsive for Cl^-. Fig. 5.9(b) exhibits a qualitatively similar picture in the case of NaI keeping in mind that in this case the anion is attracted to the interface whereas the cation is repelled. The trends are the same as for LiCl, even though we see no oscillations around zero of the net charge area density for a positive surface charge density, and the compensation of the latter is more linear for a negative surface charge. At this point, we note that overcharging in the absence of excluded-volume correlations is in our model only possible for very attractive interactions between the interface and the counterions or, analogously, very repulsive interactions between the coions and the surface.

We now turn our attention to the influence of excluded-volume correlations and thus to the results of the NPB-HS method. In fig. 5.9(a), for LiCl, the net charge area density switches sign for a negative surface charge. It exhibits a strong positive net charge area density of $\sigma_{tot}(z = 0.55 \ \mathrm{nm}) \simeq 0.13 \ e \ \mathrm{nm}^{-2}$. For a positive surface charge, on the contrary, the net charge area density even increases by almost 20 % at a distance
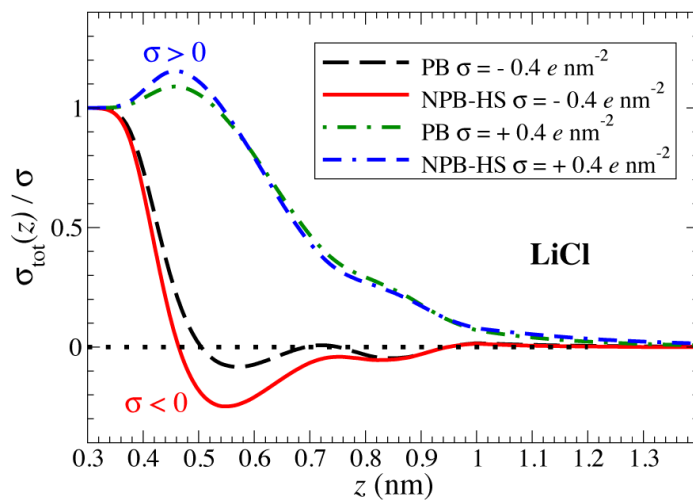
(a) LiCl.
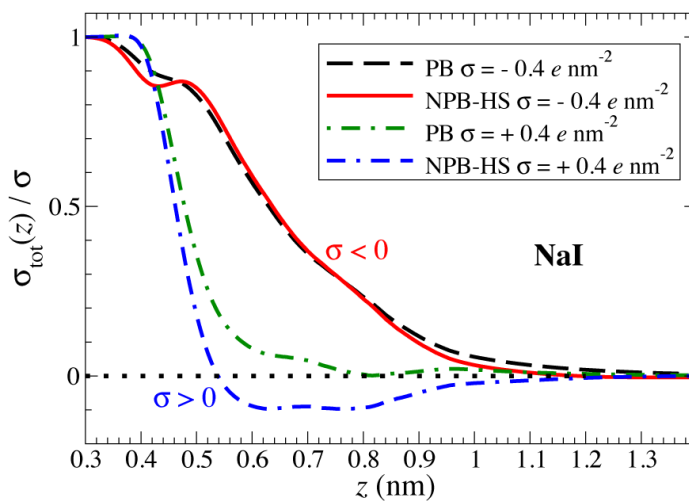
(b) NaI.

Figure 5.9.: *Distance resolved net charge area density $\sigma_{tot}(z)$ divided by the surface charge density. The reservoir density is $\rho_0 = 3$ M. Results for both negative and positive surface charge densities are shown with $\sigma = \pm 0.4$ e nm^{-2}.*

$z \simeq 0.51$ nm before declining slowly to zero. It is interesting that up to distances $z = 0.55$ nm the net charge area density is even higher than the surface charge density. For NaI we obtain in fig. 5.9(b) a continuous compensation of the negative surface charge density with increasing distance z. The positive surface charge, on the other hand, is compensated already at a distance $z \simeq 0.52$ nm and the net charge area density becomes negative for a distance range of $0.52 < z < 1.3$ nm. The scale of the observed overcharging might in this case be more of a lower limit because, reminiscent of our structural analysis of section 5.2.2, NPB-HS underestimates the excluded-volume correlations for NaI.

We can sum up our analysis stating that excluded-volume correlations can lead to overcharging for dense electrolytes. Nonetheless, the role of ion-specific ion-surface interactions is more important. Excluded-volume correlations can not lead to overcharging if the counterions are nonelectrostatically more repelled from the surface than the coions. In the latter case, ion-ion correlations can even increase the surface charge and thus lead to a competing effect to charge compensation.

5.6. Short summary

We used in this chapter the effective short-ranged ion-ion pmfs for LiCl, NaCl, CsCl, and NaI and similarly calculated ion-surface potentials in modified PB theories. We were therewith enabled to calculate the ionic structure and solvation forces of *dense* electrolytes in planar confinement. In order to assess the validity of the DFT-derived PB (DFT-PB) theories we performed both implicit-solvent Monte-Carlo (MC) and explicit-solvent MD simulations in a one-dimensional nanoconfinement. In our MC simulations, ions interact with the above pmfs, derived from MD at *infinite dilution*. Comparing MC and MD derived density profiles at finite salt concentration clarified that we can correct for (solvent-mediated) many-body interactions by choosing a realistic dielectric constant in the MC simulation, as was previously shown to be the case for bulk thermodynamic properties [27]. Then, comparing DFT-PB derived ion density profiles to MC, which treats nonelectrostatic *and* electrostatic ion-ion correlations *exactly*, enabled us to evaluate the local and nonlocal approximations in DFT as well as the validity of neglecting electrostatic ion-ion correlations at high salt concentrations.

We showed that the simplest-to-implement *nonlocal* approximation is able to correct for excluded-volume correlations in a wide parameter range. For this, we used effective BH diameters and treat the electrolyte as an *asymmetric* and *nonadditive* charged hard-sphere system. The BH diameters and the level of nonadditivity gave us a qualitative picture of the importance of excluded-volume correlations in the system. All *local* theories performed much worse than nonlocal PB (NPB), as was already hinted at in earlier work [184]. The computational simplicity of both PB and NPB methods permitted us to investigate the influence of excluded-volume correlations on salt expulsion between charged plates, the *Donnan effect*, on solvation forces between both like-charged and uncharged surfaces, and on overcharging of a single charged plate immersed in a dense electrolyte. Steric corrections, i.e., corrections due to ion-specific excluded-volume correlations, were found to amplify salt expulsion in all cases. Solvation forces are strongly

coupled to the ion-surface interaction and are therefore ion-specific. Steric corrections were found to be mainly repulsive for uncharged plates for all salts but disappeared or became attractive for highly like-charged surfaces at small separations. Further on, we observed that the charge distribution in the vicinity of a charged surface is mainly governed by ion-surface interactions but that excluded-volume correlations can trigger overcharging in a dense, highly correlated system. Finally, we emphasized that, even though the exact form of the ion-surface and ion-ion interactions depends strongly on the studied system, NPB can be used in general for a wide range of systems provided that ion-surface interactions and *effective* diameters of the ions are accessible.

Chapter 6

Crystallization Structure and Desalting: An MD study for NaCl

In this chapter we investigate a dense NaCl electrolyte at critical and supersaturated conditions. First, we show that crystallization in bulk is triggered in our simulations by supersaturations that exceed a certain threshold value. With the help of this robust kinetic criterion for fast crystallization we then investigate whether our nanoconfinement, consisting of two hydrophobic model surfaces in a pseudo grand canonical ensemble, impedes or facilitates fast crystallization at critical salt concentrations. In this context we will describe a desalting effect for very small surface-to-surface separations in the nanometer range. Finally, we will inspect fast crystallization patterns in the canonical ensemble for moderate supersaturations and different surface-to-surface separations.

6.1. Crystallization in bulk

In order to inspect the average hydration pattern around a single ion during crystallization, we first study the number of oxygen atoms in the first hydration shell for a single Na^+ and a single Cl^- atom in a water box. This endeavor is fairly simple and consists of three steps. We first compute the radial distribution function (RDF) between the ion and the water oxygen atoms. The first minimum in this RDF represents the outer boundary of the first hydration shell around the ion. The RDFs and thus the locations of the first minima differ for Na^+ and Cl^- as can be seen in the inset of fig. 6.1. The average number of water oxygen atoms within the first hydration shell—the ion-water coordination number—can then easily be obtained by simple counting atoms or, analogously, integrating the ion-oxygen RDF up to the location of the first minimum as shown previously in (3.2). The corresponding values are $n_+ = 5.9$, with the location of the first minimum in the Na^+-O RDF being $r_+ = 0.325$ nm, and $n_- = 7.2$, with the corresponding $r_- = 0.39$ nm for Cl^-.

We compute cation-anion coordination numbers in a similar fashion. Na^+-Cl^- RDFs have been computed in chapter 4. The first minimum in the RDF has been shown to be insensitive to electrolyte concentration and is located at $r_{+-} = 0.375$ nm. The cation-anion coordination number is concentration dependent and can be computed by simply counting the average number of cations within the first hydration shell of an anion or vice versa. In a perfect cubic crystal the cation-anion coordination number is $n_{+-} = 6$.

We simulate a dense NaCl bulk electrolyte for a range of different supersaturations, namely salt concentrations of $\rho \simeq 6.4$, 6.7, and 6.8 M (mol/l), or equivalently $\rho \simeq 7.9$, 8.3, and 8.4 m (mol/kg). The latter, considering that NaCl crystallizes experimentally roughly at $\rho = 6.1$ M [187], represent supersaturations of $\beta = 1.05$, 1.1, and 1.11, respectively. We want to point out at this point that the exact values are not particularly important because the exact supersaturation at which bulk sodium chloride crystallizes in a simulation depends on one hand on the force field and is on the other hand hard to estimate due to prohibitively long equilibration times. We will therefore use the term *fast crystallization* for a supersaturated electrolyte that forms a cluster of critical size, i.e., does not dissociate, after an equilibration time of $t = 180$ ns. This kinetic criterion is robust if the electrolyte exhibits fast crystallization above a certain threshold supersaturation while remaining in the dissociated state for lower supersaturations. As we will see in the following, this is indeed the case.

In the upper panel of fig. 6.1 we plot the average ion-water coordination number per ion n_+ and n_- with respect to time for the dense systems described before. As expected for such high concentrations, the latter is in all cases considerably lower than at infinite dilution. A more characteristic feature is that above supersaturations of $\beta = 1.11$ we observe that the coordination number decreases drastically within the equilibration period and converges to a new equilibrated value. The latter effect is probably due to the incipient crystallization process. We observe the same trend (not shown) also for supersaturations of $\beta = 1.01$ (no fast crystallization) and $\beta = 1.13$, 1.18 (fast crystallization). In order to confirm this assumption we inspect in the following cation-anion coordination numbers.

In the lower panel of fig. 6.1 we plot the Na^+-Cl^- coordination number n_{+-} with respect to time for all inspected supersaturations. We discover a clear analogy between the average ion-water and the cation-anion coordination number. The ion-water coordination number drops within the same time frame as the cation-anion coordination number surges. The latter does not equilibrate to $n_{+-} = 6$, the value expected for a perfect cubic crystal, due to the remaining ions that stay in solution. Our conclusion so far is twofold. On one hand, we can state that both average ion-water and cation-anion coordination numbers per ion are valuable proxies for the fast crystallization process and corroborate with previous work [108]; on the other hand we observe that fast crystallization occurs above a threshold supersaturation, roughly $\beta = 1.11$ in our specific case. The exact value of the latter depends obviously on the considered time frame but is not of major importance for our approach. As mentioned before, determining a more general and exact threshold supersaturation for crystallization of NaCl in simulation requires more sophisticated methods [105, 106] and/or much longer simulation times and is thus out of
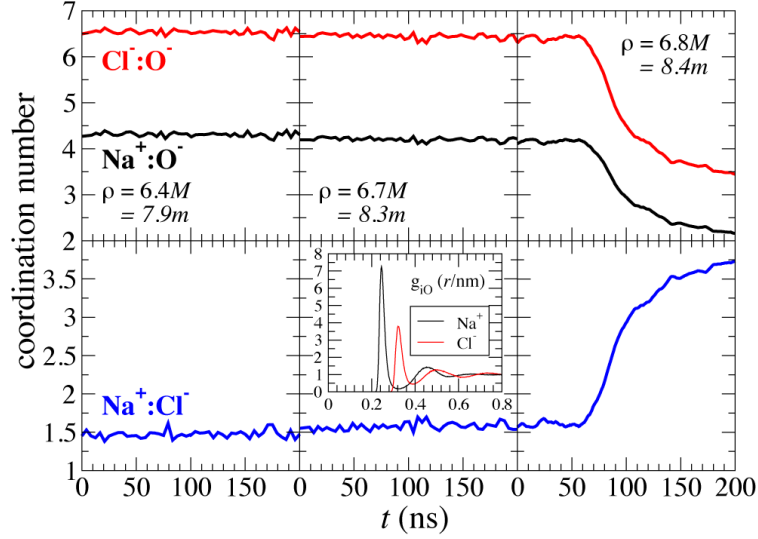
Figure 6.1.: *Average coordination number in bulk for the $Na^+ : Cl^-$, $Na^+ : O^-$ and $Cl^- : O^-$ pairs, where O^- denotes the oxygen atom of the water molecule, plotted with respect to time for different salt concentrations. Inset: Rdfs between an ion and the oxygen atom of the water molecule for both one Na^+ cation and a Cl^- anion.*

scope of this work.

We finally scrutinize the form of the formed NaCl clusters. An MD simulation snapshot of the latter is shown in fig. 6.3. Experimentally, one expects to find a so-called NaCl cubic lattice structure. We therefore calculate the structure parameter ψ_4 which is defined as

$$\psi_4 = \left\langle \frac{1}{N_{\text{layer}}} \sum_{i=1}^{N_{\text{layer}}} \frac{1}{N_i^b} \left| \sum_{j=1}^{N_i^b} \exp(i4\theta_j) \right| \right\rangle , \tag{6.1}$$

where we sum over N_{layer} layers of the crystal in (100) direction, N_i^b being the number of nearest neighbors of particle i, and θ_j being the angle of bond vectors between particles i and j. Note that a perfect square lattice corresponds to a value of $\psi_4 = 1$. We perform the analysis for supersaturations of $\beta = 1.11$, 1.13, and 1.18, and average over 4 layers of the NaCl cluster. We let the system equilibrate for $t = 180$ ns and then average over a time window of $\Delta t = 20$ ns. The obtained values do not depend crucially on the level of supersaturation and are roughly $\psi_4 \simeq 0.7$, a very high value considering that a perfect crystal structure is not possible due to kinetic reasons.

We conclude that in our bulk simulations sodium chloride exhibits fast crystallization into a cubic lattice NaCl structure for supersaturations above $\beta = 1.11$.

6.2. Salt expulsion in the grand canonical ensemble

It is well established that confinement can induce preliminary freezing between two hard walls for a one-component system [94, 95]. In this section we will investigate whether this confinement induced freezing can also be observed for a slab-water-salt system between our two simple hydrophobic walls.

We use a simple setup. We simulate a dense NaCl solution in the pseudo grand canonical ensemble described above at roughly $\rho \simeq 6.1$ M, a high but subcritical concentration in terms of fast crystallization in bulk in order to avoid salt clustering in the reservoir. After an equilibration time of $t = 180$ ns we gather data for $\Delta t = 20$ ns. Since we know from the previous section that fast crystallization is strongly linked to the level of supersaturation, we compute both the molality inside the slab and in the reservoir by simply counting water molecules and salt atoms. For this, we delimit the slab in $y-$direction by the centers of the outer surface C-atoms of one wall (cf. fig. 6.2). With the latter method we obtain a molality of $\rho \simeq 5.1$ m inside the slab and $\rho \simeq 6.4$ m in the reservoir. We observe therefore that the concentration in terms of molality in the reservoir is 25% higher than inside the slab. The latter shows that ions are expelled from the slab and that therefore the necessary supersaturations for fast crystallization might not be reached between the hydrophobic walls for a reservoir at critical supersaturation. A further analysis of the cation-anion coordination number for atoms inside the slab yields a constant value of $n_{+-} = 1.75$ for both equilibration and production period. Fig. 2.1(b) on page 10 represents a snapshot of the MD simulation after equilibration. Obviously no clustering of the salt inside the slab occurred.

Since salt is apparently expelled from the slab, we expect for small confinements a desalting effect, similar to dewetting. Hence, we simulate an NaCl electrolyte in our pseudo grand canonical ensemble using a reservoir concentration of $\rho \simeq 2$ M for surface-to-surface distances of $d = 1.0$, 1.2, 1.3, 1.4 and 1.5 nm. The simulation time is $\Delta t = 50$ ns after an equilibration time of $t = 5$ ns, the latter is sufficient since we do not expect fast crystallization inside the slab due to very low local salt concentrations. The starting configuration, before equilibration, always involves a slab filled with water and ions. In fig. 6.2 we show simulation snapshots and in tab. 6.1 we plot average salt densities in and outside (in the reservoir) the slab for all investigated surface-to-surface distances. We observe dewetting for $d = 1.0$ nm, corroborating with earlier, similar but larger scale simulations [188], i.e., all water molecules are expelled from the slab and with it all salt for the entire simulation time. For hydrophobic nanopores, it has been observed before that ions do only permeate the pore in the presence of water molecules [189]. For $d = 1.2$ nm we observe that water from the reservoir is reentering the slab for both equilibration and production run so that the filled configuration is the stable one, as observed before for two paraffin plates immersed in water for surface-to-surface distances $d \geq 1.1$ nm [190]. The water occupancy in the slab does not exhibit wetting/dewetting transitions as has been observed for the nanopore system [189]. Interestingly, all salt atoms stay in the reservoir, the latter confirmed by an average number of cations and anions around 1.5. As we proceed to larger surface-to-surface distances, Na$^+$ and Cl$^-$ ions reenter and the
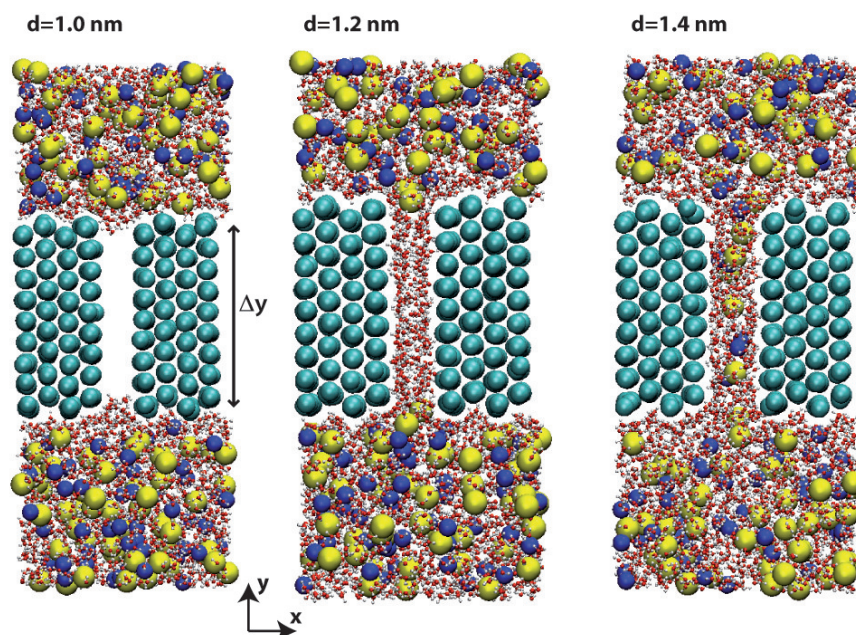
Figure 6.2.: *Snapshots of MD simulations in a pseudo grand canonical ensemble after equilibration for a reservoir salt density of roughly $\rho \simeq 2$ M and three different surface-to-surface distances: a) $d = 1.0$ nm; b) $d = 1.2$ nm; c) $d = 1.4$ nm. The confinement is delimited in y direction by the center of the outmost surface C-atoms, as depicted by Δy in a). The colorscheme is equivalent to fig. 2.1.*

molality inside the slab equilibrates to a value of roughly $\rho \simeq 1$ m for $d = 1.5$ nm, a concentration much lower than in the reservoir. The concentrations inside the slab and in the reservoir are summarized in tab. 6.1.

Therefore, a one-dimensional confinement of two hydrophobic walls in the grand canonical ensemble does not promote fast crystallization of sodium chloride. On the contrary, Na^+ and Cl^- ions can be expelled completely from the slab for small enough confinements leading to a desalting effect. We underline that this effect depends on the ion-surface interaction and is therefore not only ion-specific but can also be altered by the morphology of the wall, substituting the hydrophobic surface by a hydrophilic one for example. Substituting the NaCl salt with NaI would, as another example, not lead to a desalting effect since I^- is attracted to the wall (cf. fig. 5.1 on page 54). Further on, the lateral size of the confinement is expected to enhance the effect as reported for dewetting [188].

6.3. Crystallization in confinement

The study of dense electrolytes in the canonical ensemble seems to be less relevant to an experimental setup than in the grand canonical ensemble. Furthermore, it poses a range of problems. The chemical potential of water cannot be easily fixed through a bulk reservoir and a realistic water density inside the slab is hard to estimate. Salt crystal-

Table 6.1.: *Average salt density inside a nanoconfinement between two simple hydrophobic walls in a pseudo grand canonical ensemble for different surface-to-surface distances d, some of them shown in fig. 6.2, and a reservoir salt density of roughly $\rho \simeq 2.5\ m \simeq 2\ M$. For $d = 1.0\ nm$ dewetting occurs and the salt density cannot be computed.*

d (nm)	1.0	1.2	1.3	1.4	1.5	2.5
ρ_{slab} (mol/kg)	N/A	0.32	0.66	0.83	1.0	5.0
ρ_{res} (mol/kg)	N/A	2.25	2.5	2.5	2.50	6.4

lization in a one-dimensional model-confinement is experimentally typically induced by gradual evaporation until a critical supersaturation is reached and crystallization ensues, as in a recent investigation of supersaturated NaCl in a model-confinement [191]. The water density in such a model-system depends for example on temperature and pressure and particularly on the level of supersaturation. Despite those issues, we think that simulating a supersaturated electrolyte in the canonical ensemble for a certain effective salt concentration is instructive in order to analyze crystallization patterns and stress inside the slab. As we have seen in the previous section, the latter is difficult in the grand canonical ensemble due to prior fast crystallization in the reservoir for moderate supersaturations.

Unlike in the case of the grand canonical ensemble, the level of supersaturation in the canonical ensemble is harder to evaluate due the the difficulty in assessing the *effective* salt concentration inside the slab. Additionally, the system can be very inhomogeneous so that the local salt concentration next to the surface and in the middle of the slab are often very different. The local ion concentrations do indeed depend strongly on the exact form of the water-induced ion-surface interaction. Since both Na^+ and Cl^- are repelled from our hydrophobic model surface, we suspect the local salt concentration to be very high in the middle of the slab for small confinements in the nanometer range.

In order to study the influence of a slab-like nanoconfinement on fast crystallization of NaCl we will study in the following a slab-water-salt system at moderate supersaturations. The exact level of supersaturation is on one hand hard to evaluate and can even be locally very different within the slab, as stated before, but is on the other hand largely irrelevant for our purpose since we know from the previous section that above a certain threshold fast crystallization always occurs in a bulk system. We will therefore choose and set an effective concentration of $\bar{\rho} \simeq 5$ M, which is supposed to lead to a sufficiently high salt concentration locally inside the slab to trigger fast crystallization. In terms of molality the concentration is maintained at $\rho = 6.5 \pm 0.1$ m. A summary of the systems with different surface-to-surface distances d studied is given in tab. 6.2 on page 79.

In fig. 6.4 we show ion density profiles for 4 different systems. The profiles are averaged over $\Delta t = 20$ ns after an equilibration time of $t = 180$ ns. As a first observation, we can state that, even though being a hydrophobic surface, the water molecules show a higher propensity next to the wall than the ions. The latter signifies that the volume available to the water molecules inside the slab is higher than the volume available to the ions. We will therefore, reminiscent of our definition of the effective concentration

Figure 6.3.: *Snapshots of typical MD simulations in the canonical ensemble after an equilibration time of $t = 180$ ns. Snapshots for two different distances are shown: a) $d = 2.0$ nm; b) $d = 2.5$ nm. In c) a zoomed-in picture of the NaCl cluster of b) is shown in the $x - y$ plane. The colorscheme is equivalent to fig. 2.1.*
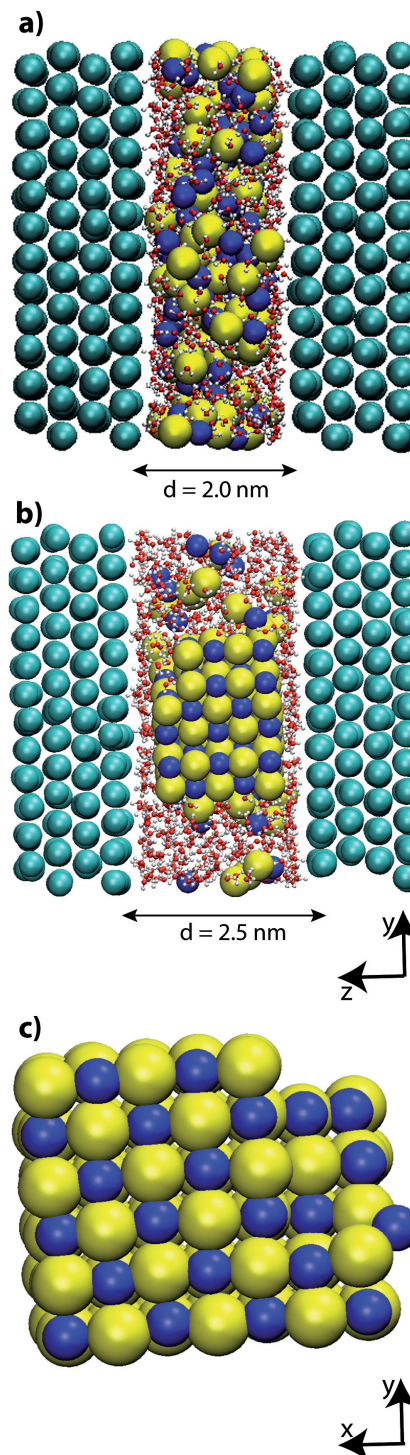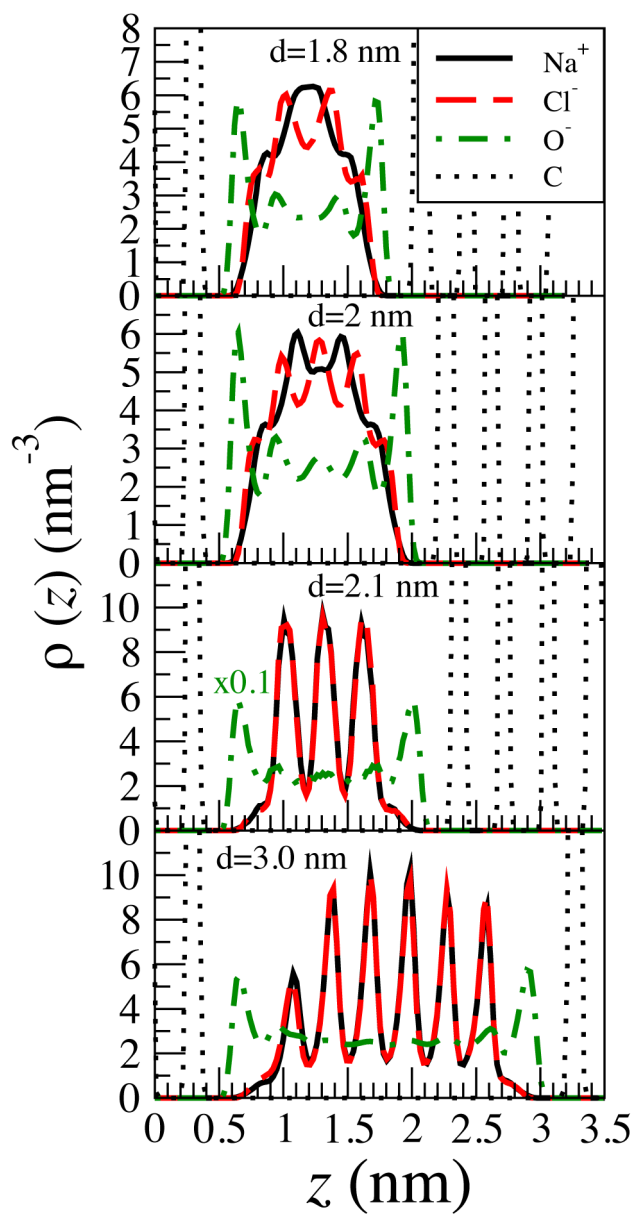
Figure 6.4.: *MD-derived density profiles in the canonical ensemble after equilibration at a moderate supersaturation for d = 1.8, 2.0, 2.1 and 3.0 nm. The effective concentration remains constant and is roughly $\bar{\rho} \simeq 5$ M. Density profiles for Na^+ (full), Cl^- (dashed), water oxygen (dot-dashed) and the wall C-atoms (dotted) are shown. The water oxygen density profiles are divided by 10 for a better view.*

Table 6.2.: *Effective concentrations for MD simulations in the canonical ensemble for different surface-to-surface distances d. Concentrations are given in terms of molality ρ and molarity $\bar{\rho} = \frac{N}{L_x L_y d_{wat}}$.*

d (nm)	1.8	2.0	2.1	2.5	3.0
$\bar{\rho}$ (mol/l)	5.0	5.0	5.0	5.0	5.0
ρ (mol/kg)	6.6	6.4	6.6	6.5	6.4

$\bar{\rho} = \frac{\tau}{d_{wat}}$ underestimate the local ion concentration in the middle of the slab for very small confinements and will recover the given $\bar{\rho} = 5$ M for very large confinements. In this latter case we will actually not observe fast crystallization anymore as we expect bulk behaviour with a threshold concentration around 6.5 M, i.e., considerably higher than our average concentration of $\bar{\rho} \simeq 5$ M.

The two lower panels of fig. 6.4 show density profiles for two different wall-to-wall distances $d = 2.1$ nm and $d = 3.0$ nm. The ion density profiles for anions and cations overlap, hinting to a strongly oriented crystal. They furthermore show distinct peaks along the z-direction, which points to a crystal that is layered in sheets parallel to the surfaces. This is indeed the case as can be seen in fig. 6.3, which shows an MD snapshot after equilibration of the system for $d = 2.5$ nm. The peaks observed in the ion density profiles clearly correspond to the sheets in the NaCl crystal structure seen in the MD snapshot. Further on, we observe a layer of water molecules between the outer crystal layer and the confining surfaces. Moreover, fig. 6.3 clearly shows that the ion density profile is not nil between the ion crystal layers. This is due to remaining "loose" ions, not forming part of the crystal, that remain even after equilibration.

The ion density profiles for wall-to-wall distances of $d = 1.8$ nm and $d = 2$ nm shown in the upper panels of fig. 6.4 exhibit strikingly different properties. Neither do the cation and anion profiles overlap, nor do they display a similarly structured shape. We suspect that the system does not show fast crystallization even though both local cation and anion concentrations in the middle of the slab are around $\rho \simeq 8$ M and thus around 30% higher than the threshold concentration for fast crystallization seen in bulk. The snapshot of the system with $d = 2$ nm after equilibration shown in fig. 6.3 does not show a crystalline order and supports the assumption that no fast crystallization takes place.

In the lower panel of fig. 6.5 we show for wall-to-wall distances of $d = 2.1$ nm and $d = 3.0$ nm the average hydration number per ion for cations and anions with respect to time for the whole simulated time interval, i.e., equilibration and subsequent production run. We observe a steep decline in the hydration number for wall-to-wall distances of $d = 2.1$ nm and $d = 3.0$ nm while for $d = 1.8$ nm and $d = 2$ nm it remains constant over the whole time span (not shown), corroborating with the form of the density profiles seen in fig. 6.4. Moreover, for $d = 2.1$ nm and $d = 3.0$ nm, the average hydration number for cations and anions converges to 2 and 3.5, respectively. The latter means that fast crystallization occurs until a critical cluster size is reached and, akin to the bulk situation, the salt concentration in solution is not sufficient anymore to ensure further crystal growth [192]. For illustrative purposes we show in fig. 6.6 on page 82 MD
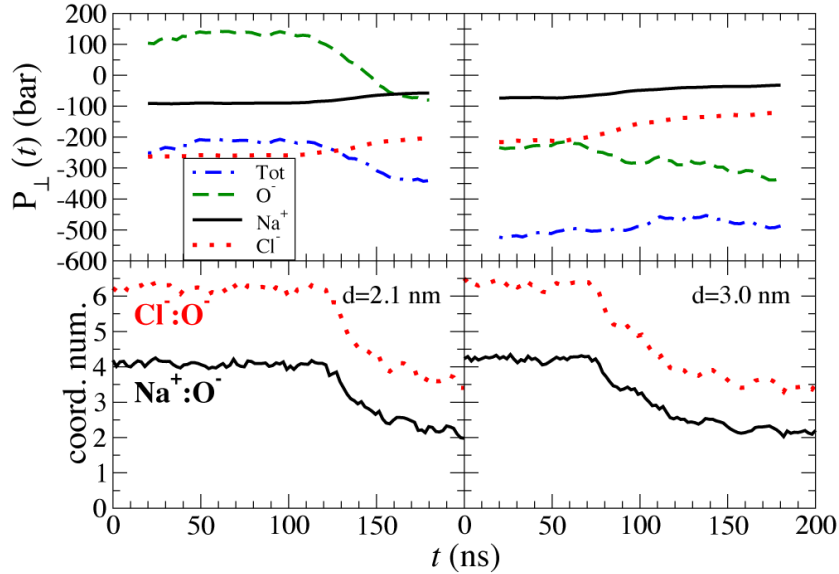
Figure 6.5.: *Pressure exerted on the walls in perpendicular $z-$direction before, during and after fast crystallization in the canonical ensemble at moderate supersaturations for two surface-to-surface distances $d = 2.1$ nm and $d = 3.0$ nm. The pressure is plotted component-by-component (upper panels) for Na^+ (full), Cl^- (dotted) ions and the water oxygen (dot-dashed) molecules, as well as the sum of all components (dot-dashed). The ion-water coordination number (lower panels) is plotted as a proxy for fast crystallization.*

snapshots for the $d = 3.0$ nm system at a time frame that corresponds to roughly 20 ns after crystallization starts, i.e., at $t_1 = 90$ ns, and after equilibration, i.e., at $t_2 = 180$ ns. We observe that at t_1 a critical cluster evidently formed in the middle of the slab, but does not exhibit the same sheet structure parallel to the confining surface as observed after equilibration at t_2. The latter suggests that the regular equilibrium structure is only attained after equilibration and that crystal growth proceeds in a more isotropic fashion.

We finally analyze the pressure exerted on one wall by the ions and the water molecules during fast crystallization. In the upper panels of fig. 6.5 we plot both the total and component-by-component pressure on one wall with respect to time for the systems with $d = 2.1$ nm and $d = 3.0$ nm, i.e., the systems that exhibit fast crystallization. We observe immediately that the pressure induced by both cations and anions is always negative and subsequently attractive on the walls. The pressure exerted by the water molecules, on the other hand, can be both repulsive and attractive. The latter is rather surprising since water between hydrophobic plates is known to exert a purely attractive force [54]. We explain this anomaly by the following argument. The perpendicular pressure exerted by the water molecules in a nanoconfinement is highly dependent on the average water density inside the slab in the canonical ensemble. A realistic value of the latter is hard to evaluate in an MD simulation and we additionally suspect the number of water molecules in the slab to depend crucially on the ensemble used. We thus expect

the total perpendicular pressure of the water molecules to be rather arbitrary. We will therefore focus on the *relative change* of the pressure components before, during and after fast crystallization only. We observe that for both $d = 2.1$ nm and $d = 3.0$ nm the pressure exerted by the cations and anions increases only feebly during fast crystallization. The water exhibits a more pronounced decrease in pressure. Considering the change in total pressure on the walls the picture remains inconclusive, given a decrease in pressure for $d = 2.1$ nm and a slight increase for $d = 3.0$ nm. We conclude that for a supersaturated NaCl crystal the pressure on the wall that originates from fast crystallization seems to be of minor importance. Considering earlier speculations [80, 193, 194], this might on one hand be due to the even shape of the perfect, smooth-faced cubic NaCl crystal sheets and on the other hand to the thin water layer between the crystal and the wall that limits the amount of stress exerted on the surface by the ion cluster. It has been speculated before that the crystallization pressure of cubic halite crystals on confining surfaces is expected to be small [80, 193, 194].

6.4. Short summary

In this last chapter we showed that fast crystallization in bulk is triggered in our simulations by supersaturations that exceed a certain threshold value. We then simulated a slab-water-salt system—using simple model surfaces—in a pseudo grand canonical ensemble at close to critical reservoir salt concentration. We probed hereby whether confinement induced freezing takes place, i.e., that fast crystallization is triggered by the slab geometry. Salt was shown to be expelled from the slab and the effective ion concentration inside the nanoconfinement to be always considerably lower than the reservoir salt concentration so that no fast crystallization takes place inside the confinement. We additionally described that for very small surface-to-surface distances ($d < 1.5$ nm) salt is almost entirely expelled, while water remains in the slab. Hence, in order to study fast crystallization in confinement, we simulated NaCl at moderate, above threshold, supersaturations in the canonical ensemble. We observed formation of salt clusters that exhibit a cubic lattice structure as observed in our bulk simulations but are in addition arranged in sheets parallel to the surface. Further on, a water film of roughly half a nanometer in size perpendicular to the surface was found to remain between the crystal and the surface and thus prevented direct contact between the salt cluster and the wall. We finally inspected the pressure exerted by the salt ions and the water molecules on the walls during fast crystallization and observed that the change in pressure between the walls during the latter is small.
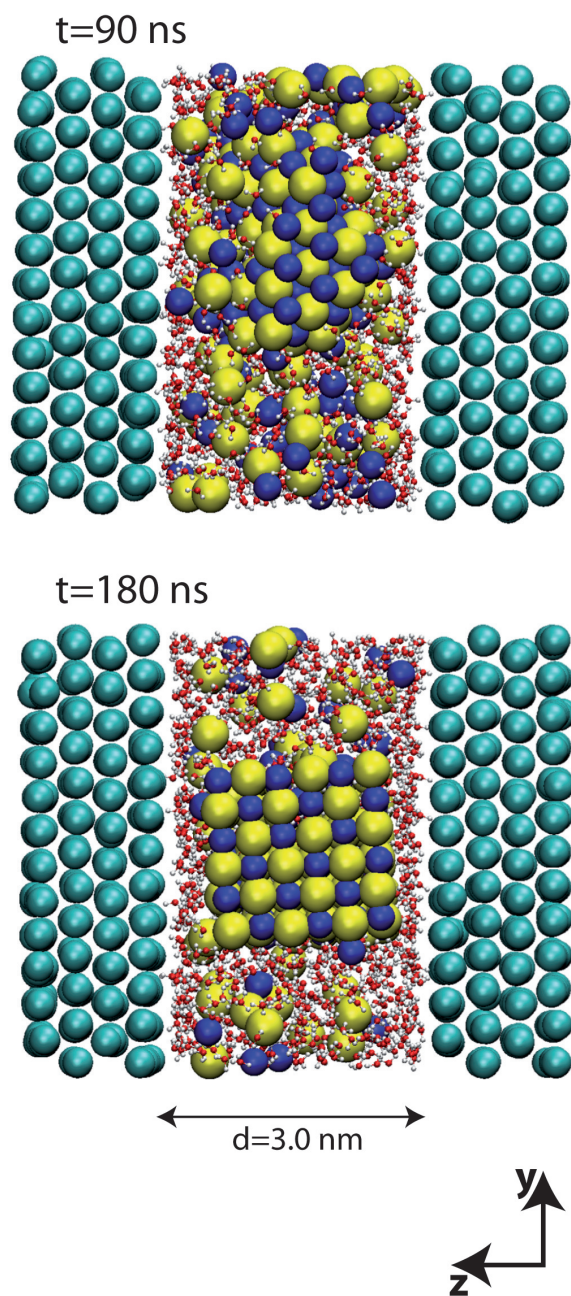
t=90 ns

t=180 ns

d=3.0 nm

y

z

Figure 6.6.: *MD snapshots of a simulation in the canonical ensemble for a surface-to-surface distance of d = 3.0 nm at two different time frames. At t = 90 ns (upper panel) a critical salt cluster has been formed in the middle of the slab but no equilibrium has been reached. At t = 180 ns (lower panel) the equilibrium configuration is depicted. The colorscheme is equivalent to fig. 2.1.*

Chapter 7

Summary and Outlook

The aim of this thesis was to analyze and understand ion-specific effects on an atomistic level, a subject that has gathered considerable attention in the last 10 years and remains a matter of vivid research. We investigated ion-specific thermodynamics and ionic structure in both bulk and (nano)confinement geometries. We presented methods that can be used for a wide range of systems, such as multivalent ions and/or biological surfaces. However, we focused on the study of alkali halides at salt concentrations in the molar range and used a simple hydrophobic model surface.

After presenting the computational and theoretical tools used in this work in chapters 2 and 3, we analyzed bulk properties of aqueous electrolytes in chapter 4. We first calculated the microscopic fluid structure—in the form of pair correlation functions $g(r)$—for concentrated LiCl, NaCl, KCl, CsCl, NaI, and KF solutions employing all-atom MD simulations. We used the pair correlation functions to obtain accurate short-ranged nonelectrostatic pair potentials and effective ion-ion diameters from MD simulations. In a second step, the short-ranged, solvent-induced structure was integrated using liquid state theory to obtain the osmotic coefficient, allowing for a systematic investigation of structural consequences to macroscopic behavior. The concentration dependent osmotic coefficients showed good agreement to experimental data for the chloride salts, while NaI and KF performed worse.

Current force fields of electrolytes, e.g., for use in biochemical simulations, are generally benchmarked to single ion properties only. Our results demonstrate that it is crucial for future force field refinement to additionally include collective bulk properties. Ongoing work in our group showed that such a procedure works well for some alkali halides but proves to be more difficult for certain salts as for example KF [53]. It is tempting to speculate that the inclusion of ion polarizabilities, neglected in the classical LJ force fields, might be critical for a correct modeling of the F^- anion.

In chapter 5, we turned our attention to dense electrolytes in a nanoconfinement. More specifically, we calculated for LiCl, NaCl, CsCl, and NaI the ionic structure—in the form of ion density profiles—between two simple hydrophobic model surfaces by means of explicit-water MD simulations, implicit-water MC simulations and modified PB theories. By taking into account a density-dependent dielectric constant, we found that the results of the MC simulations agree in general well with MD. We then showed that a simple nonlocal modification to PB—treating the electrolyte as an asymmetric and non-additive hard-sphere system using the ion-ion diameters calculated in chapter 4—is able to reproduce the ionic structure of the MC simulations, that treat ion-ion correlations exactly on a two-body level. We additionally suggested a method to include electrostatic correlations in a similar way in order to study highly charged systems. Solvation forces between like-charged plates were found to be highly ion-specific and dominated by the (counter)ion-surface potential, while the steric correction (due to excluded-volume correlations) was mainly repulsive for high salt concentrations and low surface charges. We therefore suspect excluded-volume correlations to play an important role in the restabilization of colloidal suspensions at high salt concentrations described in the introduction of this thesis.

Our findings in this chapter provide a common framework that permits to include both excluded-volume correlations, that are important for very dense systems, and electrostatic correlations, that are important for highly charged systems, on an ion-specific level. Such a framework is well suited to be implemented in coarse-grained biochemical simulations, that currently treat ions on a mean-field level only. An obvious important issue still to be tackled is the extension of the method to more complex geometries, where curvature plays a significant role, for instance, ion channels [195, 196] or charged protein binding pockets [197], where locally the ion concentration can be enormous. Recent work highlights that this is indeed feasible [198]. Our methods could then be implemented in existing continuum Poisson-Boltzmann solvers like the Adaptive Poisson-Boltzmann Solver (APBS) [199]. Future investigations should also include more realistic, biologically relevant surfaces in order to compare theoretical results to experimental measurements.

In chapter 6, we singled out the NaCl salt and investigated crystallization in bulk and nanoconfinement geometries by means of MD simulations. In bulk, we found crystallization to be triggered by a threshold supersaturation. In confinement, conclusions depend on the morphology of the confining surfaces and on the considered ensemble. For hydrophobic model surfaces, we found both Na^+ and Cl^- ions to be expelled from the slab in a pseudo grand canonical ensemble, and did for this reason not observe crystallization inside the slab. Even more, we observed a desalting effect for small surface-to-surface distances $d < 1.5$ nm, i.e., salt ions to be completely expelled from the still hydrated slab. In the canonical ensemble the picture was very different. Moderate salt supersaturations induced the formation of a critical cluster in the middle of the slab and subsequent cluster growth led to a crystal arranged in sheets parallel to the surfaces. For small values of d ($\lesssim 2$ nm), fast crystallization was inhibited and the salt remained dissolved even at high supersaturations.
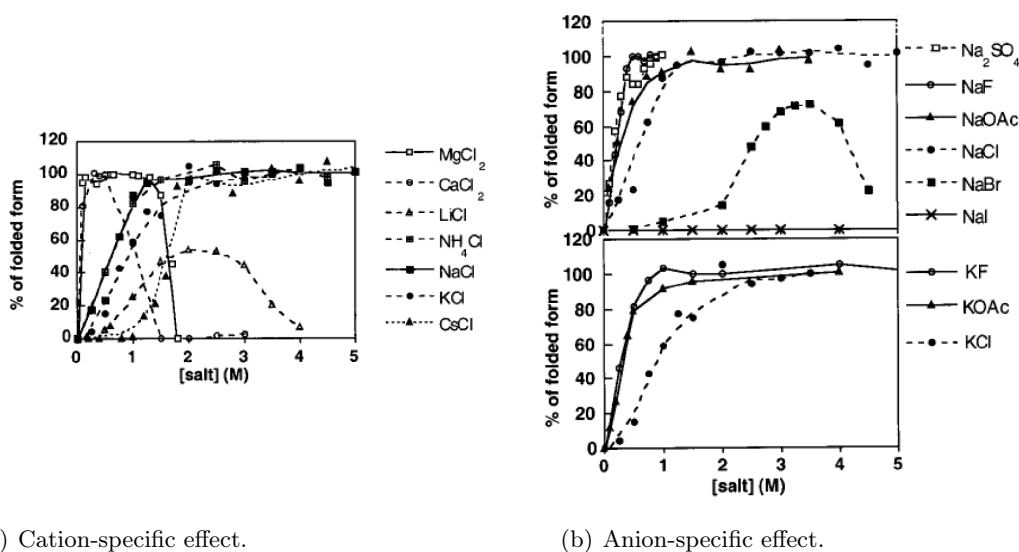
(a) Cation-specific effect.   (b) Anion-specific effect.

Figure 7.1.: *Apparent stability of halophilic malate dehydrogenase (MaIDH) immersed in a variety of electrolytes, depicted as a percentage of MaIDH found in its native folded form, plotted versus salt concentration. The specific effect of different cations (fig. 7.1(a)) and anions (fig. 7.1(b)) is shown separately by keeping the other ion constant. Fluorescence and residual activity measurements are carried out at $T = 4°C$ and pH 8 after an 24h incubation period. The case of MaIDH immersed in a 4M NaCl electrolyte is used as a reference point for 100% of the protein in folded form. Figure taken from ref. [200].*

The results in this chapter are a first step towards a better understanding of salt weathering on a molecular level. Room for improvement is vast. Future research should include not only hydrophilic surfaces but especially other salt types, such as sodium sulfate that is experimentally known to cause considerable more damage due to a higher crystallization pressure [82]. How these complex to model salts [201] can efficiently be included remains to be seen.

This thesis serves as a stepping stone for future investigations. The understanding of protein stabilization at high salt concentrations is of high biological relevance. For instance, the salt-specific stability of halophilic (salt-loving) proteins, that require high salt concentrations for stability and activity [202–204], is not understood on a molecular level. Fig. 7.1 depicts stability measurements of halophilic malate dehydrogenase (MaIDH) for a series of salts. The curves exhibit a marked salt dependency, even changing the cation or anion can significantly alter the shape of the protein stability curve. So far, we focused on static properties. It would be interesting to analyze non-equilibrium effects, such as applying a shearing force on the surfaces, as has been done in previous work for a slab-water system [205]. The investigation of multivalent ions can also prove to be very rewarding. In this realm, the strong ionic denaturant guanidinium (or the salt guanidinium chloride) is of interest in protein stability studies [206].

Summing up, we highlighted that ion-specific effects at non-vanishing salt concentrations are significant and can be tackled with a range of theoretical tools beyond the mean field level. We hope that our results lead to further refinement of presented methods. These methods are crucial in order to improve the accuracy of biochemical simulations of macromolecular systems.

Appendix A

Debye-Hückel Limiting Laws

In order to derive eq. (3.43), we start with eq. (3.37):

$$\phi(\rho) = 1 - \frac{\pi}{3}\rho \sum_{i,j=+,-} \int g_{ij}(r;\rho)\, r^3\, \frac{\mathrm{d}\beta V_{ij}^{\mathrm{eff}}(r)}{\mathrm{d}r}\mathrm{d}r. \tag{A.1}$$

The pair potential, and the pair force accordingly, as well as the rdf in the limit of infinite dilution is given by the DH terms

$$\beta w_{ij}(r) = \frac{\beta z_i z_j e^2}{4\pi\epsilon_0\epsilon r} = z_i z_j \frac{\lambda_{\mathrm{B}}}{r}$$

$$\frac{\mathrm{d}\beta w_{ij}(r)}{\mathrm{d}r} = -z_i z_j \frac{\lambda_{\mathrm{B}}}{r^2}$$

$$g_{ij}(r) = -\frac{z_i z_j \lambda_{\mathrm{B}}}{r}\exp(-\kappa r) + 1 = h_{ij}(r) + 1, \tag{A.2}$$

where $h_{ij}(r)$ is the pair correlation function. The osmotic coefficient in the DH limit is given by:

$$\phi_{\mathrm{DH}}(\rho) = 1 - \frac{\pi}{3}\rho \sum_{i,j=+,-} \int h_{ij}(r)\, r^3\, \frac{\mathrm{d}\beta w_{ij}(r)}{\mathrm{d}r}\mathrm{d}r, \tag{A.3}$$

where we inserted $h_{ij}(r)$ instead of $g_{ij}(r)$ due to electrostatic cancellation. Inserting and summing up the DH-terms for cation-anion (yielding a factor 2 due to symmetry), cation-cation and anion-anion terms leads to

$$\phi_{\mathrm{DH}}(\rho) = 1 - \frac{4\pi}{3}\rho\lambda_{\mathrm{B}}^2 \int_0^\infty \exp(-\kappa r)\mathrm{d}r$$

$$= 1 + \frac{4\pi}{3}\rho\lambda_{\mathrm{B}}^2 \frac{1}{\kappa} \left|\exp(-\kappa r)\right|_0^\infty$$

$$= \left[1 - \frac{\kappa^3}{48\,\pi\,\rho}\right], \tag{A.4}$$

where, in the last equation we inserted

$$\lambda_{\mathrm{B}}^2 = \frac{\kappa^4}{64\pi^2\rho^2}. \tag{A.5}$$

Inserting the DH limit of the osmotic coefficient ϕ_{DH} into the definition of the osmotic pressure Π_{DH} (3.30) leads to

$$\Pi_{\mathrm{DH}} = k_{\mathrm{B}}T\phi_{\mathrm{DH}}(\rho)2\rho$$

$$= 2\rho k_{\mathrm{B}}T \left[1 - \frac{\kappa^3(\rho)}{48\pi\rho}\right]. \tag{A.6}$$

Taking the first derivative with respect to ρ yields

$$\frac{\partial\Pi_{\mathrm{DH}}}{\partial\rho} = 2k_{\mathrm{B}}T \left[1 - \frac{\kappa^3(\rho)}{48\pi\rho}\right] + 2\rho k_{\mathrm{B}}T \frac{\partial}{\partial\rho}\left[1 - \frac{\kappa^3(\rho)}{48\pi\rho}\right]. \tag{A.7}$$

With the help of the expression

$$\frac{\partial\kappa(\rho)}{\partial\rho} = \frac{\partial}{\partial\rho}\sqrt{8\pi\lambda_{\mathrm{B}}\rho} = \frac{1}{2}\sqrt{\frac{8\pi\lambda_{\mathrm{B}}\rho}{\rho^2}} = \frac{1}{2}\frac{\kappa(\rho)}{\rho} \tag{A.8}$$

one easily finds

$$\frac{\partial\Pi_{\mathrm{DH}}}{\partial\rho} = 2k_{\mathrm{B}}T \left[1 - \frac{\kappa^3(\rho)}{48\pi\rho}\right] + 2\rho k_{\mathrm{B}}T \left[-\frac{\kappa^3(\rho)}{96\pi\rho^2}\right] = 2k_{\mathrm{B}}T \left(1 - \frac{\kappa^3(\rho)}{32\pi\rho}\right)$$

$$= 2k_{\mathrm{B}}T \left(1 - \frac{\kappa(\rho)\lambda_{\mathrm{B}}(0)}{4}\right), \tag{A.9}$$

where we used $\kappa^3(\rho) = 8\pi\lambda_{\mathrm{B}}(0)\rho\kappa^2(\rho)$ in the last expression.

Multiplying with ρ, taking the inverse, and using $\chi_T = \left(\rho\frac{\partial\Pi}{\partial\rho}\right)^{-1}$ finally yields:

$$2\rho k_{\mathrm{B}}T \left(\rho\frac{\partial\Pi_{\mathrm{DH}}}{\partial\rho}\right)^{-1} = 2\rho k_{\mathrm{B}}T\chi_{\mathrm{DH}} = \left(1 - \frac{\kappa(\rho)\lambda_{\mathrm{B}}(0)}{4}\right)^{-1}. \tag{A.10}$$

Derivation of $C_n(r)$

We start the derivation of the $C_n(r)$ terms of the rhs of eq. (3.68) with the lhs of eq. (3.68):

$$\int_0^1 \mathrm{d}\alpha \sum_{n=1}^\infty \frac{1}{n!}\left(-z_i z_j \frac{\lambda_\mathrm{B}}{r}\right)^n \alpha^n \exp(-n\sqrt{\alpha}\kappa r). \tag{B.1}$$

Introducing the terms

$$\begin{aligned}
a_n(r) &= \frac{1}{n!}(-z_i z_j \lambda_\mathrm{B}/r)^n \\
\Omega(r) &= -\kappa r \\
X &= \sqrt{\alpha}
\end{aligned} \tag{B.2}$$

we simplify (B.1) to

$$= 2\int_0^1 \mathrm{d}X \sum_{n=1}^\infty a_n X^{2n+1}\exp(n\Omega X) = 2\sum_{n=1}^\infty a_n \int_0^1 \mathrm{d}X\, X^{2n+1}\exp(n\Omega X) \tag{B.3}$$

At this point we make use of the following expression [207]:

$$\int x^n e^{ax}\mathrm{d}x = \frac{1}{a}x^n e^{ax} - \frac{n}{a}\int x^{n-1}e^{ax}\mathrm{d}x. \tag{B.4}$$

Repeated integration of (B.3) leads to

$$
= 2 \sum_{n=1}^{\infty} a_n \left[\left| \frac{1}{n\Omega} X^{2n+1} e^{n\Omega X} \right|_0^1 - \frac{2n+1}{n\Omega} \int_0^1 X^{2n} e^{n\Omega X} \mathrm{d}X \right]
$$

$$
= 2 \sum_{n=1}^{\infty} a_n \left[\frac{e^{n\Omega}}{n\Omega} - \frac{(2n+1)}{(n\Omega)^2} e^{n\Omega} + \frac{(2n+1)(2n)}{(n\Omega)^3} e^{n\Omega} \right.
$$
$$
\left. - \frac{(2n+1)(2n)(2n-1)}{(n\Omega)^3} \int_0^1 X^{2n-2} e^{n\Omega X} \mathrm{d}X \right] \tag{B.5}
$$

By carrying out all $2n+1$ integrations we arrive at

$$
= 2 \sum_{n=1}^{\infty} a_n \left[\frac{e^{n\Omega}}{n\Omega} - \frac{(2n+1)}{(n\Omega)^2} e^{n\Omega} + \frac{(2n+1)(2n)}{(n\Omega)^3} e^{n\Omega} - \dots \right.
$$
$$
+ \frac{(2n+1)(2n)\dots k}{(n\Omega)^{(2n+1)-k+2}} e^{n\Omega} - \dots \tag{B.6}
$$
$$
\left. + \frac{(2n+1)(2n)\dots(3)(2)}{(n\Omega)^{2n}} \int_0^1 X e^{n\Omega X} \mathrm{d}X \right].
$$

With

$$
\int_0^1 X e^{n\Omega X} \mathrm{d}X = \frac{n\Omega - 1}{(n\Omega)^2} e^{n\Omega} + \frac{1}{(n\Omega)^2}, \tag{B.7}
$$

inserting back (B.2), and by merging the terms in (B.6) into a sum, one finally arrives at

$$
\int_0^1 \mathrm{d}\alpha \sum_{n=1}^{\infty} \frac{1}{n!} \left(-z_i z_j \frac{\lambda_{\mathrm{B}}}{r} \right)^n \alpha^n \exp(-n\sqrt{\alpha}\kappa r)
$$
$$
= 2 \sum_{n=1}^{\infty} \frac{1}{n!} (-z_i z_j \lambda_{\mathrm{B}}/r)^n \frac{(2n+1)!}{(n\kappa r)^{2n+2}} \left(1 - e^{-n\kappa r} \sum_{m=0}^{2n+1} \frac{(n\kappa r)^m}{m!} \right) \tag{B.8}
$$
$$
= 2 \sum_{n=1}^{\infty} a_n(r) C_n(r),
$$

with

$$
C_n(r) = \frac{(2n+1)!}{(n\kappa r)^{2n+2}} \left(1 - e^{-n\kappa r} \sum_{m=0}^{2n+1} \frac{(n\kappa r)^m}{m!} \right) \tag{B.9}
$$

List of Figures

List of Tables

List of Publications

This thesis is based on the following publications:

- I. Kalcher and J. Dzubiella. Structure-thermodynamics relation of electrolyte solutions. *J. Chem. Phys.*, 130:134507, 2009
  URL: http://jcp.aip.org/resource/1/jcpsa6/v130/i13/p134507_s1

- I. Kalcher, D. Horinek, R. R. Netz, and J. Dzubiella. Ion specific correlations in bulk and at biointerfaces. *J. Phys. Condens. Matter*, 21:424108, 2009
  URL: http://iopscience.iop.org/0953-8984/21/42/424108

- L. Vrbka, M. Lund, I. Kalcher, J. Dzubiella, R. R. Netz, and W. Kunz. Ion-specific thermodynamics of multicomponent electrolytes: A hybrid HNC/MD approach. *J. Chem. Phys.*, 131:154109, 2009
  URL: http://jcp.aip.org/resource/1/jcpsa6/v131/i15/p154109_s1

- J. Dzubiella, M. Fyta, D. Horinek, I. Kalcher, R. R. Netz, and N. Schwierz. Ion-specificity: From solvation thermodynamics to molecular simulations and back. In W. Kunz, *Ion Specific Effects*, World Scientific, Singapore, p231-267, 2010

- M. Fyta, I. Kalcher, J. Dzubiella, L. Vrbka, and R. R. Netz. Ionic force field optimization based on single-ion and ion-pair solvation properties. *J. Chem. Phys.*, 132:024911, 2010
  URL: http://jcp.aip.org/resource/1/jcpsa6/v132/i2/p024911_s1

- I. Kalcher, J. C. F. Schulz, and J. Dzubiella. Ion-specific excluded-volume correlations and solvation forces. *Phys. Rev. Lett.*, 104:097802, 2010
  URL: http://prl.aps.org/abstract/PRL/v104/i9/e097802

- Y. von Hansen, I. Kalcher, and J. Dzubiella. Ion specificity in alpha-helical folding kinetics. *J. Phys. Chem. B*, 114:13815, 2010
  URL: http://pubs.acs.org/doi/full/10.1021/jp107495f

- I. Kalcher, J. C. F. Schulz, and J. Dzubiella. Electrolytes in a nanometer slab-confinement: Ion-specific structure and solvation forces. *J. Chem. Phys.*, 133:164511, 2010
  URL: http://jcp.aip.org/resource/1/jcpsa6/v133/i16/p164511_s1

- I. Kalcher and J. Dzubiella. Crystallization structure in bulk and in a nanometer slab-confinement: An MD study for NaCl. in preparation

Bibliography

[1] B. Alberts, A. Johnson, J. Lewis, M. Raff, K. Roberts, and P. Walter. *Molecular Biology of the Cell*. Garland Science, New York, 2002.

[2] R. A. Robinson and R. H. Stokes. *Electrolyte Solutions*. Dover Publications Inc., Mineola,NY, 2nd edition, 2002.

[3] W. Kunz. *Specific Ion Effects*. World Scientific, Singapore, 2010.

[4] P. Jungwirth and D. J. Tobias. Specific ion effects at the air/water interface. *Chem. Rev. (Washington, D.C.)*, 106:1259, 2006.

[5] D. J. Tobias and J. C. Hemminger. Chemistry-getting specific about specific ion effects. *Science*, 319:1197, 2008.

[6] R. L. Baldwin. How hofmeister ion interactions affect protein stability. *Biophys. J.*, 71:2056, 1996.

[7] J. Dzubiella. Salt-specific stability and denaturation of a short salt-bridge-forming alpha-helix. *J. Am. Chem. Soc.*, 130:14000, 2008.

[8] W. Kunz. Specific ion effects in colloidal and biological systems. *Curr. Opin. Colloid Interface Sci.*, 15:34, 2010.

[9] W. Kunz, P. Lo Nostro, and B. W. Ninham. The present state of affairs with hofmeister effects. *Curr. Opin. Colloid Interface Sci.*, 9:1, 2004.

[10] R. A. Robinson and R. H. Stokes. Tables of osmotic and activity coefficients of electrolytes in aqueous solution at 25 c. *Trans. Faraday Soc.*, 45:612, 1949.

[11] P. Debye and E. Hückel. The theory of electrolytes i. the lowering of the freezing point and related occurrences. *Phys. Z.*, 24:185, 1923.

[12] J. M. G. Barthel, H. Krienke, and W. Kunz. *Physical Chemistry of Electrolyte Solutions: Modern Aspects*. Springer/Steinkopff, Berlin,Darmstadt, 1998.

[13] J. E. Enderby and G. W. Neilson. The structure of electrolyte-solutions. *Rep. Prog. Phys.*, 44:593, 1981.

[14] S. Rajamani, T. Ghosh, and S. Garde. Size dependent ion hydration, its asymmetry, and convergence to macroscopic behavior. *J. Chem. Phys.*, 120:4457, 2004.

[15] A. K. Soper and K. Weckström. Ion solvation and water structure in potassium halide aqueous solutions. *Biophys. Chem.*, 124:180, 2006.

[16] K. D. Collins. Charge density-dependent strength of hydration and biological structure. *Biophys. J.*, 72:65, 1997.

[17] K. D. Collins. Ions from the hofmeister series and osmolytes: effects on proteins in solution and in the crystallization process. *Methods*, 34:300, 2004.

[18] L. Vrbka, B. Jagoda-Cwiklik, R. Vácha, and P. Jungwirth. Quantification and rationalization of the higher affinity of sodium over potassium to protein surfaces. *Proc. Natl. Acad. Sci. U.S.A.*, 103:15440, 2006.

[19] B. Jagoda-Cwiklik, R. Vácha, M. Lund, M. Srebro, and P. Jungwirth. Ion pairing as a possible clue for discriminating between sodium and potassium in biological and other complex environments. *J. Phys. Chem. B*, 111:14077, 2007.

[20] M. Lund, R. Vácha, and P. Jungwirth. Specific ion binding to macromolecules: effects of hydrophobicity and ion pairing. *Langmuir*, 24:3387, 2008.

[21] J. S. Uejio, C. P. Schwartz, A. M. Duffin, W. S. Drisdell, R. C. Cohen, and R. J. Saykally. Characterization of selective binding of alkali cations with carboxylate by x-ray absorption spectroscopy of liquid microjets. *Proc. Natl. Acad. Sci. U.S.A.*, 105:6809, 2008.

[22] M. Karplus and J. A. McCammon. Molecular dynamics simulations of biomolecules. *Nat. Struct. Mol. Biol.*, 9:646, 2002.

[23] S.-B. Zhu and G. W. Robinson. Molecular-dynamics computer-simulation of an aqueous nacl solution-structure. *J. Chem. Phys.*, 97:4336, 1992.

[24] A. P. Lyubartsev and A. Laaksonen. Calculation of effective interaction potentials from radial-distribution functions - a reverse monte carlo approach. *Phys. Rev. E*, 52:3730, 1995.

[25] A. P. Lyubartsev and A. Laaksonen. Osmotic and activity coefficients from effective potentials for hydrated ions. *Phys. Rev. E*, 55:5689, 1997.

[26] H. Uchida and M. Matsuoka. Molecular dynamics simulation of solution structure and dynamics of aqueous sodium chloride solutions from dilute to supersaturated concentration. *Fluid Phase Equilib.*, 219:49, 2004.

[27] B. Hess, C. Holm, and N. van der Vegt. Modeling multibody effects in ionic solutions with a concentration dependent dielectric permittivity. *Phys. Rev. Lett.*, 96:147801, 2006.

[28] B. Hess, C. Holm, and N. van der Vegt. Osmotic coefficients of atomistic nacl (aq) force fields. *J. Chem. Phys.*, 124:164509, 2006.

[29] S. Gavryushov. Effective interaction potentials for alkali and alkaline earth metal ions in spc/e water and polarization model of hydrated ions. *J. Phys. Chem. B*, 110:10888, 2006.

[30] S. Gavryushov and P. Linse. Effective interaction potentials for alkali and alkaline earth metal ions in spc/e water and prediction of mean ion activity coefficients. *J. Phys. Chem. B*, 110:10878, 2006.

[31] P. S. Ramanathan and H. L. Friedman. Study of a refined model for aqueous 1-1 electrolytes. *J. Chem. Phys.*, 54:1086, 1971.

[32] B. M. Pettitt and P. J. Rossky. Alkali-halides in water - ion solvent correlations and ion ion potentials of mean force at infinite dilution. *J. Chem. Phys.*, 84:5836, 1986.

[33] L. X. Dang, B. M. Pettitt, and P. J. Rossky. On the correlation between like ion-pairs in water. *J. Chem. Phys.*, 96:4046, 1992.

[34] M. Patra and M. Karttunen. Systematic comparison of force fields for microscopic simulations of nacl in aqueous solutions: diffusion, free energy of hydration, and structural properties. *J. Comput. Chem.*, 25:678, 2004.

[35] I. S. Joung and T. E. Cheatham. Determination of alkali and halide monovalent ion parameters for use in explicitly solvated biomolecular simulations. *J. Phys. Chem. B*, 112:9020, 2008.

[36] D. Horinek, S. I. Mamatkulov, and R. R. Netz. Rational design of ion force fields based on thermodynamic solvation properties. *J. Chem. Phys.*, 130:124507, 2009.

[37] J. E. Mayer. *Equilibrium Statistical Mechanics*. Pergamon, Oxford, 1968.

[38] W. G. McMillan and J. E. Mayer. The statistical thermodynamics of multicomponent systems. *J. Chem. Phys.*, 13:276, 1945.

[39] J. G. Kirkwood and F. P. Buff. The statistical mechanical theory of solutions .1. *J. Chem. Phys.*, 19:774, 1951.

[40] J.-P. Hansen and I. R. McDonald. *Theory of Simple Liquids*. Academic Press, New York, 3rd edition, 2005.

[41] J. C. Rasaiah and H. L. Friedman. Integral equation methods in computation of equilibrium properties of ionic solutions. *J. Chem. Phys.*, 48:2742, 1968.

[42] G. N. Patey and J. P. Valleau. Monte carlo method for obtaining interionic potential of mean force in ionic solution. *J. Chem. Phys.*, 63:2334, 1975.

[43] G. N. Patey and S. L. Carnie. Theoretical results for aqueous-electrolytes - ion-ion potentials of mean force and the solute-dependent dielectric-constant. *J. Chem. Phys.*, 78:5183, 1983.

[44] A. P. Lyubartsev and S. Marčelja. Evaluation of effective ion-ion potentials in aqueous electrolytes. *Phys. Rev. E*, 65:041202, 2002.

[45] P. J. Lenart, A. Jusufi, and A. Z. Panagiotopoulos. Effective potentials for 1:1 electrolyte solutions incorporating dielectric saturation and repulsive hydration. *J. Chem. Phys.*, 126:044509, 2007.

[46] B. Hess and N. F. A. van der Vegt. Solvent-averaged potentials for alkali-, earth alkali-, and alkylammonium halide aqueous solutions. *J. Chem. Phys.*, 127:234508, 2007.

[47] S. A. Adelman. Effective direct correlation-function - approach to theory of liquid solutions. *J. Chem. Phys.*, 64:724, 1976.

[48] S. A. Adelman. Effective direct correlation-function, an approach to theory of liquid solutions - new definition of effective solute potential. *Chem. Phys. Lett.*, 38:567, 1976.

[49] J. L. Martin, J. L. Gómez-Estévez, and M. Canales. Simple statistical-mechanics of electrolytes with a concentration dependent dielectric constant .1. the pressure equation. *J. Solution Chem.*, 16:87, 1987.

[50] S. Weerasinghe and P. E. Smith. A kirkwood-buff derived force field for sodium chloride in water. *J. Chem. Phys.*, 119:11342, 2003.

[51] Y. Luo and B. Roux. Simulation of osmotic pressure in concentrated aqueous salt solutions. *J. Phys. Chem. Lett.*, 1:183, 2010.

[52] Y. V. Kalyuzhnyi, V. Vlachy, and K. A. Dill. Aqueous alkali halide solutions: can osmotic coefficients be explained on the basis of the ionic sizes alone ? *Phys. Chem. Chem. Phys.*, 12:6260, 2010.

[53] M. Fyta, I. Kalcher, J. Dzubiella, L. Vrbka, and R. R. Netz. Ionic force field optimization based on single-ion and ion-pair solvation properties. *J. Chem. Phys.*, 132:024911, 2010.

[54] J. N. Israelachvili. *Intermolecular and Surface Forces*. Elsevier, Amsterdam, 1992.

[55] M. Boström, D. R. M. Williams, and B. W. Ninham. Specific ion effects: why dlvo theory fails for biology and colloid systems. *Phys. Rev. Lett.*, 87:168103, 2001.

[56] D. Horinek, A. Herz, L. Vrbka, F. Sedlmeier, S. I. Mamatkulov, and R. R. Netz. Specific ion adsorption at the air/water interface: the role of hydrophobic solvation. *Chem. Phys. Lett.*, 479:173, 2009.

[57] N. Schwierz, D. Horinek, and R. R. Netz. Reversed anionic hofmeister series: the interplay of surface charge and surface polarity. *Langmuir*, 26:7370, 2010.

[58] R. M. Pashley and J. N. Israelachvili. Molecular layering of water in thin-films between mica surfaces and its relation to hydration forces. *J. Colloid Interface Sci.*, 101:511, 1984.

[59] M. Colic, M. L. Fisher, and G. V. Franks. Influence of ion size on short-range repulsive forces between silica surfaces. *Langmuir*, 14:6107, 1998.

[60] M. Dishon, O. Zohar, and U. Sivan. From repulsion to attraction and back to repulsion: the effect of nacl, kcl, and cscl on the force between silica surfaces in aqueous solution. *Langmuir*, 25:2831, 2009.

[61] T. López-León, P. M. Gea-Jódar, D. Bastos-González, and J. L. Ortega-Vinuesa. Hofmeister effects in the restabilization of igg-latex particles: testing ruckenstein's theory. *Langmuir*, 21:87, 2005.

[62] A.-C. J. H. Johnson, P. Greenwood, M. Hagström, Z. Abbas, and S. Wall. Aggregation of nanosized colloidal silica in the presence of various alkali cations investigated by the electrospray technique. *Langmuir*, 24:12798, 2008.

[63] A. Y. Huang and J. C. Berg. High-salt stabilization of laponite clay particles. *J. Colloid Interface Sci.*, 296:159, 2006.

[64] T. Missana and A. Adell. On the applicability of dlvo theory to the prediction of clay colloids stability. *J. Colloid Interface Sci.*, 230:150, 2000.

[65] R. Kjellander. Intricate coupling between ion-ion and ion-surface correlations in double layers as illustrated by charge inversion-combined effects of strong coulomb correlations and excluded-voume. *J. Phys.: Condens. Matter*, 21:424101, 2009.

[66] P. G. Bolhuis, T. Åkesson, and B. Jönsson. Attractive double-layer forces from hard-core correlations. *J. Chem. Phys.*, 98:8096, 1993.

[67] J. Lyklema. Quest for ion-ion correlations in electric double layers and overcharging phenomena. *Adv. Colloid Interface Sci.*, 147-48:205, 2009.

[68] S. Leikin, V. A. Parsegian, D. C. Rau, and R. P. Rand. Hydration forces. *Annu. Rev. Phys. Chem.*, 44:369, 1993.

[69] M. Lund and P. Jungwirth. Ion specific protein assembly and hydrophobic surface forces. *Phys. Rev. Lett.*, 100:258105, 2008.

[70] M. Lund, L. Vrbka, and P. Jungwirth. Specific ion binding to nonpolar surface patches of proteins. *J. Am. Chem. Soc.*, 130:11582, 2008.

[71] A. McPherson. *Introduction to Macromolecular Crystallography*. John Wiley, Hoboken, New Jersey, 2009.

[72] W. C. K. Poon and D. Andelman. *Soft Condensed Matter Physics in Molecular and Cell Biology*. Taylor and Francis, London, 2006.

[73] J.-P. Hansen and H. Löwen. Effective interactions between electric double layers. *Annu. Rev. Phys. Chem.*, 51:209, 2000.

[74] R. Messina. Electrostatics in soft matter. *J. Phys.: Condens. Matter*, 21:113102, 2009.

[75] Y. Levin. Electrostatic correlations: from plasma to biology. *Rep. Prog. Phys.*, 65:1577, 2002.

[76] J. Forsman. A simple correlation-corrected poisson-boltzmann theory. *J. Phys. Chem. B*, 108:9236, 2004.

[77] J. Forsman. Density functional theories of surface interactions in salt solutions. *J. Chem. Phys.*, 130:064901, 2009.

[78] C. W. Correns and W. Steinborn. Experiments for measuring and explaining the so-called crystallization strength. *Z. Kristallogr.*, 101:117, 1939.

[79] R. J. Flatt, M. Steiger, and G. W. Scherer. A commented translation of the paper by c. w. correns and w. steinborn on crystallization pressure. *Environ. Geol.*, 52:187, 2007.

[80] C. Rodriguez-Navarro and E. Doehne. Salt weathering: influence of evaporation rate, supersaturation and crystallization pattern. *Earth Surf. Process. Landforms*, 24:191, 1999.

[81] R. M. Espinosa-Marzal and G. W. Scherer. Advances in understanding damage by salt crystallization. *Acc. Chem. Res.*, 43:897, 2010.

[82] N. Shahidzadeh-Bonn, S. Rafaï, D. Bonn, and G. Wegdam. Salt crystallization during evaporation: impact of interfacial properties. *Langmuir*, 24:8599, 2008.

[83] N. Shahidzadeh-Bonn, J. Desarnaud, F. Bertrand, X. Chateau, and D. Bonn. Damage in porous media due to salt crystallization. *Phys. Rev. E*, 81:066110, 2010.

[84] G. W. Scherer. Crystallization in pores. *Cem. Concr. Res.*, 29:1347, 1999.

[85] G. W. Scherer. Stress from crystallization of salt. *Cem. Concr. Res.*, 34:1613, 2004.

[86] M. Steiger. Crystal growth in porous materials-i: the crystallization pressure of large crystals. *J. Cryst. Growth*, 282:455, 2005.

[87] M. Steiger. Crystal growth in porous materials-ii: influence of crystal size on the crystallization pressure. *J. Cryst. Growth*, 282:470, 2005.

[88] D. Benavente, M. A. García del Cura, J. García-Guinea, S. Sánchez-Moral, and S. Ordó nez. Role of pore structure in salt crystallization in unsaturated porous stone. *J. Cryst. Growth*, 260:532, 2004.

[89] R. J. Flatt. Salt damage in porous materials: how high supersaturations are generated. *J. Cryst. Growth*, 242:435, 2002.

[90] R. M. Espinosa, L. Franke, and G. Deckelmann. Phase changes of salts in porous materials: crystallization, hydration and deliquescence. *J. Constr. Build. Mater.*, 22:1758, 2008.

[91] M. Angeli, J-P Bigas, D. Benavente, B. Menéndez, R. Hébert, and C. David. Salt crystallization in pores: quantification and estimation of damage. *Environ. Geol.*, 52:205, 2007.

[92] L. A. Rijniers, H. P. Huinink, L. Pel, and K. Kopinga. Experimental evidence of crystallization pressure inside porous media. *Phys. Rev. Lett.*, 94:075503, 2005.

[93] M. Gomez-Heras and R. Fort. Patterns of halite (nacl) crystallization in building stone conditioned by laboratory heating regimes. *Environ. Geol.*, 52:259, 2007.

[94] M. Miyahara and K. E. Gubbins. Freezing/melting phenomena for lennard-jones methane in slit pores: a monte carlo study. *J. Chem. Phys.*, 106:2865, 1997.

[95] L. D. Gelb, K. E. Gubbins, R. Radhakrishnan, and M. Sliwinska-Bartkowiak. Phase separation in confined systems. *Rep. Prog. Phys.*, 62:1573, 1999.

[96] C. Alba-Simionesco, B. Coasne, G. Dosseh, G. Dudziak, K. E. Gubbins, R. Radhakrishnan, and M. Sliwinska-Bartkowiak. Effects of confinement on freezing and melting. *J. Phys.:Condens. Matter*, 18:R15, 2006.

[97] R. Radhakrishnan, K. E. Gubbins, and M. Sliwinska-Bartkowiak. Effect of the fluid-wall interaction on freezing of confined fluids: towards the development of a global phase diagram. *J. Chem. Phys.*, 112:11048, 2000.

[98] R. Radhakrishnan, K. E. Gubbins, and M. Sliwinska-Bartkowiak. Global phase diagrams for freezing in porous media. *J. Chem. Phys.*, 116:1147, 2002.

[99] L. G. Cámara and F. Bresme. Molecular dynamics simulation of crystallization under confinement at triple point conditions. *J. Chem. Phys.*, 119:2792, 2003.

[100] F. Bresme and L. G. Cámara. Computer simulation studies of crystallization under confinement conditions. *Chem. Geol.*, 230:197, 2006.

[101] M. Kittner and S. H. L. Klapp. Screening effects on structure and diffusion in confined charged colloids. *J. Chem. Phys.*, 126:154902, 2007.

[102] S. Grandner and S. H. L. Klapp. Freezing of charged colloids in slit pores. *J. Chem. Phys.*, 129:244703, 2008.

[103] V. G. Baidakov, A. O. Tipeev, K. S. Bobrov, and G. V. Ionov. Crystal nucleation rate isotherms in lennard-jones liquids. *J. Chem. Phys.*, 132:234505, 2010.

[104] S. Auer and D. Frenkel. Prediction of absolute crystal-nucleation rate in hard-sphere colloids. *Nature*, 409:1020, 2001.

[105] D. Zahn. Atomistic mechanism of nacl nucleation from an aqueous solution. *Phys. Rev. Lett.*, 92:040801, 2004.

[106] C. Dellago and P. Bolhuis. Transition path sampling and other advanced simulation techniques for rare events. *Adv. Polym. Sci.*, 221:167, 2009.

[107] M. Mucha and P. Jungwirth. Salt crystallization from an evaporating aqueous solution by molecular dynamics simulations. *J. Phys. Chem. B*, 107:8271, 2003.

[108] A. Malani, K. G. Ayappa, and S. Murad. Effect of confinement on the hydration and solubility of nacl in water. *Chem. Phys. Lett.*, 431:88, 2006.

[109] D. Frenkel and B. Smit. *Understanding Molecular Simulation: From Algorithms to Applications*. Academic Press, New York, 2nd edition, 2002.

[110] M. P. Allen and D. J. Tildesley. *Computer Simulations of Liquids*. Oxford University Press, Oxford, 1989.

[111] D. van der Spoel, E. Lindhal, B. Hess, G. Groenhof, A. E. Mark, and H. J. C. Berendsen. Gromacs: Fast, flexible, and free. *J. Comput. Chem.*, 26:1701, 2005.

[112] E. Lindhal, B. Hess, and D. van der Spoel. Gromacs 3.0: a package for molecular simulation and trajectory analysis. *J. Mol. Mod.*, 7:306, 2001.

[113] H. J. C. Berendsen, J. P. M. Postma, W. F. van Gunsteren, A. DiNola, and J. R. Haak. Molecular-dynamics with coupling to an external bath. *J. Chem. Phys.*, 81:3684, 1984.

[114] H. J. C. Berendsen, J. R. Grigera, and T. P. Straatsma. The missing term in effective pair potentials. *J. Phys. Chem.*, 91:6269, 1987.

[115] U. Essmann, L. Perera, M. L. Berkowitz, T. Darden, H. Lee, and L. G. Pedersen. A smooth particle mesh ewald method. *J. Chem. Phys.*, 103:8577, 1995.

[116] L. X. Dang. Development of nonadditive intermolecular potentials using molecular-dynamics - solvation of li+ and f- ions in polarizable water. *J. Chem. Phys.*, 96:6970, 1992.

[117] L. X. Dang and B. C. Garrett. Photoelectron-spectra of the hydrated iodine anion from molecular-dynamics simulations. *J. Chem. Phys.*, 99:2972, 1993.

[118] L. X. Dang. Mechanism and thermodynamics of ion selectivity in aqueous-solutions of 18-crown-6 ether - a molecular-dynamics study. *J. Am. Chem. Soc.*, 117:6954, 1995.

[119] L. X. Dang. Fluoride-fluoride association in water from molecular-dynamics simulations. *Chem. Phys. Lett.*, 200:21, 1992.

[120] R. M. Lynden-Bell and J. C. Rasaiah. From hydrophobic to hydrophilic behaviour: a simulation study of solvation entropy and free energy of simple solutes. *J. Chem. Phys.*, 107:1981, 1997.

[121] S. Koneshan, J. C. Rasaiah, R. M. Lynden-Bell, and S. H. Lee. Solvent structure, dynamics, and ion mobility in aqueous solutions at 25 degrees c. *J. Phys. Chem. B*, 102:4193, 1998.

[122] J. Åqvist. Ion water interaction potentials derived from free-energy perturbation simulations. *J. Phys. Chem.*, 94:8021, 1990.

[123] P. Auffinger, T. E. Cheatham, and A. C. Vaiana. Spontaneous formation of kcl aggregates in biomolecular simulations: a force field issue? *J. Chem. Theory Comput.*, 3:1851, 2007.

[124] M. Parrinello and A. Rahman. Polymorphic transitions in single-crystals - a new molecular-dynamics method. *J. Appl. Phys.*, 52:7182, 1981.

[125] S. Nosé and M. L. Klein. Constant pressure molecular-dynamics for molecular-systems. *Mol. Phys.*, 50:1055, 1983.

[126] W. L. Jorgensen, D. S. Maxwell, and J. Tirado-Rives. Development and testing of the opls all-atom force field on conformational energetics and properties of organic liquids. *J. Am. Chem. Soc.*, 118:11225, 1996.

[127] J. S. Rowlinson and B. Widom. *Molecular Theory of Capillarity*. Oxford University Press, Oxford, 1982.

[128] W. Humphrey, A. Dalke, and K. Schulten. Vmd: visual molecular dynamics. *J. Molec. Graphics*, 14:33, 1996.

[129] S. Kumar, J. M. Rosenberg, D. Bouzida, R. H. Swendsen, and P. A. Kollman. The weighted-histogram analysis method for free-energy calculations on biomolecules .1. the method. *J. Comp. Chem.*, 13:1011, 1992.

[130] D. Horinek and R. R. Netz. Specific ion adsorption at hydrophobic solid surfaces. *Phys. Rev. Lett.*, 99:226104, 2007.

[131] N. Metropolis, A. W. Rosenbluth, M. N. Rosenbluth, A. H. Teller, and E. Teller. Equation of state calculations by fast computing machines. *J. Chem. Phys.*, 21:1087, 1953.

[132] Julius C. F. Schulz. Structure and phase behaviour of electrolytes in confined geometries. *Diplomarbeit*, 2010.

[133] J. Lekner. Summation of coulomb fields in computer-simulated disordered-systems. *Physica A*, 176:485, 1991.

[134] R. Sperb. An alternative to ewald sums, part 2: the coulomb potential in a periodic system. *Mol. Simul.*, 22:199, 1999.

[135] W. H. Press, S. A. Teukolsky, W. T. Vetterling, and B. P. Flannery. *Numerical Recipes in C: The Art of Scientific Computing*. Cambridge University Press, New York, 2nd edition, 1992.

[136] K. Younge, C. Christenson, A. Bohara, J. Crnkovic, and P. Saulnier. A model system for examining the radial distribution function. *Am. J. Phys.*, 72:1247, 2004.

[137] D. Chandler. *Introduction to Modern Statistical Mechanics*. Oxford University Press, Oxford, 1987.

[138] T. L. Hill. *An Introduction to Statistical Thermodynamics*. Dover Publications, New York, 1986.

[139] J. Perkyns and B. M. Pettitt. A site theory for finite concentration saline solutions. *J. Chem. Phys.*, 97:7656, 1992.

[140] P. G. Kusalik and I. M. Svishchev. The spatial structure in liquid water. *Science*, 265:1219, 1994.

[141] I. V. Khavrutskii, J. Dzubiella, and J. A. McCammon. Computing accurate potentials of mean force in electrolyte solutions with the generalized gradient-augmented harmonic fourier beads method. *J. Chem. Phys.*, 128:044106, 2008.

[142] J. G. Kirkwood. The dielectric polarization of polar liquids. *J. Chem. Phys.*, 7:911, 1939.

[143] M. Neumann. Dipole-moment fluctuation formulas in computer-simulations of polar systems. *Mol. Phys.*, 50:841, 1983.

[144] P. Kumar, S. V. Buldyrev, F. W. Starr, N. Giovambattista, and H. E. Stanley. Thermodynamics, structure, and dynamics of water confined between hydrophobic plates. *Phys. Rev. E*, 72:051503, 2005.

[145] B. Hess. Determining the shear viscosity of model liquids from molecular dynamics simulations. *J. Chem. Phys.*, 116:209, 2002.

[146] R. Zwanzig. Time-correlation functions and transport coefficients in statistical mechanics. *Annu. Rev. Phys. Chem.*, 16:67, 1965.

[147] T. Chen, B. Smit, and A. T. Bell. Are pressure fluctuation-based equilibrium methods really worse than nonequilibrium methods for calculating viscosities? *J. Chem. Phys.*, 131:246101, 2009.

[148] A. Ben-Naim. *Molecular Theory of Solutions.* Oxford University Press, Oxford, 2006.

[149] J.-L. Barrat and J.-P. Hansen. *Basic Concepts for Simple and Complex Liquids.* Cambridge University Press, Cambridge, 2003.

[150] H. Akima. A new method of interpolation and smooth curve fitting based on local procedures. *J. Assoc. Comput. Mach.*, 17:589, 1970.

[151] J. A. Barker and D. Henderson. Perturbation theory and equation of state for fluids. ii. a successful theory of liquids. *J. Chem. Phys.*, 47:4714, 1967.

[152] R. Roth, R. Evans, and A. A. Louis. Theory of asymmetric nonadditive binary hard-sphere mixtures. *Phys. Rev. E*, 64:051202, 2001.

[153] G. Pastore, P. V. Giaquinta, J. S. Thakur, and M. P. Tosi. Ionic pairing in binary liquids of charged hard-spheres with nonadditive diameters. *J. Chem. Phys.*, 84:1827, 1986.

[154] M. Dijkstra. Phase behavior of nonadditive hard-sphere mixtures. *Phys. Rev. E*, 58:7523, 1998.

[155] A. A. Louis, R. Finken, and J. P. Hansen. Crystallization and phase separation in nonadditive binary hard-sphere mixtures. *Phys. Rev. E*, 61:R1028, 2000.

[156] N. Hoffmann, F. Ebert, C. N. Likos, H. Löwen, and G. Maret. Partial clustering in binary two-dimensional colloidal suspensions. *Phys. Rev. Lett.*, 97:078301, 2006.

[157] I. Borukhov, D. Andelman, and H. Orland. Steric effects in electrolytes: a modified poisson-boltzmann equation. *Phys. Rev. Lett.*, 79:435, 1997.

[158] G. Tresset. Generalized poisson-fermi formalism for investigating size correlation effects with multiple ions. *Phys. Rev. E*, 78:061506, 2008.

[159] A. Santos, M. López de Haro, and S. B. Yuste. Equation of state of nonadditive d-dimensional hard-sphere mixtures. *J. Chem. Phys.*, 122:024514, 2005.

[160] Y. Burak and D. Andelman. Discrete aqueous solvent effects and possible attractive forces. *J. Chem. Phys.*, 114:3271, 2001.

[161] Y. Rosenfeld. Free-energy model for the inhomogeneous hard-sphere fluid mixture and density-functional theory of freezing. *Phys. Rev. Lett.*, 63:980, 1989.

[162] M. Schmidt. Rosenfeld functional for non-additive hard spheres. *J. Phys.: Condens. Matter*, 16:L351, 2004.

[163] M. Schmidt. Fundamental measure density functional theory for nonadditive hard-core mixtures: the one-dimensional case. *Phys. Rev. E*, 76:031202, 2007.

[164] R. Roth. Fundamental measure theory for hard-sphere mixtures: a review. *J. Phys.: Condens. Matter*, 22:063102, 2010.

[165] R. Kjellander, A. P. Lyubartsev, and S. Marčelja. Mcmillan-mayer theory for solvent effects in inhomogeneous systems: calculation of interaction pressure in aqueous electrical double layers. *J. Chem. Phys.*, 114:9565, 2001.

[166] S. A. Edwards and D. R. M. Williams. Double layers and interparticle forces in colloid science and biology: analytic results for the effect of ionic dispersion forces. *Phys. Rev. Lett.*, 92:248303, 2004.

[167] S. L. Carnie and D. Y. C. Chan. The statistical-mechanics of the electrical double-layer - stress tensor and contact conditions. *J. Chem. Phys.*, 74:1293, 1981.

[168] C. Schneider, M. Hanisch, B. Wedel, A. Jusufi, and M. Ballauff. in preparation.

[169] B. Hess, H. Bekker, H. J. C. Berendsen, and J. G. E. M. Fraaije. Lincs: A linear constraint solver for molecular simulations. *J. Comput. Chem.*, 18:1463, 1997.

[170] P. G. Kusalik and G. N. Patey. Theoretical results for dielectric and structural-properties of aqueous-electrolytes - the influence of ion size and charge. *J. Chem. Phys.*, 79:4468, 1983.

[171] D. Levesque, J. J. Weis, and G. N. Patey. Charged hard-spheres in dipolar hard-sphere solvents - model for electrolyte-solutions. *J. Chem. Phys.*, 72:1887, 1980.

[172] D. Levesque, J. J. Weis, and G. N. Patey. Potential of mean force for an infinitely dilute ionic solution. *Phys. Lett. A*, 66:115, 1978.

[173] A. Chandra. Static dielectric constant of aqueous electrolyte solutions: is there any dynamic contribution? *J. Chem. Phys.*, 113:902, 2000.

[174] Y.-Z. Wei, P. Chiang, and S. Sridhar. Ion size effects on the dynamic and static dielectric-properties of aqueous alkali solutions. *J. Chem. Phys.*, 96:4569, 1992.

[175] A. K. Lyashchenko and A. Y. Zasetsky. Complex dielectric permittivity and relaxation parameters of concentrated aqueous electrolyte solutions in millimeter and centimeter wavelenght ranges. *J. Mol. Liq.*, 77:61, 1998.

[176] D. V. Loginova, A. S. Lileev, and A. K. Lyashchenko. Microwave dielectric properties of aqueous solutions of potassium and cesium fluorides. *Russ. J. Phys. Chem.*, 80:1626, 2006.

[177] R. Buchner, G. T. Hefter, and J. Barthel. Dielectric-relaxation of aqueous naf and kf solutions. *J. Chem. Soc., Faraday Trans.*, 90:2475, 1994.

[178] J. M. G. Barthel, R. Buchner, and M. Münsterer. *Electrolyte Data Collection*, volume 12. DECHEMA, Frankfurt, 1995.

[179] K. Nörtemann, J. Hilland, and U. Kaatze. Dielectric properties of aqueous nacl solutions at microwave frequencies. *J. Phys. Chem. A*, 101:6864, 1997.

[180] W. Wachter, W. Kunz, R. Buchner, and G. Hefter. Is there an anionic hofmeister effect on water dynamics? dielectric spectroscopy of aqueous solutions of nabr, nai, nano3, naclo4, and nascn. *J. Phys. Chem. A*, 109:8675, 2005.

[181] M. A. Gonzalez and J. L. F. Abascal. The shear viscosity of rigid water models. *J. Chem. Phys.*, 132:096101, 2010.

[182] P. Jungwirth and D. J. Tobias. Ions at the air/water interface. *J. Phys. Chem. B*, 106:6361, 2002.

[183] A. Wynveen and F. Bresme. Properties of alkali-halide salt solutions about polarizable nanoparticle solutes for different ion models. *J. Chem. Phys.*, 133:144706, 2010.

[184] D. Antypov, M. C. Barbosa, and C. Holm. Incorporation of excluded-volume correlations into poisson-boltzmann theory. *Phys. Rev. E*, 71:061106, 2005.

[185] J. Lyklema. Overcharging, charge reversal: chemistry or physics? *Colloids Surf. A*, 291:3, 2006.

[186] R. Messina, E. González-Tovar, M. Lozada-Cassou, and C. Holm. Overcharging: the crucial role of excluded volume. *Europhys. Lett.*, 60:383, 2002.

[187] H. Langer and H. Offermann. On the solubility of sodium-chloride in water. *J. Cryst. Growth*, 60:389, 1982.

[188] T. Koishi, S. Yoo, K. Yasuoka, X. C. Zeng, T. Narumi, R. Susukita, A. Kawai, H. Furusawa, A. Suenaga, N. Okimoto, N. Futatsugi, and T. Ebisuzaki. Nanoscale hydrophobic interaction and nanobubble nucleation. *Phys. Rev. Lett.*, 93:185701, 2004.

[189] J. Dzubiella and J.-P. Hansen. Electric-field-controlled water and ion permeation of a hydrophobic nanopore. *J. Chem. Phys.*, 122:234706, 2005.

[190] X. Huang, R. Zhou, and B. J. Berne. Drying and hydrophobic collapse of paraffin plates. *J. Phys. Chem. B*, 109:3546, 2005.

[191] R. Grossier, A. Magnaldo, and S. Veesler. Ultra-fast crystallization due to confinement. *J. Cryst. Growth*, 312:487, 2010.

[192] R. Grossier and S. Veesler. Reaching one single and stable critical cluster through finite-sized systems. *Cryst. Growth Des.*, 9:1917, 2009.

[193] E. M. Winkler and P. C. Singer. Crystallization pressure of salts in stone and concrete. *Geological Society of America Bulletin*, 83:3509, 1972.

[194] C. W. Correns. Growth and dissolution of crystals under linear pressure. *Discussions of the Faraday Society*, 5:267, 1949.

[195] D. Gillespie, W. Nonner, and R. S. Eisenberg. Coupling poisson-nernst-planck and density functional theory to calculate ion flux. *J. Phys. Condens. Matter*, 14:12129, 2002.

[196] H.-X. Zhou and J. A. McCammon. The gates of ion channels and enzymes. *Trends Biochem. Sci.*, 35:179, 2010.

[197] M. I. El-Barghouthi, A. I. Saleh, A. Ghandour, R. Ghanem, and M. Zacharias. Examining the potency of suggested inhibitors for the phosphatase activity of the human soluble epoxide hydrolase by molecular dynamics simulations. *J. Mol. Struct.*, 944:97, 2010.

[198] M. G. Knepley, D. A. Karpeev, S. Davidovits, R. S. Eisenberg, and D. Gillespie. An efficient algorithm for classical density functional theory in three dimensions: ionic solutions. *J. Chem. Phys.*, 132:124101, 2010.

[199] N. A. Baker, D. Sept, S. Joseph, M. J. Holst, and J. A. McCammon. Electrostatics of nanosystems: application to microtubules and the ribosome. *Proc. Natl. Acad. Sci.*, 98:10037, 2001.

[200] C. Ebel, P. Faou, B. Kernel, and G. Zaccai. Relative role of anions and cations in the stabilization of halophilic malate dehydrogenase. *Biochemistry*, 38:9039, 1999.

[201] E. Wernersson and P. Jungwirth. Effect of water polarizability on the properties of solutions of polyvalent ions: simulations of aqueous sodium sulfate with different force fields. *J. Chem. Theory Comput.*, 6:3233, 2010.

[202] D. Madern, C. Ebel, and G. Zaccai. Halophilic adaptation of enzymes. *Extremophiles*, 4:91, 2000.

[203] M. Mevarech, F. Frolow, and L. M. Gloss. Halophilic enzymes: proteins with a grain of salt. *Biophys. Chem.*, 86:155, 2000.

[204] A. H. Elcock and J. A. McCammon. Electrostatic contributions to the stability of halophilic proteins. *J. Mol. Biol.*, 280:731, 1998.

[205] C. Sendner, D. Horinek, L. Bocquet, and R. R. Netz. Interfacial water at hydrophobic and hydrophilic surfaces: slip, viscosity, and diffusion. *Langmuir*, 25:10768, 2009.

[206] W. K. Lim, J. Rösgen, and S. W. Englander. Urea, but not guanidinium, destabilizes proteins by forming hydrogen bonds to the peptide group. *Proc. Natl. Acad. Sci.*, 106:2595, 2009.

[207] I.N. Bronstein, K. A. Semendjajew, G. Musiol, and H. Mühlig. *Taschenbuch der Mathematik*. H. Deutsch, Frankfurt am Main, 7th edition, 2008.

Acknowledgments

Ich möchte an dieser Stelle vor allem jenen danken, ohne die ich diese Arbeit nicht fertig-stellen hätte können. Dies betrifft in erster Linie meinen Betreuer Joachim "Joe"Dzubiella, welcher ständig für mich erreichbar war und mir gleichzeitig viele Freiheiten gewährte. Weiters ermöglichte er mir unsere Forschung an Universitäten in Berlin sowie in San Die-go vorzustellen was mir großen Spaß machte. Sehr herzlich bedanke ich mich bei Roland Netz an dessen Lehrstuhl T37 ich arbeiten durfte und welcher mir ermöglichte viele Men-schen kennen zu lernen und an zahlreichen Exkursionen, von der jährlichen Winterschule bis hin zu einem Trip nach Istanbul, der Gruppe teilzunehmen.

Bei allen Mitgliedern von T37 bedanke ich mich ganz besonders für das tolle Arbeitskli-ma in dieser Gruppe. Die vorliegende Arbeit betreffend leistete Julius Schulz großartige Arbeit zu den vorgestellten Monte-Carlo Simulationen, sowie zu den lokalen Poisson-Boltzmann Theorien. Bei meiner Bürokollegin Nadine Schwierz, die immer dazu bereit war meine Manuskripte auf Fehler zu untersuchen, bedanke ich mich für ein sehr ange-nehmes Büroklima und zahlreiche fach- und nichtfachliche Diskussionen. Ein herzliches Danke auch an Dominik Horinek der, neben seiner umfassenden wissenschaftlichen Tä-tigkeit, den Rechnercluster administrierte und mir damit ermöglichte zahlreiche für diese Arbeit essenzielle (und wahrscheinlich noch mehr sich als sinnfrei herausstellende) Re-chenjobs zu submittieren.
Für engagiertes Mitwirken bei "extracurricular" Aktivitäten, sogar auch in Garching, be-danke ich mich vor allem bei meinen Freunden Aykut Erbaş, Douwe Bonthuis, Richard Hawranek, Ioannis Daoutidis, Javier Madroñero, und Thomas Einert.

Ich bedanke mich bei meiner Familie, ganz besonders bei Christian, Karl, und Klaudia, die mir schon immer selbstlos zur Seite stehen, und mir dadurch unter anderem mein Studium ermöglichten.